



THE HONG KONG  
POLYTECHNIC UNIVERSITY

香港理工大學

Pao Yue-kong Library  
包玉剛圖書館

---

## Copyright Undertaking

This thesis is protected by copyright, with all rights reserved.

**By reading and using the thesis, the reader understands and agrees to the following terms:**

1. The reader will abide by the rules and legal ordinances governing copyright regarding the use of the thesis.
2. The reader will use the thesis for the purpose of research or private study only and not for distribution or further reproduction or any other purpose.
3. The reader agrees to indemnify and hold the University harmless from and against any loss, damage, cost, liability or expenses arising from copyright infringement or unauthorized usage.

If you have reasons to believe that any materials in this thesis are deemed not suitable to be distributed in this form, or a copyright owner having difficulty with the material being included in our database, please contact [lbsys@polyu.edu.hk](mailto:lbsys@polyu.edu.hk) providing details. The Library will look into your claim and consider taking remedial action upon receipt of the written requests.

The Hong Kong Polytechnic University

Department of Applied Physics

**Simulation of electromechanical properties  
in ferroelectric thin films**

Chung Wing Yee Winnie

A thesis submitted in partial fulfillment of  
the requirements for the Degree of  
Master of Philosophy

August, 2006

## CERTIFICATE OF ORIGINALITY

I hereby declare that this thesis is my own work and that, to the best of my knowledge and belief, it reproduces no material previously published or written nor material which has been accepted for the award of any other degree or diploma, except where due acknowledgement has been made in the text.

\_\_\_\_\_ (Signed)

CHUNG WING YEE WINNIE (Name of student)



## ABSTRACT

Electromechanical properties of ferroelectric thin films have drawn a lot of attention because of their applications in sensors, actuators and microelectromechanical devices. Their electrical properties not only depend on the electrical loading but also on the mechanical one. Similarly, the mechanical properties are influenced by both electrical and mechanical loadings. The coupling between the electrical and mechanical effects is obviously important for these phenomena. Thus, it is worthwhile to investigate these properties in order to understand the switching mechanisms behind the various phenomena and to optimize the device performance.

In this project, these properties were investigated theoretically using a modified two-dimensional four-state Potts model. It has been established that  $90^\circ$  domain-wall switching is responsible for electromechanical properties. Consequently, any theory that intends to explain or simulate electromechanical properties in microscopic scale should have the description and formulation to tackle this  $90^\circ$  domain-wall switching. Four-state Potts model provides a simple picture to meet this requirement. In my present work, the ferroelectric thin film is modelled by a two-dimensional array of dipoles and each of which is represented by a pseudo-spin. There are four possible states for the pseudo-spin which are mutually perpendicular to each other. The dipole orientation is associated with the deformation of a perovskite cell, through the ferroelastic effect. Consequently, there are also two strain states, correlated with the pseudo-spin states

---



according to the dipole orientation. In addition to the coupling of neighbouring dipoles and that between the dipoles and the electric field as in the Hamiltonian of a conventional Potts model or Ising model, the mechanical energy density and the coupling between neighbouring strain states are also incorporated in the Hamiltonian of our model. Moreover, the effect of anisotropic switching is also taken into account. The evolution of the ensemble of pseudo-spins and strain states can then be determined using the conventional metropolis algorithm. The macroscopic properties, such as polarization and strain, are then evaluated from the ensemble of pseudo-spins and strain states.

Stress always exists in ferroelectric films. The presence of stress alters the ferroelectric properties of thin films, such as phase transition temperature, polarization and strain. Experimental accounts on the effects of stress are numerous [Garino and Harrington, 1992; Kushida and Takeuchi, 1990; Kushida and Takeuchi, 1991; Rossetti et al., 1991; Shepard et al., 1996; Taylor et al., 2002; Yuzyuk et al., 2002]. For instance, the paraelectric–ferroelectric phase transition temperature can be determined from either the polarization versus temperature or susceptibility versus temperature relations. Only the electric field perpendicular to the film surface was applied to the system throughout our work. The shift in phase transition temperature in the presence of stress was obtained and compared with experimental results qualitatively [Abe and Komatsu, 1995; Taylor et al., 2002; Yuzyuk et al., 2002]. Moreover, we have also simulated the polarization–electric field and electric displacement–electric field hysteresis loops as well as the strain–electric field butterfly loops under different loading conditions: (i) static stress with alternating electric field and (ii) alternating stress and electric field. For the former

---



one, as observed from experiments, the presence of either in-plane tensile stress or longitudinal compressive stress reduces both the remnant and saturated polarizations. On the other hand, either in-plane compressive stress or longitudinal tensile stress leads to opposite effect. The corresponding strain responses of the thin films were also obtained. In particular, the dynamic change in strain over a cycle was enhanced under the following conditions: (i) in-plane tensile stress, (ii) uni-axial compressive stress, and (iii) small anisotropic switching factor  $\phi_c$ .

The experimental result on the dielectric and strain responses under combined electrical and mechanical loadings investigated by Zhou and Kamlah [Zhou and Kamlah, 2004] was also numerically simulated. It was found that when the alternating electric field and the uni-axial compressive stress are in phase, the dynamic changes for both electric displacement and strain are reduced. On a contrary, they are enhanced when both loadings are out-of-phase. Explanation to this novel behavior is presented in this thesis.



## PUBLICATIONS

1. Wing Yee Winnie Chung and Veng Cheong Lo, 'Phase Transition Temperature of Ferroelectric Thin Film Evaluated by Four-state Potts Model', *Material Research Society Symposia Proceedings*, **902E**, 0902-T10-51.1 (2006)
2. Hai-Xia Cao, Veng Cheong Lo and Winnie W. Y. Chung, 'Investigation of electromechanical properties in ferroelectric thin films', *Journal of Applied Physics*, **99**, 024103 (2006)
3. Wing Yee Winnie Chung and Veng Cheong Lo, 'Effect of Stress on the Phase Transition of Ferroelectric Films', to be published in *Japanese Journal of Applied Physics*, Vol **45**, No 10A, (2006).



## ACKNOWLEDGMENTS

I would like to gratefully acknowledge and express my sincere gratitude to my chief supervisor, Dr. V.C. Lo, for his invaluable direction, patient supervision and support throughout the period of my research work and thank for his suggestions regarding organization of the content and proofreading of this thesis. I would like to thank my co-supervisor, Dr. K.W. Kwok, and Prof. F.G. Shin for their fruitful discussion and helpful comments.

It is my pleasure to thank Mr. M.T. Lung for his help with my computer simulation at the beginning of my study. I would also like to express my gratitude to Ms. H.X. Cao for her comments and help.

Last but not least, I would like to thank my family and all my friends for their understanding, support and encourage. A special word of thanks goes to Mr. K.S. Wong for his patient, care, understanding and support.

Finally, I am grateful to The Hong Kong Polytechnic University in facilitating me the opportunity of pursuing the master degree at the Department of Applied Physics. This project is supported by a Hong Kong Polytechnic University research grant.



## TABLES OF CONTENTS

	PAGE
ABSTRACT .....	i
PUBLICATIONS .....	iv
ACKNOWLEDGEMENTS .....	v
TABLES OF CONTENTS .....	vi
LIST OF FIGURES .....	x
LIST OF TABLES .....	xvii
LIST OF SYMBOLS .....	xviii

## CHAPTERS

<b>Chapter 1 Introduction .....</b>	<b>1</b>
<i>1.1 Ferroelectric, ferroelastic and related electromechanical behaviors in materials science and technology.....</i>	<i>2</i>
<i>1.2 Ferroelectric thin films</i>	
1.2.1 The importance of thin films.....	9
1.2.2 The novel behaviors observed in ferroelectric thin films.....	10
<i>1.3 Objective of this work .....</i>	<i>12</i>



## Chapter 2 Literature Review

<b>2.1</b>	<b><i>Observed electromechanical phenomena reported in literature.....</i></b>	<b>14</b>
2.1.1	Effect of static stress on various ferroelectric properties.....	15
2.1.2	Effect of alternating stress.....	20
<b>2.2</b>	<b><i>Theoretical works on ferroelectricity.....</i></b>	<b>24</b>
2.2.1	Landau theory.....	24
2.2.2	First principles calculation .....	28
2.2.3	Ising and Potts models.....	31

## Chapter 3 Theory and numerical simulation

<b>3.1</b>	<b><i>Formulation of our Models.....</i></b>	<b>34</b>
3.1.1	Two-dimensional four-state Potts model.....	35
3.1.2	Initialization of domains.....	38
3.1.3	System Hamiltonian.....	45
<b>3.2</b>	<b><i>Boundary conditions.....</i></b>	<b>53</b>
<b>3.3</b>	<b><i>c-domain volume fraction and anisotropic switching.....</i></b>	<b>54</b>



<b>3.4</b>	<b><i>Switching mechanism and algorithm</i></b> .....	<b>58</b>
<b>3.5</b>	<b><i>Calculation of observable properties</i></b> .....	<b>60</b>
<b>3.6</b>	<b><i>Normalization of variables</i></b> .....	<b>62</b>

## **Chapter 4 Simulation results**

### **4.1 *Effect of static stress on phase transition temperature***

4.1.1	Experimental observations.....	66
4.1.2	Determination of phase transition temperature .....	67
4.1.3	Results and discussion.....	70

### **4.2 *Effect of static stress on other ferroelectric properties***

4.2.1	Experimental observations.....	80
4.2.2	Simulation.....	81
4.2.3	Results and discussion .....	83
4.2.4	Effects of anisotropic switching.....	104



**4.3 *Effect of combined alternating electrical and mechanical loadings***

4.3.1 Experimental observations.....**111**

4.3.2 Simulation.....**115**

4.3.3 Results and discussion.....**117**

**Chapter 5 Conclusion and Future work.....133**

**References.....136**



## LIST OF FIGURES

		<b>PAGE</b>
Figure 1.1	Typical $D$ - $E$ hysteresis loop in ferroelectrics [Cross and Newnham, 1987].....	5
Figure 1.2	Typical $\varepsilon$ - $E$ butterfly loop in ferroelectrics [Ball et al., 2005].....	5
Figure 1.3	Typical $P$ - $\sigma$ hysteresis loop in ferroelectrics [Ball et al., 2005].....	8
Figure 1.4	Typical $\varepsilon$ - $\sigma$ hysteresis loop in ferroelectrics [Ball et al., 2005].....	8
Figure 2.1	Different modes of dipolar switching: (a) $90^\circ$ switching and (b) $180^\circ$ switching induced by an applied field; (c) $90^\circ$ switching induced by an applied mechanical stress.....	21
Figure 2.2	The configuration of spins in a 2D array.....	31
Figure 3.1	The ferroelectric film is represented by the two-dimensional array of cells (rectangles).....	37
Figure 3.2	(a) A state is assigned to a randomly-selected site according to $\phi_c$ and the random numbers $r_1$ and $r_2$ . (b) A prescribed number of seed dipoles $N_D$ are randomly assigned in the film.....	39
Figure 3.3	The algorithm to determine the state of the seed dipole.....	40



Figure 3.4	(a) Another cell has to be selected again when there is no even one assigned neighboring cell. (b) In the presence of only one assigned neighboring cell, the unassigned cell will be assigned to the same state as this neighboring cell. (c) In the presence of two assigned neighboring cells with different states, the unassigned cell will be assigned to either one of these states with equal probabilities. Similar procedure is taken for assigning the unassigned selected cell if there are three or four assigned neighboring cells, as in (d) and (e).....	41-43
Figure 3.5	The steps for constructing domain configuration: (a) allocating the seed dipoles, (b) assigning the state of the unassigned neighboring cells, (c) repeating (b) until all cells are assigned.....	44
Figure 3.6	Nonlinear relation between stress and strain.....	49
Figure 3.7	Change in energy for (a) dipole transiting from in-plane ( <i>a</i> -domain) orientation to out-of-plane ( <i>c</i> -domain) orientation, and (b) dipole transiting from out-of-plane orientation to in-plane orientation. Case (a) is more energetically favorable in a <i>c</i> -domain-dominated sample.....	56
Figure 4.1	Polarization vs MCS per pseudo-spin at $e_3 = 0.02$ and $\bar{T} = 0.9$ .....	69
Figure 4.2	Polarization vs temperature for different transverse stress values ( $\zeta_1 = 0.0, -0.02$ and $+0.02$ ).....	70
Figure 4.3	Susceptibility vs temperature for different transverse stress values ( $\zeta_1 = 0.0, -0.02$ and $+0.02$ ).....	71
Figure 4.4	Polarization vs temperature for different longitudinal stress values ( $\zeta_3 = 0.0, -0.02$ and $+0.02$ ).....	72
Figure 4.5	Susceptibility vs temperature for different longitudinal stress values ( $\zeta_3 = 0.0, -0.02$ and $+0.02$ ).....	73



Figure 4.6	Susceptibility vs temperature for different strain-strain coupling coefficients ( $\alpha' = 0.0, 0.1$ and $0.3$ ).....	79
Figure 4.7	Polarization versus electric field under different static transverse stresses ( $\zeta_1 = 0.0, 0.5, -0.5$ ).....	84
Figure 4.8	Electric displacement versus electric field under static transverse stresses ( $\zeta_1 = 0.0, 0.5, -0.5$ ).....	85
Figure 4.9	(a) Longitudinal strain and (b) transverse strain versus electric field under static transverse stresses ( $\zeta_1 = 0.0, 0.5, -0.5$ ).....	86
Figure 4.10	Volume fractions of (a) State <i>A</i> and (b) State <i>C</i> versus electric field under different static transverse stresses ( $\zeta_1 = 0.0, 0.5, -0.5$ ).....	87
Figure 4.11	Volume fractions of (a) State <i>B</i> and (b) State <i>D</i> versus electric field under different static transverse stresses ( $\zeta_1 = 0.0, 0.5, -0.5$ ).....	88
Figure 4.12	Polarization versus electric field under different static longitudinal stresses ( $\zeta_3 = 0.0, 0.2, -0.2$ ).....	89
Figure 4.13	Electric displacement versus electric field under static longitudinal stresses ( $\zeta_3 = 0.0, 0.2, -0.2$ ).....	90
Figure 4.14	(a) Longitudinal strain and (b) transverse strain versus electric field under static longitudinal stresses ( $\zeta_3 = 0.0, 0.2, -0.2$ ).....	91
Figure 4.15	Volume fractions of (a) State <i>A</i> and (b) State <i>C</i> versus electric field under static longitudinal stresses ( $\zeta_3 = 0.0, 0.2, -0.2$ ).....	92
Figure 4.16	Volume fractions of (a) State <i>B</i> and (b) State <i>D</i> versus electric field under static longitudinal stresses ( $\zeta_3 = 0.0, 0.2, -0.2$ ).....	93



Figure 4.17	(a) Longitudinal strain and (b) transverse strain versus electric field under different magnitudes of longitudinal compressive stresses ( $\zeta_3 = 0.0, -0.2, -0.5, -1.0, -1.5$ )...	98
Figure 4.18	Volume fractions of (a) State A and (b) State C versus electric field under different magnitudes of longitudinal compressive stresses ( $\zeta_3 = 0.0, -0.2, -0.5, -1.0, -1.5$ )...	99
Figure 4.19	Volume fractions of (a) State B and (b) State D versus electric field under different magnitudes of longitudinal compressive stresses ( $\zeta_3 = 0.0, -0.2, -0.5, -1.0, -1.5$ )...	100
Figure 4.20	(a) Longitudinal strain and (b) transverse strain versus electric field under different transverse static stresses ( $\zeta_1 = 0.0, 0.5, 0.8, -0.5, -0.8$ ).....	102
Figure 4.21	(a) Longitudinal strain and (b) transverse strain versus electric field under different longitudinal static stresses ( $\zeta_3 = 0.0, 0.2, 0.5, -0.2, -0.5$ ).....	103
Figure 4.22	Polarization versus electric field under stress-free condition with different volume fraction of <i>c</i> -domains ( $\phi_c = 0.4, 0.5, 0.6$ ) .....	104
Figure 4.23	Electric displacement versus electric field under stress-free condition with different volume fraction of <i>c</i> -domains ( $\phi_c = 0.4, 0.5, 0.6$ ) .....	105
Figure 4.24	(a) Longitudinal strain and (b) transverse strain versus electric field under stress-free condition ( $\zeta_3 = \zeta_1 = 0.0$ ) with different volume fraction of <i>c</i> -domains ( $\phi_c = 0.4, 0.5, 0.6$ ).....	106



Figure 4.25	Volume fractions of (a) State <i>A</i> and (b) State <i>C</i> versus electric field under different stress-free condition ( $\zeta_3 = \zeta_1 = 0.0$ ) with different volume fraction of <i>c</i> -domains ( $\phi_c = 0.4, 0.5, 0.6$ ) .....	107
Figure 4.26	Volume fractions of (a) State <i>B</i> and (b) State <i>D</i> versus electric field under different stress-free condition ( $\zeta_3 = \zeta_1 = 0.0$ ) with different volume fraction of <i>c</i> -domains ( $\phi_c = 0.4, 0.5, 0.6$ ) .....	108
Figure 4.27	Electric-field-time and stress-time patterns in which the maximum stress is zero (released compression). (a) In-phase loading. (b) Out-of-phase loading. [Zhou, D. Y. and Kamlah, 2004].....	112
Figure 4.28	Comparison of the (a) electric displacement and (b) strain behavior in the stress-free state, under in-phase and out-of-phase electromechanical loading with zero-maximum stress. [Zhou, D. Y. and Kamlah, 2004].....	114
Figure 4.29	The normalized electric displacement of a film under stress-free state, in-phase and out-of-phase conditions .....	118
Figure 4.30	The normalized longitudinal strain behavior of a film under stress-free state, in-phase and out-of-phase conditions.....	119
Figure 4.31	Electric displacement versus electric field under stress-free, in-phase and out-of-phase conditions. Symbols are experimental results from Zhou and Kamlah, and lines are simulated results.....	121
Figure 4.32	Longitudinal strain versus electric field under stress-free, in-phase and out-of-phase conditions. Symbols are experimental results from Zhou and Kamlah, and lines are simulated results.....	122



Figure 4.33	Electric-field-time and stress-time patterns of the in-phase loading condition in which the maximum stress is zero (released compression).....	124
Figure 4.34	Effects of both influences cancel each other when both $E_3$ and $\sigma_3$ are the maximum (At point A in Figure 4.33).....	124
Figure 4.35	Electric-field-time and stress-time patterns of the in-phase loading condition in which the maximum stress is zero (released compression).....	125
Figure 4.36	Effects of both influences cancel each other when both $E_3$ and $\sigma_3$ are exactly at one-half of their maximum value (At point B in Figure 4.35).....	125
Figure 4.37	Electric-field-time and stress-time patterns of the in-phase loading condition in which the maximum stress is zero (released compression).....	126
Figure 4.38	Dipoles remain in its original status when both $E_3$ and $\sigma_3$ are nearly zero (At point C in Figure 4.37).....	126
Figure 4.39	Electric-field-time and stress-time patterns of the out-of-phase loading condition in which the maximum stress is zero (released compression).....	128
Figure 4.40	Dipoles are aligned along the electric field direction when $E_3$ is the maximum and $\sigma_3$ is zero (At point A in Figure 4.39).....	128
Figure 4.41	Electric-field-time and stress-time patterns of the out-of-phase loading condition in which the maximum stress is zero (released compression).....	129
Figure 4.42	Effects of both influences cancel each other at point B. The two possibilities of dipole orientation when both $E_3$ and $\sigma_3$ are exactly at one-half of their maximum value (At point B in Figure 4.41).....	129



Figure 4.43	Electric-field-time and stress-time patterns of the out-of-phase loading condition in which the maximum stress is zero (released compression).....	130
Figure 4.44	Dipoles are aligned perpendicular to the stress direction when $E_3$ is nearly equal to zero and $\sigma_3$ is the maximum (At point C in Figure 4.43).....	130
Figure 4.45	Volume fractions of (a) State A and (b) State C versus electric field under stress-free state, in-phase and out-of-phase conditions.....	131
Figure 4.46	Volume fractions of (a) State B and (b) State D versus electric field under stress-free state, in-phase and out-of-phase conditions.....	132

**LIST OF TABLES**

	<b>PAGE</b>
Table 2.1 The polarization components of the theoretically predicted phases in epitaxial ferroelectric thin films [Pertsev et al., 1998] .....	16
Table 3.1 Association between dipole states and ferroelastic strain states of perovskite cell.....	48
Table 3.2 The change in Hamiltonian $\Delta H'$ for the case (a) <i>c</i> -domains are dominant and (b) <i>a</i> -domains are dominant after switching between <i>a</i> -domain and <i>c</i> -domain.....	57
Table 4.1 The set of real parameters used for the simulation.....	120

**LIST OF SYMBOLS**

$a_0$	Length of the longitudinal edge of a tetragonal cell
$c_0$	Length of the transverse edge of a tetragonal cell
$D$	Electric displacement
$D_3$	Electric displacement along the electric field direction
$d_3$	Normalized electric displacement along the electric field direction
$d_{ij}$	piezoelectric tensors
$d_{33}$	Longitudinal piezoelectric coefficient
$d_{13}$	Transverse piezoelectric coefficient
$d'_{33}$	Normalized longitudinal piezoelectric coefficient
$d'_{13}$	Normalized transverse piezoelectric coefficient
$\hat{E}$	Electric field in matrix form
$\hat{E}^T$	Transpose of matrix $\hat{E}$
$E$	Electric field
$E_c$	Coercive field strength
$E_{dc}$	Amplitude of the static electric field
$E_0$	Amplitude of the alternating electric field
$E_3$	Component of electric field along the $z$ - (longitudinal) direction

---



$E_1$	Component of electric field along the $x$ - (transverse) direction
$\hat{e}$	Normalized electric field in matrix form
$\hat{e}^T$	Transpose of matrix $\hat{e}$
$e_{dc}$	Normalized amplitude of the static electric field
$e_0$	Normalized amplitude of the alternating electric field
$e_3$	Component of the normalized electric field along the $z$ - (longitudinal) direction
$e_1$	Component of the normalized electric field along the $x$ - (transverse) direction
$H$	Total Hamiltonian energy
$H'$	Energy for the switching anisotropy
$H_3$	Energy barrier between $a$ - and $c$ - domains during switching
$h$	Normalized total Hamiltonian energy
$h'$	Normalized energy for the switching anisotropy
$h_3$	Normalized energy barrier between $a$ - and $c$ - domains during switching
$i$	Index describing the location of a cell in the film along the $x$ - (transverse) direction
$J$	Dipole-dipole coupling coefficient
$j$	Index describing the location of a cell in the film along the $z$ - (longitudinal) direction

---



	direction
$k_B$	Boltzmann's constant
$k$	Coefficient for the stress-strain shape function
$N_D$	Number of seed dipoles (OR number of domains)
$N_x$	Number of dipoles (cells) along the $x$ - (transverse) direction
$N_y$	Number of dipoles (cells) along the $y$ -direction
$N_z$	Number of dipoles (cells) along the $z$ - (longitudinal) direction
$\hat{n}$	Normal vector along the electric field direction
$\hat{n}^T$	Transpose of matrix $\hat{n}$
$n$	Index for the stress-strain shape function
$P$	Polarization
$P_r$	Remanent polarization
$P_3$	Polarization along the $z$ - (longitudinal) direction
$P_2$	Polarization along the $y$ -direction
$P_1$	Polarization along the $x$ - (transverse) direction
$P_{SAT}$	Magnitude of the saturated polarization
$p_r$	Normalized remanent polarization
$p_s$	Spontaneous polarization
$p_3$	Normalized polarization along the $z$ - (longitudinal) direction

---



$\hat{q}$	Normal vector along the $x$ - (transverse) direction
$\hat{q}^T$	Transpose of matrix $\hat{q}$
$q$	Number of states (dipole orientations) in Potts model
$q_{ijkl}$	Electrostriction tensors
$r$	Random number in the interval (0, 1)
$r_1$	Random number in the interval (0, 1)
$r_2$	Random number in the interval (0, 1)
$\hat{S}$	Pseudo-spin matrix representation of the dipole orientation of a cell
$\hat{S}'$	Pseudo-spin matrix representation of the dipole orientation of a cell after 90° rotation
$\hat{S}^T$	Transpose of matrix $\hat{S}$
$T$	Temperature
$T_0$	Curie-Weiss temperature
$T_c$	Curie temperature
$\bar{T}$	Normalized temperature
$\bar{T}_c$	Normalized Curie temperature
$t$	Physical time
$t_{MCS}$	Time in Monte Carlo Steps



$Y$	Young's Modulus
$Y'$	Normalized Young's Modulus
$x$ -	Transverse direction
$z$ -	Longitudinal direction
$\alpha$	Strain-strain coupling coefficient
$\alpha'$	Normalized strain-strain coupling coefficient
$\beta_1$	Constant in standard Potts model
$\beta_2$	Constant in planar Potts model
$\delta$	Domain size
$\phi$	Phase difference between the applied field and stress
$\phi_c$	Volume fraction of $c$ -domains
$\phi_a$	Volume fraction of $a$ -domains
$\phi_{S_A}$	Volume fraction of State $A$
$\phi_{S_B}$	Volume fraction of State $B$
$\phi_{S_C}$	Volume fraction of State $C$
$\phi_{S_D}$	Volume fraction of State $D$
$\theta_n$	Angle between two adjacent dipoles
$\kappa_0$	Permittivity of free space
$\kappa_r$	Relative permittivity of the material

---



$\kappa$	Permittivity of the material ( $\kappa = \kappa_0 \kappa_r$ )
$\kappa'$	Normalized dielectric permittivity of the material
$\hat{\sigma}$	Mechanical stress in matrix form
$\hat{\sigma}^T$	Transpose of matrix $\hat{\sigma}$
$\sigma$	Stress
$\sigma_{dc}$	Amplitude of the applied static stress
$\sigma_0$	Amplitude of the alternating stress
$\sigma_3$	Component of stress along the $z$ - (longitudinal) direction
$\sigma_1$	Component of stress along the $x$ - (transverse) direction
$\sigma_{crit}$	Critical stress for the linear relation between stress and strain
$\hat{\zeta}$	Normalized mechanical stress in matrix form
$\hat{\zeta}^T$	Transpose of matrix $\hat{\zeta}$
$\zeta_{dc}$	Normalized amplitude of the static stress
$\zeta_0$	Normalized amplitude of the alternating stress
$\zeta_3$	Component of the normalized stress along the $z$ - (longitudinal) direction
$\zeta_1$	Component of the normalized stress along the $x$ - (transverse) direction
$\zeta_{crit}$	Normalized critical stress for the linear relation between stress and strain
$\hat{\varepsilon}$	Total strain in matrix form
$\hat{\varepsilon}^0$	Initial strain in matrix form

---



$\hat{\varepsilon}^F$	Ferroelastic strain in matrix form
$\hat{\varepsilon}^{F^T}$	Transpose of matrix $\hat{\varepsilon}^F$
$\hat{\varepsilon}^E$	Field-induced strain in matrix form
$\hat{\varepsilon}^{el}$	Stress-induced elastic strain in matrix form
$\varepsilon$	Strain
$\varepsilon_3^E$	Component of the field-induced strain along the $z$ - (longitudinal) direction
$\varepsilon_1^E$	Component of the field-induced strain along the $x$ - (transverse) direction
$\varepsilon_3^{el}$	Component of the stress-induced elastic strain along the $z$ - (longitudinal) direction
$\varepsilon_1^{el}$	Component of the stress-induced elastic strain along the $x$ - (transverse) direction
$\varepsilon_0$	Reference strain due to ferroelastic switching
$\varepsilon_{sat}$	Total saturation strain of the material
$\varepsilon_3$	Component of strain along the $z$ - (longitudinal) direction
$\varepsilon_1$	Component of strain along the $x$ - (transverse) direction
$\hat{\xi}$	Normalized total strain in matrix form
$\hat{\xi}^0$	Normalized initial strain in matrix form
$\hat{\xi}^F$	Normalized ferroelastic strain in matrix form
$\hat{\xi}^{F^T}$	Transpose of matrix $\hat{\xi}^F$

---



$\hat{\xi}^E$	Normalized field-induced strain in matrix form
$\hat{\xi}^{el}$	Normalized stress-induced elastic strain in matrix form
$\xi_3^E$	Component of the normalized field-induced strain along the $z$ - (longitudinal) direction
$\xi_1^E$	Component of the normalized field-induced strain along the $x$ - (transverse) direction
$\xi_3^{el}$	Component of the normalized stress-induced elastic strain along the $z$ - (longitudinal) direction
$\xi_1^{el}$	Component of the normalized stress-induced elastic strain along the $x$ - (transverse) direction
$\xi_0$	Normalized reference strain due to ferroelastic switching
$\xi_3$	Component of normalized strain along the $z$ - (longitudinal) direction
$\xi_1$	Component of normalized strain along the $x$ - (transverse) direction
$\Gamma$	Period in real time
$\Gamma_{MCS}$	Period in Monte Carlo Steps
$\chi_{33}$	Dielectric susceptibility along the electric field direction
$\bar{\chi}_{33}$	Normalized dielectric susceptibility along the electric field direction
$\nu$	Poisson ratio
$\nu_c$	Volume of a single tetragonal cell

---



$\Delta H$  Change in Hamiltonian energy

$\Delta H'$  Change in energy due to anisotropy switching

$\Delta t$  infinitesimal time step



## Chapter 1 Introduction

Since the discovery of ferroelectricity in polycrystalline ceramics during the early to mid-1940s, they have been widely used as capacitors, transducers and sensors [Cross and Newnham, 1987]. Among different families of ferroelectrics, perovskite-type ferroelectrics, such as  $\text{Pb}(\text{Zr}_x\text{Ti}_{1-x})\text{O}_3$  (PZT) and  $\text{BaTiO}_3$ , are commonly used due to their superior ferroelectric, piezoelectric and pyroelectric properties. Owing to the maturity of thin film fabrication techniques, increasing attention has been drawn to the potential applications of ferroelectric thin films in nonvolatile memory, dynamic random access memory (DRAM), ultrasonic actuators and micro-electromechanical (MEMS) devices. However, both experimental and theoretical investigations have shown that the physical properties of ferroelectric thin films substantially differ from those of bulk ferroelectrics. To sustain the trend towards further miniaturization of microelectronic devices, a thorough understanding of the electromechanical properties of ferroelectric thin films is vitally important. Such investigation can also assist both structural and material designs of thin-film based electromechanical devices for optimal performance.



## ***1.1 Ferroelectric, ferroelastic and related electromechanical behaviors in materials science and technology***

Ferroelectricity was discovered in 1921 by Valasek. The term ‘ferroelectricity’ is used in analogy to ferromagnetism, in which a material exhibits a permanent magnetic moment. Valasek discovered that the polarization of sodium potassium tartrate tetrahydrate ( $\text{NaKC}_4\text{H}_4\text{O}_6 \cdot 4\text{H}_2\text{O}$ ), better known as Rochelle salt, could be reversed by the application of an external electric field [Lines and Glass, 1977]. Similar to the phenomena observed in ferromagnetism, the spontaneous polarization, which can be reversed with an applied electric field, exists in ferroelectric materials. The first demonstration of polarization reversal was by the observation of dielectric hysteresis (Valasek, 1920) through the Sawyer-Tower circuit, which is still frequently used for the characterization of ferroelectrics. Similar to ferromagnetism, a sharp peak also exists in the susceptibility versus temperature curve where the paraelectric–ferroelectric phase transition takes place. The temperature at this peak is called Curie temperature  $T_c$ .

Beginning with the pioneering work on Rochelle salt and potassium dihydrogen phosphate, the study of ferroelectrics has been rapidly accelerated during World War II (1940s) due to the discovery of perovskite barium titanate ( $\text{BaTiO}_3$ ) [Lines and Glass, 1977]. In the following decade, more than 100 new ferroelectrics had been identified. Lead zirconate titanate (PZT) has surpassed  $\text{BaTiO}_3$  (BT) due to its better performance for various applications. Because of the simplicity in crystal structure, chemical and mechanical stability and existence of ferroelectric state at



room temperature, perovskite-type ferroelectrics rapidly became a very important group of ferroelectrics and the most extensively investigated ferroelectric material.

Ferroelectric materials are manifested by the presence of domain structure and spontaneous polarization  $p_s$  at temperatures below  $T_c$  [Smith, 2005]. Spontaneous polarization, which only exists in ferroelectric phase, is defined as the dipole moment per unit volume, or by the charge per unit area  $A$  developed on the surface normal to the spontaneous polarization. As the temperature  $T$  increases, the spontaneous polarization  $p_s$  decreases and eventually disappears at a Curie temperature  $T_c$  [Lines and Glass, 1977]. (In 2<sup>nd</sup> order phase transition,  $p_s$  gradually diminishes to zero, but for 1<sup>st</sup> order phase transition, it undergoes a sudden jump to zero at  $T_c$ .) Moreover, the permittivity is divergent at  $T_c$ . Above  $T_c$ , the materials exhibit paraelectric behavior, i.e. the polarization disappears in the absence of external electric field. For perovskite-type ferroelectrics, the crystal structure of paraelectric phase is cubic and the spontaneous polarization is absent because of the symmetrical property. Ferroelasticity is manifested by the presence of spontaneous strain, in the absence of either electric field or stress. Ferroelastic behavior can also be observed for several ferroelectric materials, such as tetragonal zirconia, zirconates, titanates and vanadates. The crystal structure is distorted and reoriented when an external mechanical loading is applied. Instead of spontaneous magnetization or polarization, a spontaneous strain is developed below a paraelastic to ferroelastic phase transition.



In ferroelectric materials, both hysteresis and nonlinear constitutive relations exist. The polarization  $P$  and strain  $\varepsilon$  can be expressed as a function of  $E$  and  $\sigma$ , i.e.,  $P = f(E, \sigma)$  and  $\varepsilon = g(E, \sigma)$ , where  $P$ ,  $E$ ,  $\sigma$  and  $\varepsilon$  are polarization, electric field, stress and strain, respectively. These relations demonstrate that the electrical and mechanical responses, i.e.  $P$  and  $\varepsilon$  of ferroelectric materials can be induced by either electrical or mechanical loading, and they are strongly coupled with each other. The electrical properties of ferroelectric materials, such as dielectric properties and hysteresis in their  $P(E)$  relationship, depend not only on the electrical loading, but also on the mechanical one. The orientation of the dipoles would be influenced by the presence of stress, which may hinder or enhance the polarization switching in ferroelectric materials. Similarly, the mechanical properties, such as the strain-electric field butterfly loop ( $\varepsilon$ - $E$ ) and the piezoelectricity, are influenced by both electrical and mechanical loading. Thus, the coupling between the two responses, electrical and mechanical, is obviously important for these phenomena.

Practically, it is more convenient to investigate the electric displacement-electric field ( $D$ - $E$ ) loop. The electric displacement  $D$  is related by  $D = P + \kappa E$ , where  $\kappa = \kappa_o \kappa_r$ ,  $\kappa_o$  is the permittivity of free space and  $\kappa_r$  is the relative permittivity of the material. Typical displacement-electric field hysteresis loop ( $D$ - $E$  loop) and strain-electric field butterfly loop ( $\varepsilon$ - $E$  loop) are shown in Figure 1.1 and Figure 1.2, respectively.

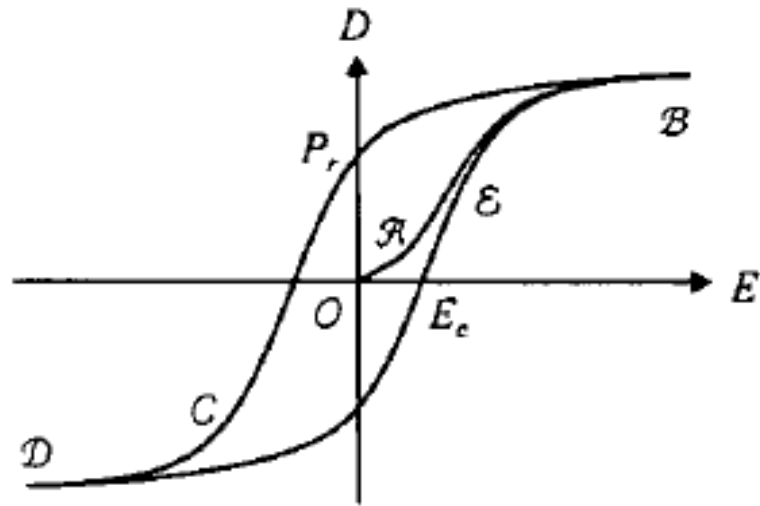


Figure 1.1 Typical  $D$ - $E$  hysteresis loop in ferroelectrics [Cross and Newnham, 1987]

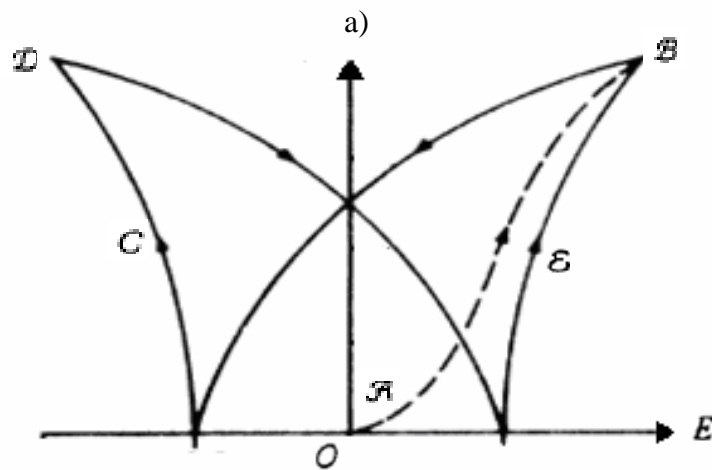


Figure 1.2 Typical  $\epsilon$ - $E$  butterfly loop in ferroelectrics [Ball et al., 2005]



As illustrated in Figure 1.1 and Figure 1.2, the initially unpoled ferroelectric material is represented by the point  $O$ . The orientation of the domains is randomly oriented resulting in zero electric displacement in this state. The electric displacement  $D$  increases along path  $\mathcal{A}$  when the electric field increases from zero. The domain structure is unchanged and the ions of the unit cells are shifted within the neighborhood of their equilibrium positions when the electric field is sufficiently small. The dielectric behavior, i.e. the plot of polarization vs. applied field, is reversible and approximately linear in this state. As the electric field reaches the coercive field strength  $E_c$ , irreversible switching processes of the domains are initiated. Dipoles are preferentially aligned along the direction of electric field through  $90^\circ$  or  $180^\circ$  rotations. Majority of the domains are aligned along the electric field direction when the sample reaches point  $\mathcal{B}$ . The polarization becomes positively saturated. As the field  $E$  is gradually reduced from the point  $\mathcal{B}$ , the displacement  $D$  is reduced simultaneously along the segment  $\mathcal{BCD}$ . At zero field, the displacement  $D$  has a non-zero value  $P_r$ , called the remanent polarization. The remanent polarization is positive as a greater portion of domains is still aligned in the positive direction. The displacement  $D$  is reduced to zero when the field equals to  $-E_c$ . Below this point,  $D$  changes sign (from positive to negative) by rotation of dipoles to the opposite direction. At point  $\mathcal{D}$ , the material is polarized to negative saturation. If the field  $E$  increases again, the profile of  $D$  is along the segment  $\mathcal{DEB}$ . The closed segment  $\mathcal{BCDEB}$  forms a saturated  $D$ - $E$  hysteresis loop of the material.



The butterfly loops, formed by the strain vs. applied electric field  $E$ , is shown in Figure 1.2. Since the onset of ferroelectric/ferroelastic switching processes is triggered if the applied field exceeds the coercive field, energetically favorable domains grow. In these domains, dipoles are aligned along the field direction. A significant elongation of the specimen is observed (along path  $\mathcal{A}$ ). The elongation is mainly due to two contributions. The first one is by the growth in volume fraction of the energetically favorable domains through dipole rotations and the second one is the piezoelectric effect in which the charge separation inside a cell leads to an additional deformation. The strain of the material reaches the maximum at point  $\mathcal{B}$  as the field is the maximum. The strain is then reduced as the electric field decreases. When the electric field equals to zero, only the ferroelastic component remains. Upon reversing the electric field beyond the coercive field strength, backswitching process takes place. The strain attains a sharp minimum. Below this point, the corresponding  $D$  of the material changes sign (from positive to negative). However, domains aligned along the  $c$ -axes dominate. Thus, the switching strain as well as the piezoelectric strain starts to increase again. The strain attains another maximum at point  $\mathcal{D}$  when the electric field is maximal at the negative direction.

The presence of stress produces very similar effects on the polarization and strain. In Figure 1.3, the spontaneous polarization is reduced by the application of compressive stress along the polarization direction. Likewise, the longitudinal strain is also reduced, as shown in Figure 1.4. Upon the removal of stress, both the polarization and strain slightly increase, but cannot restore to their initial values. This is due to the irreversible nature of ferroelastic switching. We will elaborate in details in Chapter 3.

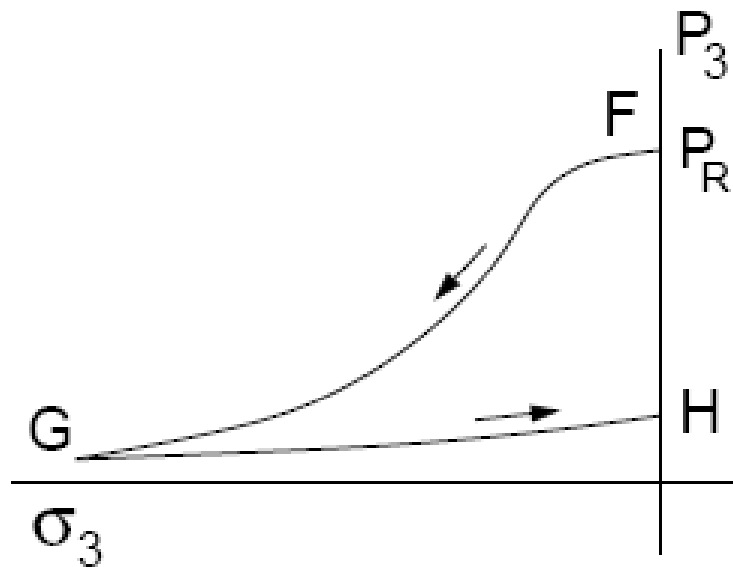


Figure 1.3 Typical  $P$ - $\sigma$  hysteresis loop in ferroelectrics [Ball et al., 2005]

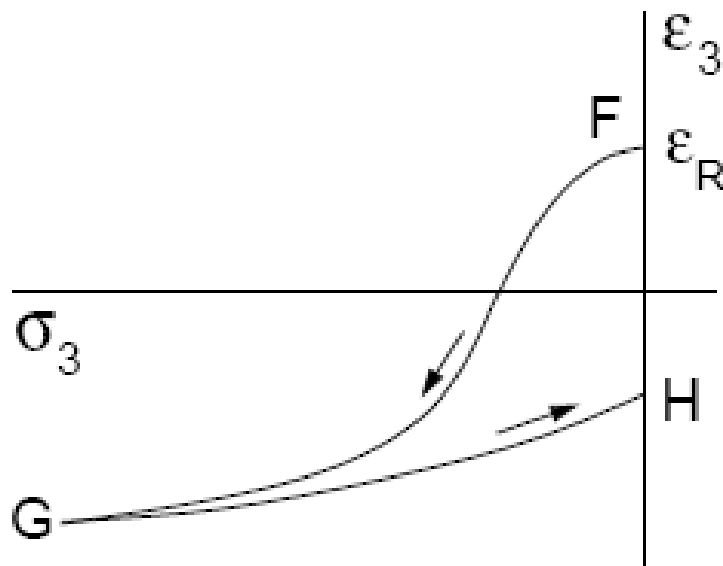


Figure 1.4 Typical  $\epsilon$ - $\sigma$  hysteresis loop in ferroelectrics [Ball et al., 2005]



## **1.2 *Ferroelectric thin films***

### **1.2.1 The importance of thin films**

Piezoelectric materials have been widely used for sensors and actuators including strain gauges, pressure transducers and accelerometers. However, bulk-type sensors suffer from several shortcomings such as low fracture toughness, high inertia and relatively large size. Recently, due to the remarkable progress in epitaxial growth of perovskite-type thin films using different methods, ferroelectric devices and components in thin film form become possible. Moreover, both experimental and theoretical investigations have shown that the physical properties of ferroelectric thin films substantially differ from those of bulk ferroelectrics [Taylor et al., 2002; Yuzyuk et al., 2002; Maiwa and Ichinose, 2003; Berfield et al., 2004]. Ferroelectric thin films, with much superior performance, attract a lot of attention for both academic interests and applications. We will elaborate these novel behaviors in the next section.

Thin film ferroelectrics have been used for micro-electromechanical systems (MEMS), such as micro-scanning mirrors, atomic force microscope cantilevers and membrane-type micropumps. The major advantages of using thin film include: high speed, small profile, low power consumption and capable to be integrated with silicon ICs. On the other hand, the presence of residual stresses is an inevitable problem in thin films where it can be easily accommodated in a bulk material. For instance, films grown on different substrates or by different deposition methods would have different initial residual stress states [Zhou, Y.C. et al., 2003; Lian and Sottos, 2004; Ohno et al.,



2004]. The presence of this residual stress might sometimes be an advantage to yield a better performance, such as a higher dielectric constant. However, it might also impose adverse effects, such as shrinkage of the film's service life, delamination of the film from the substrate or cracking. Thus, the study of the residual stress is important. A thorough understanding of the physical mechanism behind the observable phenomena about the electromechanical properties of such films can assist both structural and material designs for optimal performance.

### **1.2.2 The novel behaviors observed in ferroelectric thin films**

Experimental investigations on the electromechanical properties of ferroelectric thin films are quite exhaustive. Stress is an important factor and always exists in ferroelectric films. The existence of stress is mainly caused by thermal mismatch or lattice mismatch between substrate and film. For instance, compressive or tensile residual stresses of the order of several hundred MPa have been reported [Tuttle et al., 1992; Zhang, L. L. et al., 2003; Ohno et al., 2004]. It may also be created by the geometrical change upon the phase transition. Alternatively, stress can be imposed externally. In the followings, we will discuss the stress effects on ferroelectric properties, such as phase transition temperature, remanent polarization and coercive field, and the possible causes for these properties.



In brief, the phase transition temperature in the ferroelectric thin films can be changed by the application of stress. According to the experimental works of Rossetti et al. [Rossetti et al., 1991] and Yuzyuk et al. [Yuzyuk et al., 2002], the in-plane compressive stress resulted in increasing the Curie temperature, while the tensile stress induced the decrease in the Curie temperature. Moreover, some of them suggested that the existence of in-plane compressive stress favors the alignment of dipoles along the longitudinal direction whereas in-plane tensile stress encourages in-plane dipole alignment. The existence of stress also influences the dielectric and mechanical properties of ferroelectric films. Many experiments demonstrated that both remanent polarization in  $P$ - $E$  loop and field-induced strain in  $\varepsilon$  -  $E$  loop increase under in-plane compressive stress and decrease under a tensile stress.



### **1.3 Objective of this work**

The aim of this project is to establish a theoretical framework for the simulation of electromechanical properties in the nanometer scale. Most of the past theoretical works are based on Landau thermodynamic theory. Even though it has been widely used for theoretical analysis with great success, it is a macroscopic approach only relating macroscopic quantities in the free energy expression while those mechanisms in atomic or cell levels have been overlooked. Moreover, it does not provide a picture on how a dipole is rotated during the polarization switching. Thus, it might not be applicable to systems in nanometer scale. We will make a detailed review on the Landau theory in Chapter 2. Moreover, the microscopic pictures, such as the switching mechanism of individual dipoles and the domain configuration, may facilitate us to understand the origin of various phenomena in ferroelectric thin films. In this study, a modified two-dimensional four-state Potts model, which considers the interactions between dipoles and between dipoles and external electrical or mechanical loading, has been adopted. The changes in electromechanical properties of ferroelectric films under stress observed in experiments are reproduced by using our model.

The thesis was divided into five chapters. The motivation of this research is presented in Chapter 1. A brief review on the background of both theoretical and experimental works achieved in the literature will be presented in Chapter 2. In Chapter 3, we will present our model and the theoretical framework with the associated mathematical formulation. Based on this model, the simulation results,



such as polarization-temperature curves, susceptibility-temperature curves, polarization-electric field hysteresis loops and strain-electric field butterfly loops, will be presented in Chapter 4. The stress effect on phase transition temperature is then demonstrated and compared with experimental results. The effect of static stress on the polarization-electric field hysteresis loop and strain-electric field butterfly loop will also be discussed. Furthermore, the simulation results of both the polarization and strain responses under combined alternating electromechanical loading are presented and compared with experimental data.



## Chapter 2 Literature Review

### ***2.1 Observed electromechanical phenomena reported in literature***

Most studies on the application of ferroelectric materials aim at fabricating thin films with large switchable polarizations and high dielectric responses. On decreasing the thickness of a ferroelectric film down to nanometer scale, distinct properties occur, such as enhanced dielectric permittivity, enhanced piezoelectric coefficients, and the shift in phase transition temperature. [Takayama and Tomita, 1989; Scott, 1996]. There are two major causes for the distinct ferroelectric properties in thin film: the dominance of interfacial effect and the diminishing of collective dipole-dipole interactions because of the smaller system size. One of the roles of the interface on the ferroelectric thin film is to impose interfacial stress, which might be negligible in a bulk system. There are many origins for the presence of interfacial stress: thermal or lattice mismatch between the film and the underlying substrate or film, structural and dimensional change upon phase transition and the application of a bending moment. The direction of the stress induced by these causes is basically transverse (or parallel to the film). On the other hand, longitudinal stress (normal to film) can also exist when two or more films are stacked together, or it is under a uniaxial mechanical loading. The following section summarizes the effect of stress on various ferroelectric properties.



### 2.1.1 Effect of static stress on various ferroelectric properties

#### (a) Effect of stress on the ferroelectric-paraelectric phase transition

Both the paraelectric to ferroelectric transition temperature and the stability of ferroelectricity are strongly influenced by the presence of interfacial stress [P.W. Forsbergh, 1954; Rossetti et al., 1991; Pertsev et al., 1998; Pertsev et al., 1999; Taylor et al., 2002; Yuzyuk et al., 2002]. Due to the distortion of the crystal structure under different stress states (compressive or tensile), the ferroelectricity can be suppressed or enhanced in epitaxially-grown ferroelectric films [Frey and Payne, 1993; Waser, 1997; Yuzyuk et al., 2002]. Thus, the stress effect on the crystal structure, which is related to the ferroelectric phase, and the ferroelectric-paraelectric phase transition in ferroelectric films are strongly correlated.

Numerous experiments demonstrated the effects of interfacial stress on structural characteristics of ferroelectric phase in thin films [Rossetti et al., 1991; Berfield et al., 2004; Lian and Sottos, 2004]. Most of them have reported that BaTiO<sub>3</sub>-based epitaxial films on cubic substrates, such as silicon substrates, failed to display pronounced hysteresis loops comparable to the corresponding bulk materials [Frey and Payne, 1993; Waser, 1997]. Thus, Pertsev et al. [Pertsev et al., 1998; Pertsev et al., 1999] have suggested that the presence of transverse tensile stress in BaTiO<sub>3</sub> (BT) film on a silicon substrate can alter the types of stable ferroelectric phases, such as the *a* phase (tetragonal phase along transverse direction where  $P_1 \neq 0$  and  $P_2 = P_3 = 0$ ) and the *ac* phase (where  $P_1 \neq 0$ ,  $P_3 \neq 0$  and  $P_2 = 0$ ), with respect to that in a bulk material. The definition of



the ferroelectric phases and their polarization components in ferroelectric films [Pertsev et al., 1998] are shown in Table 2.1.

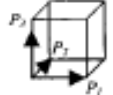
Phase	Polarization components	
<i>Paraelectric</i>	$P_1 = P_2 = P_3 = 0$	
<i>c</i> phase	$P_1 = P_2 = 0, P_3 \neq 0$	
<i>a</i> phase	$P_1 \neq 0, P_2 = P_3 = 0$	
<i>ac</i> phase	$P_1 \neq 0, P_2 = 0, P_3 \neq 0$	
<i>aa</i> phase	$P_1 = P_2 \neq 0, P_3 = 0$	
<i>r</i> phase	$P_1 = P_2 \neq 0, P_3 \neq 0$	

Table 2.1 The polarization components of the theoretically predicted phases in epitaxial ferroelectric thin films [Pertsev et al., 1998]

Due to the two-dimensional clamping effect by the tensile stress, the tetragonal phase along transverse direction (*a* phase) was no longer stable in the BT films. Conversely, ferroelectric phases, such as orthorhombic *aa* phase (where  $P_1 = P_2 \neq 0$  and  $P_3 = 0$ ) and monoclinic *r* phase (where  $P_1 = P_2 \neq 0$  and  $P_3 \neq 0$ ) with two and three nonzero polarization components, were stabilized in the films which do not exist in bulk sample. They also suggested that the misfit tensile strain in BaTiO<sub>3</sub> films favored the existence of the orthorhombic *aa*



phase in which the polarization was parallel to the film. The volume fraction of longitudinal domains aligned was correspondingly reduced. Therefore, the overall longitudinal polarization was suppressed under the transverse tensile stress. On the other hand, from Yuzyuk's work, the epitaxially-grown (Ba,Sr)TiO<sub>3</sub> thin film on (001) MgO substrate was under in-plane compressive stress. The thermal misfit compressive strain favored the longitudinal domains resulting in enhanced ferroelectricity along the longitudinal direction.

Since the ferroelectric phase can be altered by the stress, the ferroelectric-paraelectric phase transition temperature in thin film can also be changed. Both Rossetti et al. [Rossetti et al., 1991] and Yuzyuk et al. [Yuzyuk et al., 2002] have demonstrated that the in-plane compressive stress increased the Curie temperature  $T_c$ . In particular, Rossetti et al. have shown an increase in  $T_c$  by nearly 50°C in the presence of  $3.5 \times 10^8 \text{ N/m}^2$  in-plane compressive stress in PbTiO<sub>3</sub> thin film. Yuzyuk et al., likewise, have shown that BST-0.3 thin film under in-plane compressive stress on a (001) MgO substrate exhibited a higher  $T_c$  (365K) than the value (300K) of its bulk counterpart. Similar results were obtained for epitaxial ferroelectric SrTiO<sub>3</sub> films on (001) LaAlO<sub>3</sub> substrates.

On the other hand, Taylor et al. [Taylor et al., 2002] have reported a decrease in  $T_c$  under a large tensile strain. This in-plane biaxial tension induced a contraction normal to the film on one hand and forced the alignment of dipoles along the film on the other. The correlation between the shifting direction of  $T_c$  and the sign (i.e. negative for compressive and positive for



tensile stress) of the in-plane stress has also been experimentally confirmed by Pertsev et al [Pertsev et al., 1999]. Furthermore, Lu et al. [Lu et al., 2000] have studied the critical behavior theoretically using Landau theory by incorporating an additional stress-gradient term in Landau free energy expression and have successfully derived the similar shifting trend of  $T_c$  under different in-plane stresses.

#### **(b) Other ferroelectric properties**

The electromechanical responses of thin films can also be greatly influenced by the applied static stress. Garino and Shepard [Garino and Harrington, 1992] and Shepard et al. [Shepard et al., 1996] have investigated the change in  $P$ - $E$  hysteresis loop caused by the mechanical stress in ferroelectric thin films. The PZT films used in their experiments were under a residual in-plane tensile stress. Both remnant and saturated polarizations decreased when the PZT film was subject to a transverse tensile stress perpendicular to the applied electric field direction whereas the remnant and saturated polarizations increased under a compressive stress. The area of the  $P$ - $E$  hysteresis loop was reduced under an in-plane tensile stress but enlarged under a compressive stress. Furthermore, both spontaneous polarization and the dielectric constant in the samples decreased with the transverse tensile stress and increased with the compressive stress.



Shaw et al. [Shaw et al., 1999] and Berfield et al [Berfield et al., 2004] have attributed both the decrease in the dielectric constant and longitudinal strain in strain-electric field butterfly loop to the existence of in-plane tensile stress. Lian and Sottos [Lian and Sottos, 2004] have obtained similar results. They have also demonstrated significant changes in the strain-field loops for PZT films by applying a bending moment to the film/substrate combination. Either an in-plane compressive or tensile stress was induced. Lian and Sottos have shown that the residual tensile stress in the PZT films was relieved in the presence of the applied in-plane compressive stress. The 2D clamping effect was reduced and more dipoles were allowed to switch to the electric field direction. Thus, the field-induced strain along the field direction increased accordingly. The butterfly loop shifted upward along the strain axis and the loop area was increased. It was proposed in literature that the shifting of the butterfly loops along the strain axis was mainly due to the elastic deformation of the samples. Conversely, the tensile stress was further amplified in the presence of an external tensile stress. Dipoles were prohibited to switch to the electric field direction. In this condition, the field-induced strain along the field direction decreased. The loop shifted downward and the loop area was reduced.



### 2.1.2 Effect of alternating stress

We have already discussed the effects of static stress on the ferroelectric films. Alternating stress can also exist in the film. The film may be subject to mechanical vibration, either intentionally or unintentionally. In the followings, we will present reviews on experimental results under an alternating stress in three different electric loading conditions: (1) zero field, (2) static field and (3) alternating field.

The hysteretic relations between input fields  $E$  and stress  $\sigma$  and output polarization  $P$  and strains  $\varepsilon$  are not only caused by the ferroelectric switching mechanism, but also ferroelastic switching mechanism. The polarization switching is the result of rotations of individual dipoles under the influences of electric or mechanical stimuli or both. The correlation between the external stimuli and dipolar switching is shown in Figure 2.1. The application of an electric field  $E$  can produce either a  $\pm 90^\circ$  or a  $\pm 180^\circ$  rotation of dipoles whereas the application of a stress  $\sigma$  can only induce a  $\pm 90^\circ$  rotation of the dipole perpendicular to the stress direction.

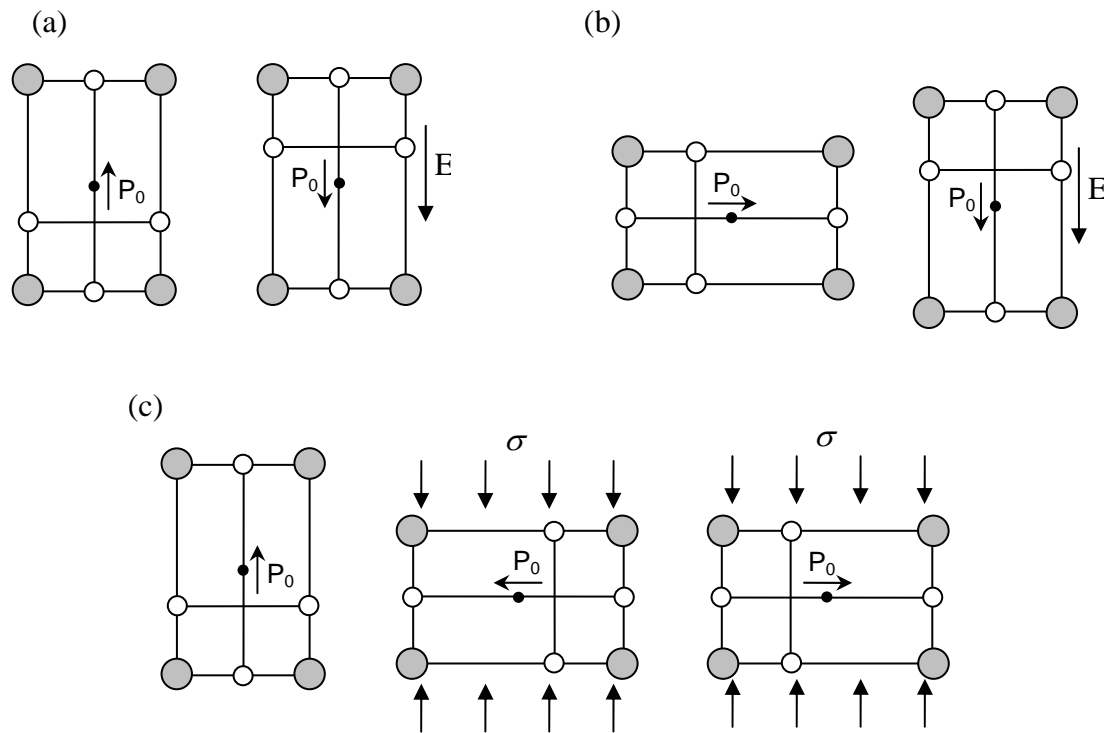


Figure 2.1 Different modes of dipolar switching: (a) 90° switching and (b) 180° switching induced by an applied field; (c) 90° switching induced by an applied mechanical stress



Lynch [Lynch, 1996] and Feng et al. [Feng et al., 2005] have investigated the polarization and strain responses of the poled lanthanum doped PZT and PMN-PT crystals, respectively, under an alternating compressive stress at zero electric field. Typical stress-polarization ( $\sigma$ - $P$ ) and stress-strain ( $\sigma$ - $\varepsilon$ ) curves, similar to Figures 1.3 and 1.4, were obtained from these experiments. The existence of both remanent strains and remanent polarization clearly demonstrates the hysteretic and nonlinear nature of the mechanical properties. Mitrovic et al. [Mitrovic et al., 2001] have reported similar strain responses in PZT-based piezoelectric stack actuators.

Mitrovic have also investigated the strain responses of the piezoelectric stack actuators under an alternating compressive stress in a high static electric field. The loop area of the curve became much smaller than that at zero electric field and the strain-stress loop was clamped into a single line instead of a loop since a much larger stress was required to switch the dipole away from the electric field direction.

Comparing with the number of reports on the effect of alternating stress under a constant or zero electric field, there are only very few discussions on the effect of combined alternating electric and mechanical loadings in the literature. The works of Mitrovic et al. [Mitrovic et al., 2001] and Zhou et al. [Zhou, D. Y. and Kamlah, 2004] are the typical experimental accounts on this topic. Both authors have evaluated the responses of six piezoelectric stack actuators and a commercial soft PZT material under combined



electromechanical loading conditions respectively. The samples were subject to a longitudinal cyclic compressive stress which was either in-phase or out-of-phase with the alternating electric field. For the in-phase condition, the changes in polarization in  $P$ - $E$  loop and strain outputs in  $\varepsilon$ - $E$  loop over a cycle were significantly reduced. On the other hand, in the out-of-phase case, both changes were enhanced. Large hysteresis and nonlinearity were observed in the polarization-electric field and strain-electric field curves. Zhou et al. suggested that, for the in-phase condition, the reduction in polarization and strain changes was mainly due to the prohibition on domain switching to the poling direction; whereas for the out-of-phase case, large amount of non-180° domain switching perpendicular to the poling direction has been induced when electric field was equal to zero. A large amount of domain switching induced during the loading-unloading process caused the significant increase in loop area of the  $P$ - $E$  and the  $\varepsilon$ - $E$  curves.



## 2.2 Theoretical works on ferroelectricity

There are a number of theoretical tools for the study of ferroelectric properties. They include Landau phenomenological theory, first principles calculation and the Monte Carlo simulation of a collection of interacting spins. In this section, we will briefly introduce these methods and review some previous theoretical works on ferroelectrics.

### 2.2.1 Landau Theory

Landau phenomenological theory is a macroscopic approach relating one or a few prominent parameters, such as polarization ( $P$ ), strain ( $\varepsilon$ ), and other macroscopic quantities, such as electric field and stress, in the free energy expression. The free energy  $\hat{F}$  of a ferroelectric material itself can be expressed in power series of polarization, as shown in the following expression:

$$\hat{F} = \frac{\alpha_0(T - T_0)P^2}{2} + \frac{\beta P^4}{4} + \frac{\gamma P^6}{6} + \dots \quad (2.1)$$

where  $\alpha_0$ ,  $\beta$  and  $\gamma$  are the Landau coefficients and  $T_0$  is the Curie-Weiss temperature. The second or first order phase transition of the ferroelectric material can be implemented by the retention of up to the 4<sup>th</sup> or 6<sup>th</sup> order terms in the polarization power series. The higher-order terms, such as  $P^8$  or above, are often neglected in the calculation for simplicity.

In the presence of the electric field  $E$ , an additional term related to the electric field should be included in the free energy expression [Ishibashi et al.,



2005], so that

$$\hat{F} = \frac{\alpha_0(T - T_0)P^2}{2} + \frac{\beta P^4}{4} + \frac{\gamma P^6}{6} - PE \quad (2.2)$$

Incorporating the mechanical contributions, the free energy in a three dimensional space can be written in the following expression: [Pertsev et al., 1998; Pertsev et al., 1999]:

$$\begin{aligned} \hat{F} = & \alpha_1(P_1^2 + P_2^2 + P_3^2) + \alpha_{11}(P_1^4 + P_2^4 + P_3^4) + \alpha_{12}(P_1^2 P_2^2 + P_1^2 P_3^2 + P_2^2 P_3^2) \\ & + \alpha_{111}(P_1^6 + P_2^6 + P_3^6) + \alpha_{112}[P_1^4(P_2^2 + P_3^2) + P_2^4(P_1^2 + P_3^2) + P_3^4(P_1^2 + P_2^2)] \\ & + \alpha_{123}P_1^2 P_2^2 P_3^2 - \frac{1}{2}s_{11}(\sigma_1^2 + \sigma_2^2 + \sigma_3^2) - s_{12}(\sigma_1\sigma_2 + \sigma_2\sigma_3 + \sigma_3\sigma_1) \\ & - \frac{1}{2}s_{44}(\sigma_4^2 + \sigma_5^2 + \sigma_6^2) - Q_{11}(\sigma_1 P_1^2 + \sigma_2 P_2^2 + \sigma_3 P_3^2) \\ & - Q_{12}[\sigma_1(P_2^2 + P_3^2) + \sigma_2(P_1^2 + P_3^2) + \sigma_3(P_1^2 + P_2^2)] \\ & - Q_{44}(P_2 P_3 \sigma_4 + P_1 P_3 \sigma_5 + P_2 P_1 \sigma_6) \end{aligned} \quad (2.3)$$

where  $\sigma_n$  are the internal mechanical stresses in the film,  $\alpha_i$ ,  $\alpha_{ij}$  and  $\alpha_{ijk}$  are the dielectric stiffness coefficients,  $s_{mn}$  are the elastic compliances at constant polarization,  $Q_{mn}$  are the electrostriction coefficients and subscripts 1, 2 and 3 represent the  $x$ ,  $y$  and  $z$  axes of ferroelectric thin films whereas subscripts 4, 5 and 6 represent the direction of the shear stress, respectively. The basic procedure of solving Eqn. (2.3) is to equilibrate the system by minimizing the free energy such that:

$$\frac{\partial F}{\partial P} = 0 \quad (2.4)$$



The phase transformation characteristics can also be tackled by Landau Theory through the comparison of free energies of different phases under the same conditions. For a dynamic problem such as the polarization switching, Landau-Khalatnikov equation has been used [Ishibashi et al., 2005]:

$$\gamma \frac{dP}{dt} = - \frac{\partial F}{\partial P} \quad (2.5)$$

where  $\gamma$  is a viscosity coefficient.

There are numerous examples of using Landau theory to simulate different phenomena in ferroelectrics. For instance, Pertsev et al. have studied the stability of ferroelectric phase and the shift in Curie temperature under different interfacial stresses using Landau theory. The calculated  $T_c$  increases with the in-plane compressive stress but decreases with in-plane tensile stress. The disappearance of ferroelectricity can also be obtained when the film is under sufficient in-plane tensile stress. G.A. Rossetti Jr. et al. [Rossetti et al., 1991] have obtained similar results. The simulated results agree with the experimental observations. Moreover, Pertsev et al. have calculated polarization distributions in polydomain  $\text{PbTiO}_3$  (PT) and  $\text{BaTiO}_3$  (BT) films grown on cubic substrates and simulated their dielectric properties [Pertsev and Koukhar, 2000] using Landau theory. The stability of each phase was related to the temperature and pressure.



Song et al. [Song et al., 2003] have investigated the effect of static stress on the  $P$ - $E$  hysteresis using the Landau-Khalatnikov equation. By making the following assumptions:  $P_1 = P_2 = 0$  and  $\sigma_3 = \sigma_4 = \sigma_5 = \sigma_6 = 0$ , Eqn. (2.3) can be simplified as follow:

$$\hat{F} = \alpha_1 P^2 + \alpha_{11} P^4 + \alpha_{111} P^6 - Q_{12}(\sigma_1^2 + \sigma_2^2)P^2 - EP \quad (2.6)$$

The Landau- Khalatnikov equation can then be obtained by substituting the free energy expression into Eqn. (2.5). From their computational results, the polarization and coercive field increased with the in-plane compressive stress and decreased with the in-plane tensile stress. Furthermore, Zhang et al. [Zhang, W. and Bhattacharya, 2005] have demonstrated the effect of static longitudinal stress on the  $P$ - $E$  hysteresis and  $\varepsilon$ - $E$  butterfly loops. The coercive field decreased as the longitudinal compressive stress increased. The strain increased for small applied stress and it began to decrease beyond a critical stress for a fixed amplitude of the applied electric field.

While there are numerous successful examples of simulating the phase diagram,  $P$ - $E$  hysteresis and  $\varepsilon$ - $E$  butterfly loops of both bulk ferroelectrics and ferroelectric films, Landau theory is restricted to be a macroscopic description. As the system size is decreasing down to atomic scale, the microscopic processes and structures are then overlooked by this phenomenological approach. It fails to tackle the dynamics of individual dipoles which is vitally important for polarization switching.



### 2.2.2 First principles calculation

First principles calculation, on the other hand, has been used to study of ferroelectrics from the level of electronic structure. Most properties of solids, including ferroelectric materials, can be traced to the arrangement and behavior of the electrons that make up the solid. In first principles (i.e. *ab initio*) electronic structure calculations, the solid is regarded as a particles system that consists of electrons and nuclei. Based on the Density-Functional Theory (DFT), it is capable of predicting various physical properties at 0K, such as formation energy, volume and bulk modulus by implementing fundamental quantum theory and finding a solution to the time-independent Schrödinger equation.

The first principles calculation can be classified into two types: the direct first-principles and the first-principles-based method. Based on the basic formula of quantum mechanics and some reasonable approximations, the direct first-principles approaches were able to provide the total energy forces and stress of a given crystal. The ground state of the system was then confirmed from the relation between the total energy, electronic structure and nucleus configuration. Optical properties and ferroelectric properties can then be calculated from this approach. However, it failed to study ferroelectrics under an external electric field. For the first-principles-based method, one of the most commonly used approaches was the effective Hamiltonian scheme, which has first been developed for simple perovskite and then extended for studying ferroelectric solid solutions. In this approach, an analytical expression of the



total internal energy  $U$  is derived, depending only on a few degrees of freedom. The parameters of the analytical expression of  $U$  are determined by fitting to the results of first-principles calculations on small cells. Once the effective Hamiltonian is fully specified, its total internal energy can be used in Monte-Carlo or molecular dynamics simulations on large supercells to compute finite-temperature properties of ferroelectrics. The piezoelectric coefficients can be calculated by using this approach.

In recent years, the first principles calculations have been widely used in studying the phase transitions and the ferroelectricity of the perovskite-type ferroelectrics. Numbers of publications in the literature have shown that the cell size was very important to the ferroelectricity of perovskite ferroelectrics. Zhong and Vanderbilt [Zhong et al., 1994; Zhong et al., 1995] have developed a first-principles scheme to study perovskite-type ferroelectrics. They constructed an effective Hamiltonian based on Taylor expansion of the energy surface around the cubic structure and determined the expansion parameters by first-principles density-functional calculations. The calculated phase sequence, transition temperatures, latent heats and spontaneous polarizations agreed with experimental results well. Wang et al. [Wang, Y. X. et al., 2002] have also demonstrated the cell volume effect on ferroelectricity. They have used the first principles calculations to calculate the electronic structure of  $\text{CaTiO}_3$ ,  $\text{SrTiO}_3$  and  $\text{BaTiO}_3$  in order to understand the ferroelectric behavior of quantum paraelectrics and ferroelectrics and the origin of the ferroelectricity. From total energy analysis, Wang et al. have shown that the displacement of Ti along [001]



direction of  $\text{CaTiO}_3$  and  $\text{SrTiO}_3$  resulted in a shallow, but well-defined double energy well and ferroelectricity appears with increasing cell volume, whereas the ferroelectricity of  $\text{BaTiO}_3$  will disappear as the cell volume is decreased. Bellaiche [Bellaiche, 2002] have studied the piezoelectricity of ferroelectric perovskites by the first principles approach. Furthermore, Vanderbilt has shown the intrinsic hysteresis behavior of the polarization and the susceptibility of tetragonal  $\text{PbTiO}_3$  as a function of electric field applied along the tetragonal axis based on the first principles density-functional methods.

Comparing with other theoretical tools, the direct first-principles calculations do not require experimental information as an input. These calculations are generally applicable to any structure and any element in the periodic table. Thus, the results from the first principles calculation are accurate and the calculation is independent of experimental data. Moreover, it can provide a microscopic picture of piezoelectric effects. Unfortunately, it is very difficult to obtain the analytic or exact numerical solutions for system involving large numbers of atoms. Since the structure of conventional perovskite-type ferroelectrics is much more complicated and most of them contain heavy metals, it requires much more calculations in order to obtain more accurate results. Furthermore, special simulation software, such as VASP, and a supercomputer are required for the tedious calculations.



### 2.2.3 Ising and Potts models

In Ising model or  $q$ -state Potts models, the focus is on the dynamics of individual dipoles, or referred to pseudo-spins as this concept was borrowed from ferromagnetism. The arrangement of spins in Ising model can be graphically represented in a 2D array:

↓	↑	↑	↓	↓
↓	↓	↑	↑	↓
↑	↑	↓	↓	↑
↑	↑	↓	↑	↑
↑	↓	↓	↓	↑

Figure 2.2 The configuration of spins in a 2D array

The ensemble of dipoles in a particular configuration gives rise to a value of system Hamiltonian which includes the mutual interactions between dipoles and the external influences. The rotation of even one single dipole leads to the change in configuration and hence the system Hamiltonian. Whether or not this change is probable is governed by the change in Hamiltonian, as described by Metropolis algorithm [Newman and Barkema, 1999]. Statistical physics establishes a bridge between these microscopic mechanisms and macroscopic observable quantities such as polarization and strains. However, a large sample size is required to minimize the perturbation of a statistical system.



The difference between Ising and Potts model is that there are only two anti-parallel dipole orientations in Ising model while in the  $q$ -state Potts Model the number of dipole orientations can be extended to  $q \geq 3$ . One dimensional Ising model was first introduced by Lenz in 1920. Lars Onsager [Onsager, 1944] solved problems with two dimensional Ising model in 1944 [Onsager, 1944]. On the other hand, Ashkin and Teller has extended to the number of dipole orientations to four in 1943, even though the standard name “Potts model” appeared much later after Domb has suggested this term as a research topic to his Research Student Potts.

Both Ising and Potts models have been used to study phase transitions and critical phenomena in ferromagnetism. It was then extended to study the corresponding behaviors in ferroelectric systems. The similarity between ferroelectricity and ferromagnetism is the presence of permanent dipoles: being electric for the former and magnetic for the latter. There are a number of examples of simulating ferroelectric properties based on Ising model and Potts model. Lo [Lo, 2002] has used the Ising model to model the role of oxygen vacancy on ferroelectric properties in thin films. Qian et al. [Qian and Bursill, 1996] have successfully demonstrated the dielectric breakdown in PMN-PT film whereas Li et al. [Li, K. T. and Lo, 2004] have studied the thickness dependence on ferroelectric thin films by using two-dimensional four-state Potts model. Moreover, Liu [Liu, 1999] has used the  $q$ -state Potts model to describe the kinetics of partial polarization reversal in a multi-grained system under an external electric field. We have presented the effects of stress in phase



transition temperature,  $P$ - $E$  loop and  $\varepsilon$ - $\sigma$  loop [Cao et al., 2006] using four-state Potts model in a two dimensional systems. We will elaborate our model in Chapter 3.



## Chapter 3 Theory and numerical simulation

### *3.1 Formulation of our Models*

In our project, we have established a theoretical framework to simulate the electromechanical properties in nanometer scale (in atomic or cell levels). It can tackle the detailed switching mechanism of individual dipoles and hence the whole domain. From both Ising and Potts models, the dynamics of individual dipoles is governed by the system Hamiltonian which includes the mutual interactions between dipoles as well as the external influences. However, the conventional Ising or Potts models only include contributions from dipole-dipole and electric-field-dipole couplings in the system Hamiltonian. As mentioned previously, stress is important in the electromechanical properties in ferroelectric films. This factor must be incorporated in the Hamiltonian. Therefore, a modified two-dimensional planar-type four-state Potts model has been established in order to simulate the electromechanical properties under both electrical and mechanical loadings.



### 3.1.1 Two-dimensional four-state Potts model

A real system is in three-dimensions. However, the computational cost to simulate problems in three-dimensional space is usually very high. It is worthwhile to approximate the three-dimensional problem by a two-dimensional one if most of the physical features are retained and if the features along one of the axis can be replaced or is totally equivalent to those along the other axis. For our present problem, the numerical simulation of a ferroelectric thin film lying on the  $xy$  plane, where there is no distinction for properties along  $x$ - or  $y$ - direction. On the other hand, if the film is discretized into an array of cells in three-dimensional space: the numbers of cells are then  $N_x$ ,  $N_y$ , and  $N_z$ , respectively, along  $x$ -,  $y$ - and  $z$ - directions. In our work, we have adopted  $N_x = 150$ ,  $N_z = 80$ .  $N_y$  will also be equal to 150 because of the equivalence in  $x$ - and  $y$ - directions. The number of grid points will then be equal to  $150^2 \times 80 = 1.8 \times 10^6$ ! The computation will be very inefficient. This justifies the adoption of two-dimension in our simulation.

Both Ising model and Potts model with  $q > 4$  have been used to simulate ferroelectric properties before. The former restricts only uniaxial dipole orientations [Duiker and Beale, 1990; Lo, 2002] even though experiments suggested that non-180° domain wall movement is the dominant switching mechanism [Li, K. T. and Lo, 2005]. The different states in the latter model has been used to represent different grain orientations in a polycrystalline system instead of a multidomained one [Liu, 1999]. It must impose some assumptions on the relation between grain boundary and domain wall. On the other hand, the widely used ferroelectric ceramics never involves just two states. The



experimental evidence confirmed the co-existence of  $90^\circ$  and  $180^\circ$  domain walls [Nagarajan et al., 1999; Saito et al., 2003] and the origin of electromechanical coupling effect by non- $180^\circ$  domain wall movement. The four-state Potts model should then be a better choice because it is comprehensive enough to tackle the non- $180^\circ$  domain-wall switching but simple enough to keep the number of states to minimum. Consequently, the four-state Potts model is applicable to single crystalline thin film with dipoles orientated normal or parallel to the film. The epitaxial polycrystalline film is also highly oriented that the validity of this model can also be extended to polycrystalline thin film case.

In our model, the ferroelectric thin film can be represented by a two-dimensional array of cells. Each of these cells represents a single perovskite tetragonal cell in the  $x$ - $z$  plane. As shown in Figure 3.1, the size of the film can be described by a pair of integers  $N_x$  and  $N_z$  to represent numbers of cells along the  $x$ - (or transverse) and  $z$ - (or longitudinal) directions, respectively. As has been discussed previously, [Li, K. T. and Lo, 2004; Li, K.T., 2005; Li, K. T. and Lo, 2005], the location of each cell can be represented by a pair of indices  $(i, j)$ , where  $0 < i < N_x$  and  $0 < j < N_z$ .

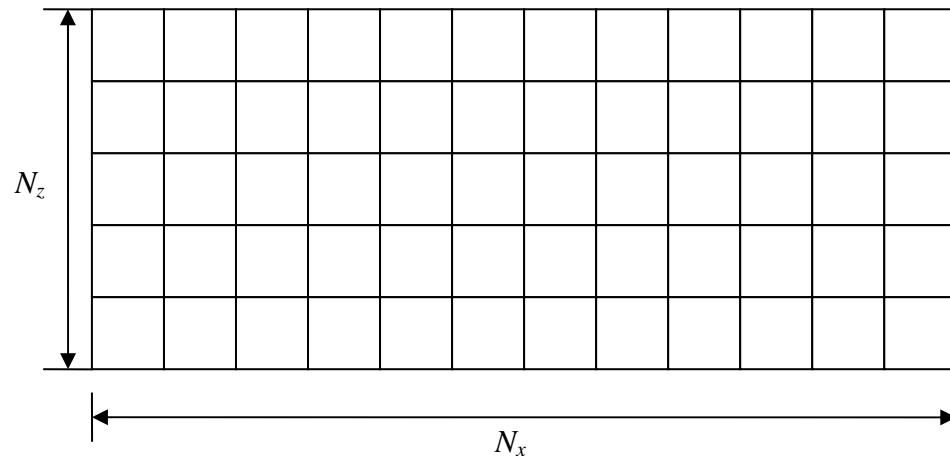
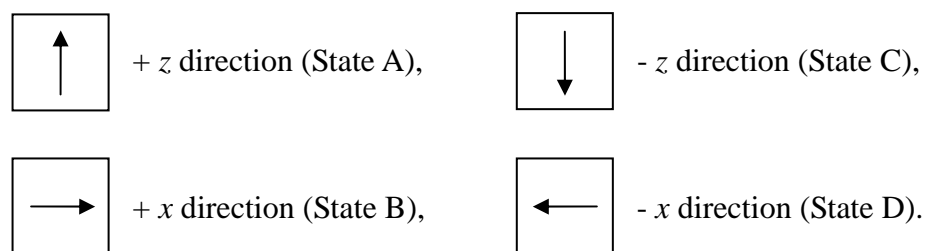


Figure 3.1 The ferroelectric film is represented by the two-dimensional array of cells (rectangles).

In the four-state Potts model, each dipole (pseudo-spin) is assigned to one of the four possible states which are mutually perpendicular to each other shown as follows:



There are quite a number of authors used the concept of “pseudo-spin” to represent the effect of dipoles in ferroelectric materials [Buzano et al., 1980; Chaudhuri et al., 1980; Wada et al., 2001; Yao et al., 2002].



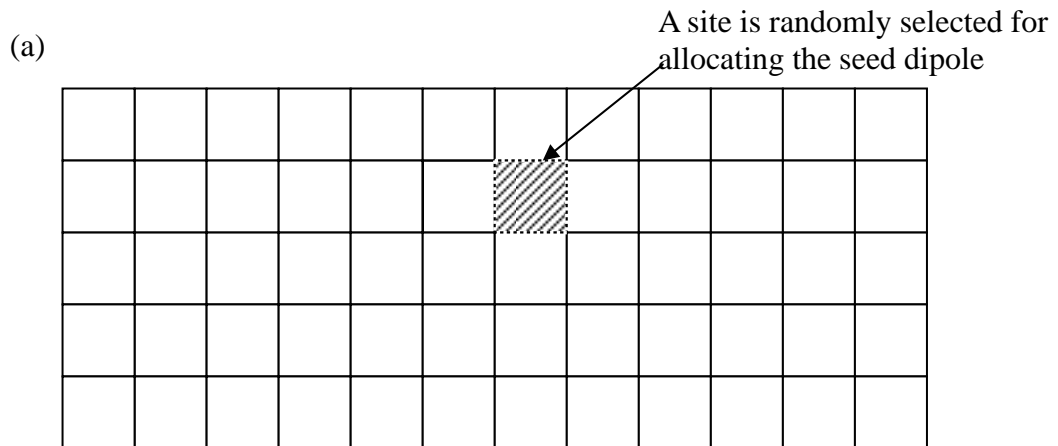
### 3.1.2 Initialization of domains

The ferroelectricity can be characterized by a system of strongly interacting dipoles and the presence of domains. The other reason for the existence of domains is to minimize the system energy. Domains exist even for an unpoled sample below  $T_c$ . In such situation, the volume fractions of domains in opposite directions must be equal. This is the basis for us to initialize the domain configuration in an unpoled sample.

There are two important parameters for the initialization: the average domain size  $\delta$  and volume fraction of  $c$ -domains  $\phi_c$ . The orientation of a  $c$ -domain is normal to the film (with dipoles are in either  $A$  or  $C$  states). Likewise, the orientation of an  $a$ -domain is parallel to the film (with dipoles are in either  $B$  or  $D$  states). The volume fraction of  $a$ -domains is  $1 - \phi_c$ . The number of domains in the system can thus be related by

$$N_D = \frac{N_x N_z a_0 c_0}{\delta^2} \quad (3.1)$$

where  $a_0$  and  $c_0$  are the transverse and longitudinal edges, respectively of the rectangle. Seed dipoles, in a number  $N_D$ , are the randomly allocated inside the film, Figure 3.2. The orientation of a seed dipole is then determined by the probability  $\phi_c$  and random number  $r_1$  and  $r_2$  (where  $0 < r_1 < 1$  and  $0 < r_2 < 1$ ), as expressed by the following algorithm (Figure 3.3).



For  $\phi_c = 0.6$  and  $r_1 \leq 0.6$ , the orientation of the seed dipole would be longitudinal:



For  $\phi_c = 0.6$  and  $r_1 > 0.6$ , the orientation of the seed dipole would be transverse:

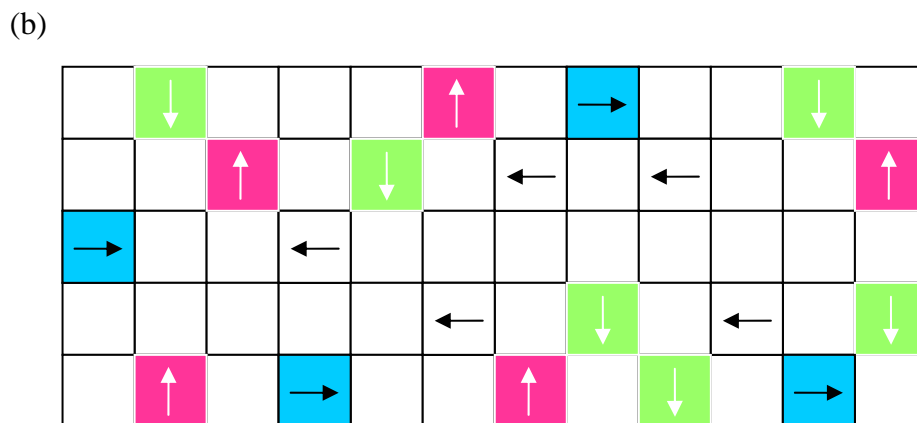
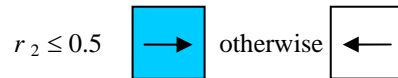


Figure 3.2 (a) A state is assigned to a randomly-selected site according to  $\phi_c$  and the random numbers  $r_1$  and  $r_2$ . (b) A prescribed number of seed dipoles  $N_D$  are randomly assigned in the film.

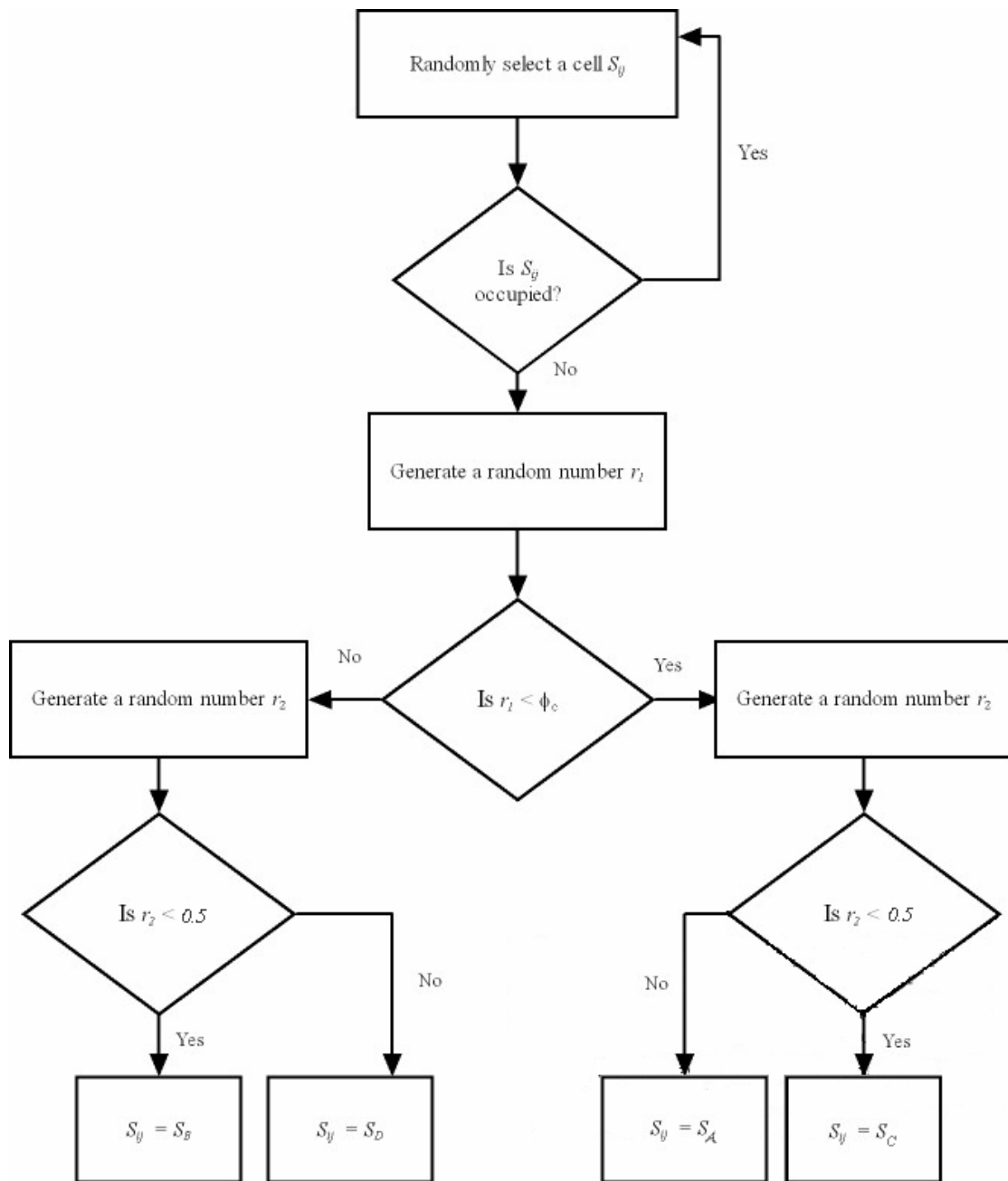
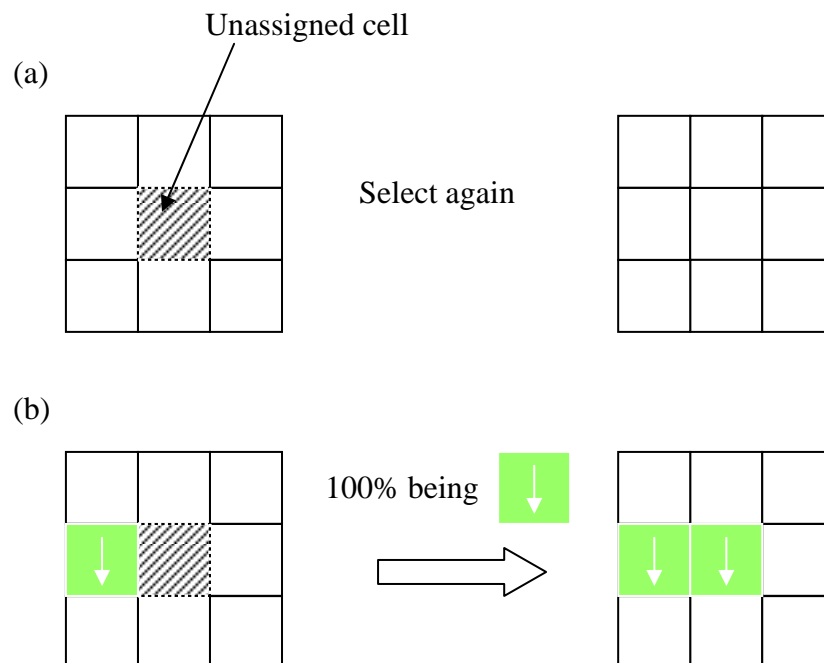
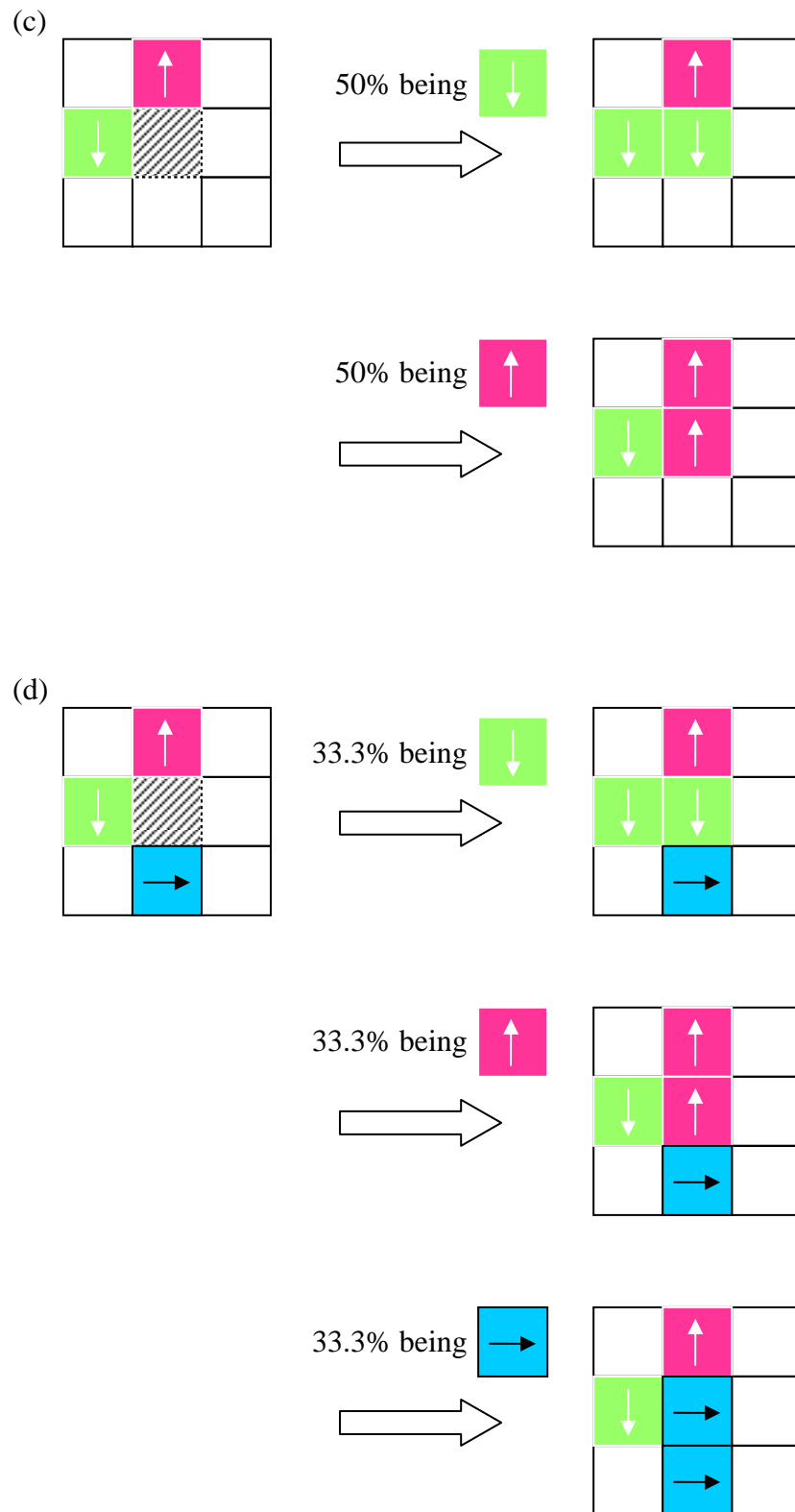


Figure 3.3 The algorithm to determine the state of the seed dipole.



After the assignment of these seed dipoles into the film, domains are generated as described before [Li, K. T. and Lo, 2004; Li, K.T., 2005; Li, K. T. and Lo, 2005]. An unassigned site is randomly selected. When there are no assigned cells next to it as shown in Figure 3.4 (a), another cell has to be selected again. Each domain is formed by aligning the unassigned neighboring cells to the same state with the assigned cells as shown in Figure 3.4 (b). However, for the unassigned cell at the boundary of two different domains as shown in Figure 3.4 (c), there are two possibilities for the unassigned cell to be aligned with equal probabilities. Similar assignment of state for an unassigned cell with neighboring cells of three or even four different states follows a similar rule, as shown in Figure 3.4 (d) and (e), respectively. The “growth” proceeds until the states of all the cells have been assigned as shown in Figure 3.5 (c).





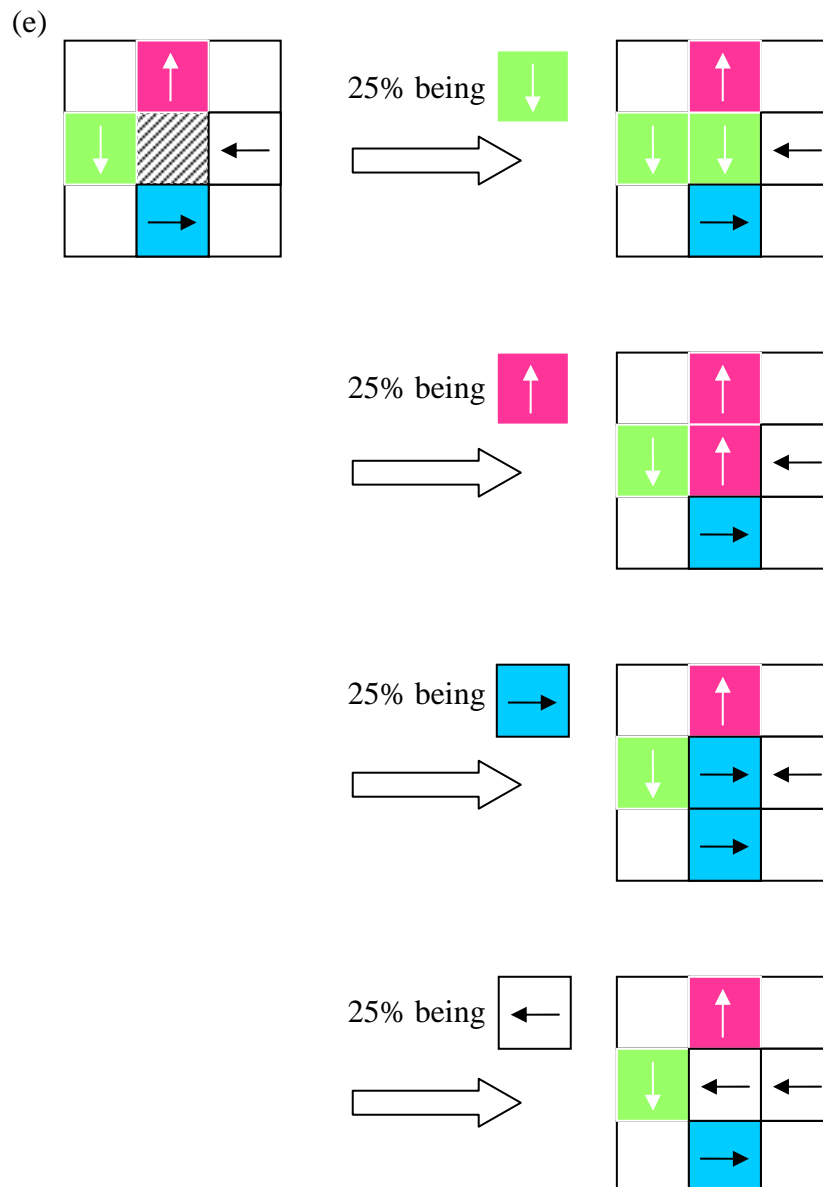


Figure 3.4 (a) Another cell has to be selected again when there is no even one assigned neighboring cell. (b) In the presence of only one assigned neighboring cell, the unassigned cell will be assigned to the same state as this neighboring cell. (c) In the presence of two assigned neighboring cells with different states, the unassigned cell will be assigned to either one of these states with equal probabilities. Similar procedure is taken for assigning the unassigned selected cell if there are three or four assigned neighboring cells, as in (d) and (e).

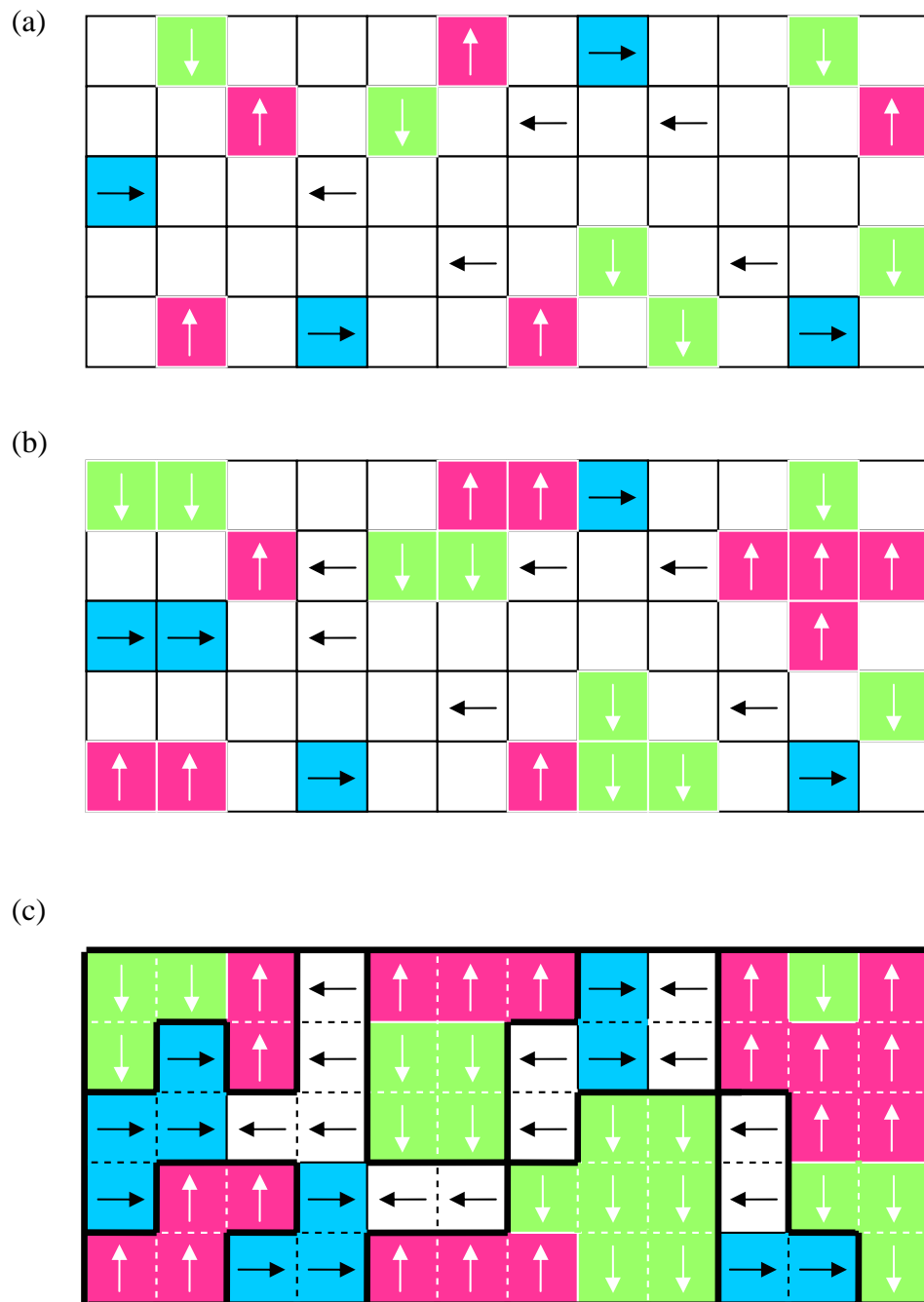


Figure 3.5 The steps for constructing domain configuration: (a) allocating the seed dipoles, (b) assigning the state of the unassigned neighboring cells, (c) repeating (b) until all cells are assigned.



### 3.1.3 System Hamiltonian

Considering only the coupling between neighboring dipoles, the Hamiltonian can be generally expressed as

$$H = -\sum_{i,j} J(\theta_{i,j}) \quad (3.2)$$

for  $q$ -state Potts model, where  $J(\theta_{i,j})$  is the coupling function,  $\theta_{i,j} = \theta_{n_i} - \theta_{n_j}$  is the angle between two dipole states  $n_i$  and  $n_j$ ,  $\theta_n = 2\pi n/q$ , and  $n < q-1$ . Wu [Wu, 1982] have made a review on two different forms of Potts model: the standard and the planar Potts model. For the former one, the coupling function  $J(\theta_{i,j})$  can be written as

$$J(\theta_{i,j}) = \beta_1 \delta(n_i, n_j) \quad (3.3)$$

where

$$\delta(n_i, n_j) = \frac{1}{q} [1 + (q-1) e^{n_i} \cdot e^{n_j}] \quad (3.4)$$

$n_i, n_j = 0, 1, \dots, q-1$ ,  $e^{n_i}$  and  $e^{n_j}$  are  $q$  unit vectors pointing toward  $q$  symmetric directions of a hypertetrahedron, and  $\beta_1$  is a constant. For the planar Potts model, the coupling function  $J(\theta_{i,j})$  is given by

$$J(\theta_{i,j}) = \beta_2 \cos(\theta_{i,j}) \quad (3.5)$$

where  $\beta_2$  is another constant. From Eqn. (3.5), the interacting dipoles of dissimilar orientations yield a higher energy than those with the same orientation.

In the presence of an electric field  $E_{i,j}$ , an additional term should be added to the



Hamiltonian as follow:

$$H = -\sum_{i,j} J(\theta_{i,j}) - \sum_i P_0 \cdot E \cos(\theta_i) \quad (3.6)$$

where  $P_0$  is the magnitude of the dipole moment.

In our work, the planar-type Potts model has been chosen for the simulation. With  $q = 4$ , the possible angles between two adjacent dipoles are:  $\theta_n = 0, \pi/2, \pi, 3\pi/4$ . From Eqn. (3.5), the following values of the coupling function  $J(\theta_{i,j})$  can be obtained:

$$\begin{aligned} J(\theta_{i,j}) &= \beta_2 && \text{if the two interacting dipoles are parallel,} \\ J(\theta_{i,j}) &= -\beta_2 && \text{if they are anti-parallel,} \\ J(\theta_{i,j}) &= 0 && \text{if they are perpendicular to each other.} \end{aligned}$$

It is convenient to represent this coupling function by the product of two pseudo-spin matrices, in order to retain the original form in the Hamiltonian. The pseudo-spin matrix  $\hat{S}_{i,j}$  of a cell located at  $(i, j)$  has the following values in different orientations:

$$\begin{aligned} \hat{S}_{i,j} = \hat{S}_A &= \begin{pmatrix} 1 \\ 0 \end{pmatrix} \text{ (+z direction),} & \hat{S}_{i,j} = \hat{S}_C &= \begin{pmatrix} -1 \\ 0 \end{pmatrix} \text{ (-z direction),} \\ \hat{S}_{i,j} = \hat{S}_B &= \begin{pmatrix} 0 \\ 1 \end{pmatrix} \text{ (+x direction),} & \hat{S}_{i,j} = \hat{S}_D &= \begin{pmatrix} 0 \\ -1 \end{pmatrix} \text{ (-x direction),} & (3.7) \\ \hat{S}_{i,j} = \hat{S}_0 &= \begin{pmatrix} 0 \\ 0 \end{pmatrix} \text{ (dipole is absent).} \end{aligned}$$



The coupling function in Eqn. (3.5) can be replaced by  $\{\hat{S}_{i,j}^T \hat{S}_{k,l}\}$  where  $\hat{S}_{i,j}^T$  is the transpose matrix of  $\hat{S}_{i,j}$ . This function returns one of the following values: + 1 if the two spins are parallel; -1 if they are anti parallel and 0 if they are perpendicular. The system Hamiltonian can now be expressed as:

$$H = - \sum_{i,j,k,l} J \{\hat{S}_{ij}^T \hat{S}_{kl}\} - P_{SAT} \sum_{i,j} \{\hat{E}^T \hat{S}_{ij}\}, \quad (3.8)$$

where  $J$  is the coupling coefficient,  $P_{SAT}$  is the magnitude of the saturated polarization,  $\hat{E}^T$  is the transpose matrix of  $\hat{E}$  and  $\hat{E}$  is the matrix representation of the electric field as shown in the following form:

$$\hat{E} = \begin{pmatrix} E_3 \\ E_1 \end{pmatrix} \quad (3.9)$$

where  $E_3$  and  $E_1$  are longitudinal ( $z$ -direction) and transverse ( $x$ -direction) components, respectively. In order to be consistent with the notation conventionally adopted in the literature, all components along  $z$ -direction are denoted by the subscript “3” and those along  $x$ -direction are denoted by “1”. In our work, only the longitudinal electric field is applied to the system (i.e.,  $E_3 \neq 0$  and  $E_1 = 0$ ) throughout the calculation.

In additional to the first two terms in Eqn. (3.8), the coupling effects between the neighboring cells due to the distortion, as well as the mechanical energy density are incorporated into the system Hamiltonian. Moreover, there are three different contributions of strains: ferroelastic, elastic and piezoelectric. For the first one, the distortion of cell is associated with the dipole orientation, as



shown in Table 3.1. Hence, one can also define a ferroelastic strain state which is associated with the pseudo-spin state [Li, W. F. and Weng, 2002]. These states are defined in Eqns. (3.10).

Dipole	Corresponding strain states	
$S_A, S_C$	$\epsilon_a = \begin{pmatrix} \epsilon_0 \\ -\epsilon_0/2 \end{pmatrix}$	
$S_B, S_D$	$\epsilon_b = \begin{pmatrix} -\epsilon_0 \\ \epsilon_0/2 \end{pmatrix}$	

Table 3.1 Association between dipole states and ferroelastic strain states of perovskite cell.

$$\hat{\epsilon}^F_{ij} = \hat{\epsilon}_a = \begin{pmatrix} \epsilon_0 \\ -\epsilon_0/2 \end{pmatrix} \text{ (for the dipole in either state A or C)}$$

and (3.10)

$$\hat{\epsilon}^F_{ij} = \hat{\epsilon}_b = \begin{pmatrix} -\epsilon_0 \\ \epsilon_0/2 \end{pmatrix} \text{ (for the dipole in either state B or D),}$$

where  $\epsilon_0$  is a reference strain due to ferroelastic switching. Again the indices  $i$  and  $j$  refer to the location of the cell. Because of the invariance of volume upon deformation of a cell, the magnitude of the transverse strain is one-half of the longitudinal value, and the signs of both directions are opposite. Moreover, both tensile stress and strain take positive sign and their compressive counterparts negative.



The second strain component is due to the elastic effect, i.e., an object deforms elastically in the presence of a mechanical stress. The stress-strain relation can be divided into two regions. For most of the materials, it must be a linear region followed by a nonlinear region. Calderon-Moreno [Calderon-Moreno, 2001] has demonstrated the stress-strain behaviors in hard and soft PZT materials. The strain of samples increases linearly when the stress is small and it becomes nonlinear as the stress further increases. The increase in strain becomes smaller and smaller at high compressive values. We have set a nonlinear model between the strain and stress. The relation between stress and strain is shown in Figure 3.6.

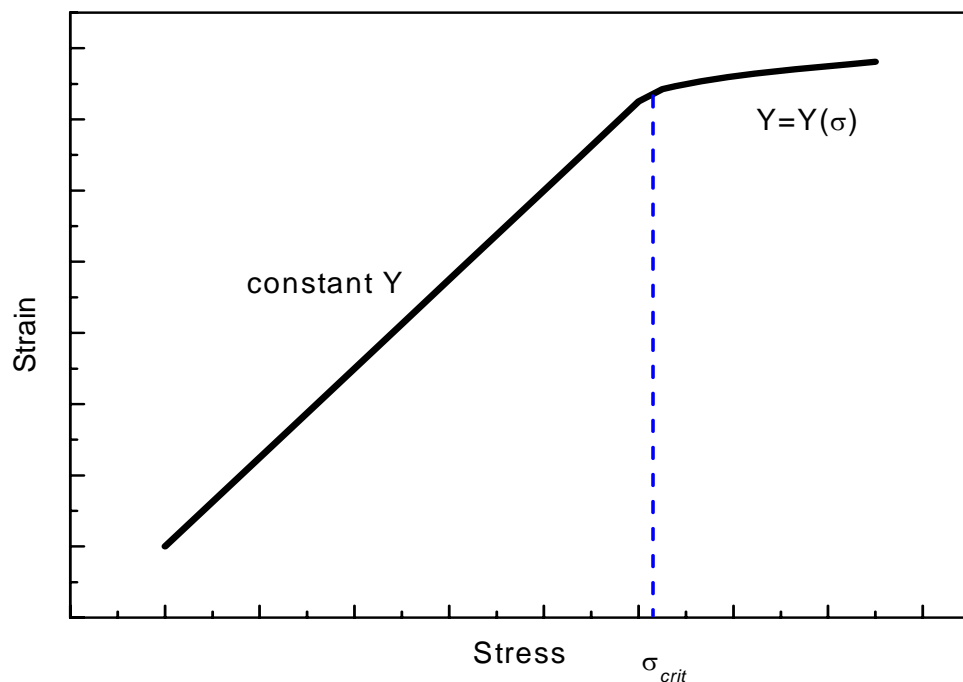


Figure 3.6 Nonlinear relation between stress and strain



The stress and strain relation is given as follows:

$$\hat{\varepsilon}_{ij}^{el} = \begin{pmatrix} \varepsilon_3^{el} \\ \varepsilon_1^{el} \end{pmatrix} = \frac{1}{Y} \begin{pmatrix} 1 & -\nu \\ -\nu & 1 \end{pmatrix} \begin{pmatrix} \sigma_3 \\ \sigma_1 \end{pmatrix} \quad \text{if } \sigma_3 < \sigma_{crit} \quad (3.11)$$

and

$$\begin{aligned} \varepsilon_3^{el} &= \frac{\sigma_{crit}}{Y} + k|(\sigma_3 - \sigma_{crit})|^n - \nu \frac{\sigma_1}{Y} \\ \varepsilon_1^{el} &= \frac{\sigma_1}{Y} - \nu \left[ \frac{\sigma_{crit}}{Y} + k|(\sigma_3 - \sigma_{crit})|^n \right] \quad \text{if } \sigma_3 > \sigma_{crit} \end{aligned} \quad (3.12)$$

where  $Y$  is the Young's modulus,  $\nu$  the Poisson ratio,  $\sigma_{crit}$  upper limit for the linear region,  $k$  and  $n$  are the shape parameter for the nonlinearity.  $\sigma_3$  and  $\sigma_1$  are, respectively, the longitudinal and transverse stress components. The relation in Eqns. (3.12) is a mathematical model to reflect the nonlinearity. It produces the stress-strain relation which is similar to the one obtained from experiments. The critical stress and the shape of curve in the nonlinear region have to be determined from experiments.

Finally, the presence of external electric field also induces the displacements of charges in each cell. This will in turn create distortion to the cell. Notice that, unlike the ferroelastic effect which leads to the switching of dipoles, we only consider the distortion of cell due to the displacements of charges. The general expression for this electric field-induced strain is [Strukov and Levanyuk, 1998]

$$\varepsilon_{mn} = d_{mnk} E_k + q_{mnkl} E_k E_l \quad (3.13)$$

where  $d_{mnk}$  and  $q_{mnkl}$  are piezoelectric and electrostriction tensors, respectively. In Eqn. (3.13), the index “ $m$ ” refers to the direction of the distortion and “ $n$ ” to the



normal of the cell surface. Thus,  $\varepsilon_{mm}$  is the normal strain and  $\varepsilon_{mn}$  is the shearing strain (for  $m \neq n$ ). If we ignore the shearing strain, then we can merge the two indices into one, such that  $\varepsilon_{mm} = \varepsilon_m$ . The field-induced strain is then given by

$$\begin{aligned} \left(\varepsilon_3^E\right)_{ij} &= d_{33}E_3 + d_{31}E_1 + q_{333}E_3^2 + q_{313}E_1E_3 + q_{331}E_3E_1 + q_{311}E_1^2 \quad \text{and} \\ \left(\varepsilon_1^E\right)_{ij} &= d_{13}E_3 + d_{11}E_1 + q_{133}E_3^2 + q_{113}E_1E_3 + q_{131}E_3E_1 + q_{111}E_1^2 \end{aligned} \quad (3.14)$$

where subscripts “3” and “1” refer to their directions and the subscripts “ $ij$ ” corresponds to the location of the cell. In the absence of the transverse electric field component  $E_l = 0$ , and with symmetric property:  $d_{13} = d_{31}$ , Eqn. (3.14) can be simplified into

$$\begin{aligned} \left(\varepsilon_3^E\right)_{ij} &= d_{33}E_3 + q_{333}E_3^2 \quad \text{and} \\ \left(\varepsilon_1^E\right)_{ij} &= d_{13}E_3 + q_{133}E_3^2 \end{aligned} \quad (3.15)$$

The strain matrix is

$$\hat{\varepsilon}_{ij}^E = \begin{pmatrix} \left(\varepsilon_3^E\right)_{ij} \\ \left(\varepsilon_1^E\right)_{ij} \end{pmatrix} \quad (3.16)$$

The total strain is thus the superposition of the three contributions: ferroelastic, elastic and field induced, as shown in the following expression:

$$\hat{\varepsilon}_{ij} = \hat{\varepsilon}_{ij}^F + \hat{\varepsilon}_{ij}^{el} + \hat{\varepsilon}_{ij}^E \quad (3.17)$$

The system Hamiltonian can now be expressed as

$$H = - \sum_{i,j,k,l} J \{ \hat{S}_{ij}^T \hat{S}_{kl} \} - P_{SAT} \sum_{i,j} \{ \hat{E}^T \hat{S}_{ij} \} - \sum_{i,j} \{ \hat{\sigma}^T \hat{\varepsilon}_{ij} \} - \alpha \sum_{i,j,k,l} \hat{\varepsilon}_{ij}^{F,T} \hat{\varepsilon}_{kl}^F + H' \quad (3.18)$$

where  $\alpha$  is the coupling coefficient between neighboring strain states and  $\hat{\sigma}$  the



stress matrix. The first and second terms in Eqn. (3.18) are the coupling effects between neighboring dipoles and between dipoles and the electric field, as in the conventional Hamiltonian. The third one is the mechanical energy density. The fourth term is the coupling between neighboring strain states. As mentioned previously, the ferroelectric film is represented by a two-dimensional array of rectangles. In reality, dipoles with different ferroelastic strain states are not simply joined together. Domain walls exist in this region. Unit cells may be distorted or strain gradient may exist. Thus, a strain-strain coupling term is implied into the model. In Landau theory, similar term has been adopted to express the strain gradient inside the system. In our work, only the interaction between the first nearest neighbors is considered for simplicity. Finally, the last term  $H'$  tackles the effect of anisotropy switching. We will elaborate the anisotropy effect later.



### 3.2 *Boundary conditions*

We are considering a thin film system where the transverse size is much larger than the thickness. Consequently, we adopt periodic boundary condition for the two transverse edges and free boundary condition for the top and bottom surfaces. Periodic boundary condition has been widely used to tackle a system of infinite size [Binder and Heermann, 2002] since it is impractical to implement an “infinite” system. The basic strategy is to remove the effect of surface by setting the points at the boundary as ‘internal’ points to ensure that the internal effect must dominate over the surface effect. The reason of adopting free boundary condition for the top and bottom surfaces is that the dipoles disappear there and there is no coupling effect from these surfaces. In mathematical expressions, these boundary conditions can be written as follows:

$$\hat{S}_{0,j} = \hat{S}_{N_x,j} \quad \text{and} \quad \hat{S}_{N_x+1,j} = \hat{S}_{1,j}, \quad (\text{Periodic boundary condition along the transverse direction})$$

(3.19)

$$\hat{S}_{i,0} = \hat{S}_{i,N_z+1} = \hat{S}_0.$$

(Free boundary condition along the longitudinal direction)



### 3.3 *c*-domain volume fraction and anisotropic switching

While we have shown that the presence of stress in thin film influences ferroelectric properties, the orientation of the film also plays an important role. It was reported that an *a*-axis-oriented film has a higher room-temperature dielectric constant than a *c*-axis-oriented film. For instance, Tuttle et al. [Tuttle et al., 1992] have shown that the PZT 40/60 films in a high degree of *c*-axis (001) orientation had a higher polarization and lower dielectric constant than films oriented with their crystallite axes perpendicular to the top film surface. Similarly, the piezoelectric coefficients in the *c*- and *a*-axis are also significantly different [Berlincourt and Jaffe, 1958].

The crystallographic orientation of ferroelectric films can be influenced by numbers of factors: the growth technique, the selection of bottom electrode material and its orientation. Several workers have reported on fabrication of oriented ferroelectric films. It was reported that BaTiO<sub>3</sub> growth on (001) MgO by metal-organic chemical-vapor deposition (MOCVD) leads to *a*-axis-oriented films whereas *c*-axis-oriented films have been grown on (001) MgO by pulsed laser deposition (PLD). Gifford and Kingon [Gifford and Kingon, 1992] deposited (100) oriented PZT 40/60 films by ion beam deposition on platinized MgO whereas Kushida and Takeuchi [Kushida and Takeuchi, 1987] found that the PbTiO<sub>3</sub> film grown on a (100) SrTiO<sub>3</sub> single-crystal plate was highly *c*-axis oriented from the x-ray diffraction observation.



From the above examples, the films grown by different materials are anisotropic. Anisotropy influences ferroelectric properties of the films. It is well known that  $\text{PbTiO}_3$  has a large spontaneous polarization and a high electromechanical coupling constant in the  $c$ -axis direction. For instance, Kushida and Takeuchi [Kushida and Takeuchi, 1987] have demonstrated the existence of a large electromechanical coupling constant in (100)-oriented  $\text{PbTiO}_3$  film. Moreover, Lian and Sottos [Lian and Sottos, 2000] have shown that lead zirconate titanate (PZT) thin films with (100) preferred orientation were found to have higher piezoelectric constants and lower dielectric dissipation factors than films with (111) preferred orientation.

In this work, the anisotropic effect is represented by the volume fraction of  $c$ -domains,  $\phi_c$ . On one hand, it gives the population of  $c$ -domains in the film. On the other, it determines whether a rotation of a dipole is energetically favorable. For example, in a  $c$ -domain dominated case, dipoles are preferentially aligned along longitudinal direction. Therefore, a dipole rotating from the longitudinal direction to the transverse one will take more energy than one undergoing reverse rotation, as shown in Figure 3.7. Consequently, the former rotation is not preferable in a  $c$ -domain-dominated case. Combined with the effects of ferroelectric strain, there must be an additional contribution in the system Hamiltonian to account for this anisotropic effect.

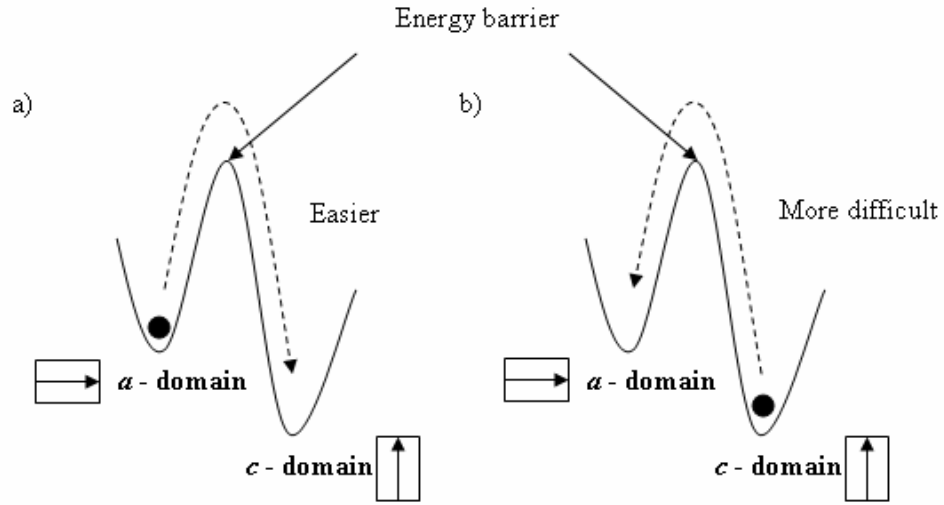


Figure 3.7 Change in energy for (a) dipole transiting from in-plane ( $\alpha$ -domain) orientation to out-of-plane ( $c$ -domain) orientation, and (b) dipole transiting from out-of-plane orientation to in-plane orientation. Case (a) is more energetically favorable in a  $c$ -domain-dominated sample.

We incorporate the term  $H'$  into the system Hamiltonian in Eqn. (3.18) to tackle the effect of anisotropy switching on the ferroelectric properties. The explicit form of  $H'$  in Eqn. (3.18) can be written as:

$$H' = -\sum_{i,j} H_3(\phi_c - \phi_a) \left| \hat{n}^T \hat{S}_{ij} \right| \quad (3.20)$$

where  $H_3$  is the energy barrier between  $a$ - and  $c$ - domains during switching, and  $\hat{n}$  the unit matrix along the longitudinal direction. Supposed that a dipole  $\hat{S}_{ij}$  is selected and rotates into another state denoted by  $\hat{S}'_{ij}$ , the change in Hamiltonian  $\Delta H'$  becomes

$$\Delta H' = H_3(\phi_c - \phi_a) \left\{ \left| \hat{n}^T \hat{S}'_{ij} \right| - \left| \hat{n}^T \hat{S}_{ij} \right| \right\}. \quad (3.21)$$

The corresponding signs of  $\Delta H'$  after switching between  $a$ -domain and  $c$ -domain under



different cases are shown in Table 3.2.

	$\hat{S}_{ij}$ initially at state A or C	$\hat{S}_{ij}$ initially at state B or D
before rotation ( $\hat{S}_{ij}$ )	$-H_3(\phi_c - \phi_a)$	0
after rotation ( $\hat{S}'_{ij}$ )	0	$-H_3(\phi_c - \phi_a)$
$\Delta H'$	$H_3(\phi_c - \phi_a)$	$-H_3(\phi_c - \phi_a)$
a) For $\phi_c > \phi_a$	$> 0$	$< 0$
b) For $\phi_c < \phi_a$	$< 0$	$> 0$

Table 3.2 The change in Hamiltonian  $\Delta H'$  for the case (a)  $c$ -domains are dominant and (b)  $a$ -domains are dominant after switching between  $a$ -domain and  $c$ -domain.

From this table, it reveals that it needs an amount of energy  $H_3(\phi_c - \phi_a)$  in order to rotate a dipole from  $c$ - to  $a$ - domain. Conversely, an energy of  $-H_3(\phi_c - \phi_a)$  is released by rotating the dipole from  $a$ - to  $c$ - domain. Consequently, the dipole aligned along  $z$  axis is more energetically favorable in a  $c$ -domain dominated sample. For  $\phi_c < \phi_a$ , dipoles parallel to the film are more stable. Hence, the signs of  $\Delta H'$  obtained from Eqn. (3.21) for both cases,  $\phi_c > \phi_a$  and  $\phi_c < \phi_a$ , can reflect the switching anisotropy.



### **3.4 Switching mechanism and algorithm**

By using the algorithm described in Section 3.1.2 to initialize the domain configuration, the whole film can be divided into domains with both  $90^\circ$  and  $180^\circ$  domain walls. The existence of  $90^\circ$  domain walls must be a consequence of  $90^\circ$  rotation of dipoles whereas the presence of  $180^\circ$  domain walls can be caused by either one  $180^\circ$  bipolar flipping or two successive  $90^\circ$  rotations. In the co-existence of both  $a$ - and  $c$ -domains as our film, it is expected that both  $90^\circ$  rotation and  $180^\circ$  flipping occur. It has been shown that, on one hand,  $90^\circ$  domain wall movement is responsible for the electromechanical responses, and on the other hand,  $180^\circ$  flipping of dipole demands more energy than  $90^\circ$  rotation [Nagarajan et al., 1999; Kim et al., 2003]. It is natural to conclude that the switching mechanism in an electromechanical system is dominated by  $90^\circ$  rotations of dipoles. In our present simulation, we consider only the contribution from  $90^\circ$  rotations and ignore the portion from  $180^\circ$  flipping for simplicity.

The polarization switching is implemented by the conventional Metropolis algorithm. It has been shown that the polarization switching through the domain wall movement takes less energy than by the rotation of a dipole inside a domain. The domain wall movement can be visualized by the change in dipole orientation for a cell at the domain wall, causing the wall moves in unit of one-cell. This cell is called a wall cell and the dipole inside is called the wall dipole. It can be shown that, there must be at least one dipole from its nearest neighbors aligned at a direction other than that of the wall cell. It will expense less energy than if the cell is inside the domain. The latter is referred to an interior cell. The corresponding dipole is called the interior dipole. In



Metropolis algorithm, a move that takes less energy will occur more probably. Thus the switching by the nucleation of a foreign domain inside a domain through the rotation of an interior dipole can still occur even though it is not energetically favorable. In our present model, we rule out all the rotations of the interior dipoles for simplicity. We define a Monte Carlo Step (MCS) as the trial of flipping one dipole at a site. In each Monte Carlo step (MCS), a pseudo-spin  $\hat{S}_{ij}$  in the film is randomly chosen and is restricted to rotate  $90^\circ$ , either along clockwise or anti-clockwise direction, with equal probabilities. Thus, the change in Hamiltonian  $\Delta H$  through a  $90^\circ$  rotation is evaluated. The trial rotation for this dipole is accepted when one of the following conditions is satisfied:

$$\Delta H < 0 \quad (3.22)$$

or

$$\exp(-\Delta H / k_B T) < r, \quad (3.23)$$

where  $r$  is a random number in the interval  $(0,1)$ ,  $T$  the temperature and  $\Delta H$  the change in Hamiltonian. This algorithm ensures that the change in system energy is either minimized or thermally activated under a finite temperature. As the pseudo-spin state is changed, the strain state must also be changed correspondingly according to Table 3.1. Both dipole and strain configurations are updated after every MCS.



### 3.5 Calculation of observable properties

The longitudinal polarization at a particular instance can be evaluated by the ensemble average of the system of dipoles, as shown by the following expression:

$$P_3 = \frac{P_s \sum_{ij} \{\hat{n}^T \hat{S}_{ij}\}}{N_x N_z}, \quad (3.24)$$

where  $\hat{n} = \begin{pmatrix} 1 \\ 0 \end{pmatrix}$  is the unit matrix along the longitudinal direction. It is more convenient to investigate the electric displacement - electric field hysteresis ( $D - E$ ) loop. The electric displacement  $D$  is related by:

$$D_3 = P_3 + \kappa E_3, \quad (3.25)$$

where  $\kappa = \kappa_o \kappa_r$ ,  $\kappa_o$  is the permittivity in free space and  $\kappa_r$  is the relative permittivity of the material.

To calculate the dielectric susceptibility, a small amplitude longitudinal  $dc$  electric field is applied to the film. The variance of polarization is then calculated by the following expression [Privman, 1990]:

$$\chi_{33} = \frac{\partial P_3}{\partial E_3} = \frac{N_x N_z}{k_B T} \left\langle P_3^2 - \langle P_3 \rangle^2 \right\rangle \quad (3.26)$$

where  $\langle \dots \rangle$  is time-average of a quantity after the steady-state condition has been attained. The time averages of a quantity, such as  $\langle P_3 \rangle$ , is the average of  $P_3$  over many MCS after attaining steady state condition.



The average longitudinal and transverse strains of each cell can be calculated from the following expressions:

$$\varepsilon_3 = \frac{1}{N_x N_z} \sum_{ij} \hat{n}^T (\hat{\varepsilon}_{ij} - \hat{\varepsilon}_{ij}^0) \quad (3.27)$$

and

$$\varepsilon_1 = \frac{1}{N_x N_z} \sum_{ij} \hat{q}^T (\hat{\varepsilon}_{ij} - \hat{\varepsilon}_{ij}^0) \quad (3.28)$$

where  $\hat{\varepsilon}_{ij}^0$  is the initial strain matrix for each cell,  $\hat{n} = \begin{pmatrix} 1 \\ 0 \end{pmatrix}$  and  $\hat{q} = \begin{pmatrix} 0 \\ 1 \end{pmatrix}$  are the unit matrices along the longitudinal and transverse direction, respectively.

The volume fraction of each spin state can be obtained as follows:

$$\begin{aligned} \phi_{S_A} &= \frac{\text{Number of dipoles at State A}}{\text{Total number of dipoles}} \\ \phi_{S_B} &= \frac{\text{Number of dipoles at State B}}{\text{Total number of dipoles}} \\ \phi_{S_C} &= \frac{\text{Number of dipoles at State C}}{\text{Total number of dipoles}} \\ \phi_{S_D} &= \frac{\text{Number of dipoles at State D}}{\text{Total number of dipoles}} \end{aligned} \quad (3.29)$$



### 3.6 Normalization of variables

In order to implement the numerical calculation, all variables should be converted into dimensionless versions. The conversion is described as follows:

$$\begin{aligned}
 h &= \frac{H}{J} & h' &= \frac{H'}{J} \\
 \hat{e} &= \frac{P_s}{J} \hat{E}, & \hat{\zeta} &= \frac{\hat{\sigma} \varepsilon_{sat}}{J}, & \alpha' &= \frac{\alpha}{J}, \\
 \hat{\zeta}_{ij} &= \frac{\hat{\varepsilon}_{ij}}{\varepsilon_{sat}}, & \hat{\zeta}_{ij}^F &= \frac{\hat{\varepsilon}_{ij}^F}{\varepsilon_{sat}},
 \end{aligned} \tag{3.30}$$

where  $J$  is the coupling coefficient in ferroelectric material in unit of  $\text{Jm}^{-3}$  and  $\varepsilon_{sat}$  is the saturated strain of the material. After the conversion, the normalized Hamiltonian now becomes

$$h = - \sum_{i,j,k,l} \hat{S}_{ij}^T \hat{S}_{kl} - \sum_{i,j} \hat{e}^T \hat{S}_{ij} - \sum_{i,j} \hat{\zeta}^T \hat{\varepsilon}_{ij} - \alpha' \sum_{i,j,k,l} \hat{\zeta}_{ij}^F \hat{\varepsilon}_{kl}^F + h' \tag{3.31}$$

The normalized strain  $\hat{\varepsilon}_{ij}$  in Eqn. (3.30) can then be expressed as

$$\hat{\varepsilon}_{ij} = \hat{\zeta}_{ij}^F + \hat{\zeta}_{ij}^{el} + \hat{\zeta}_{ij}^E \tag{3.32}$$

where

$$\hat{\zeta}_{ij}^F = \frac{\hat{\varepsilon}_{ij}^F}{\varepsilon_{sat}}, \quad \hat{\zeta}_{ij}^{el} = \frac{\hat{\varepsilon}_{ij}^{el}}{\varepsilon_{sat}} \quad \text{and} \quad \hat{\zeta}_{ij}^E = \frac{\hat{\varepsilon}_{ij}^E}{\varepsilon_{sat}}. \tag{3.33}$$



The elastic strain in Eqns. (3.11) and (3.12) become:

$$\hat{\xi}_{ij}^{el} = \begin{pmatrix} \xi_3^{el} \\ \xi_1^{el} \end{pmatrix} = \frac{1}{Y'} \begin{pmatrix} 1 & -\nu \\ -\nu & 1 \end{pmatrix} \begin{pmatrix} \zeta_3 \\ \zeta_1 \end{pmatrix} \quad \text{if } \zeta_3 < \zeta_{crit} \quad (3.34)$$

and

$$\begin{aligned} \xi_3^{el} &= \frac{\zeta_{crit}}{Y'} + k \left( \zeta_3 - \zeta_{crit} \right)^n - \nu \frac{\zeta_1}{Y'} \\ \xi_1^{el} &= \frac{\zeta_1}{Y'} - \nu \left[ \frac{\zeta_{crit}}{Y'} + k \left( \zeta_3 - \zeta_{crit} \right)^n \right] \end{aligned} \quad \text{if } \zeta_3 > \zeta_{crit} \quad (3.35)$$

where  $Y' = Y \frac{\varepsilon_{sat}^2}{J}$  is the normalized Young's modulus,  $\nu$  is the Poisson ratio and  $\zeta_{crit}$  is the critical value of the normalized stress that the linear relation between stress and strain change to the non-linear one.  $\zeta_3$  and  $\zeta_1$  are, respectively, the longitudinal and transverse stress components. For the field-induced strain, it can be normalized as follow:

$$\begin{aligned} \left( \xi_3^E \right)_{ij} &= \frac{\varepsilon_3^E}{\varepsilon_{sat}} = d_{33} \frac{e_3 J}{\varepsilon_{sat} P_S} = d'_{33} e_3 \quad \text{and} \\ \left( \xi_1^E \right)_{ij} &= \frac{\varepsilon_1^E}{\varepsilon_{sat}} = d_{13} \frac{e_3 J}{\varepsilon_{sat} P_S} = d'_{13} e_3 \end{aligned} \quad (3.36)$$

where  $d'_{33} = \frac{d_{33} J}{\varepsilon_{sat} P_S}$  and  $d'_{13} = \frac{d_{13} J}{\varepsilon_{sat} P_S}$ . In Eqn. (3.36), the electrostrictive effect is ignored. Furthermore, the term  $h'$  for tackling the anisotropic effect is written as:

$$h' = - \sum_{i,j} h_3 (\phi_c - \phi_a) \left| \hat{n}^T \hat{S}_{ij} \right| \quad (3.37)$$

where  $h_3 = \frac{H_3}{J}$ .



Besides the system Hamiltonian, other parameters should also be normalized in the calculation. The temperature  $T$  in Eqn. (3.23) is normalized to a dimensionless variable  $\bar{T}$  as follows:

$$\bar{T} = \frac{k_B T}{J v_c} \quad (3.38)$$

where  $v_c$  is the volume of a single tetragonal cell, i.e.,  $a_0^2 c_0$ . Moreover, both the period ( $\Gamma$ ) and time ( $t$ ) are scaled in terms of number of Monte Carlo steps (MCS) according to the following relations

$$\Gamma_{\text{MCS}} = \Gamma \frac{N_x N_z}{\Delta t}, \quad (3.39)$$

and

$$t_{\text{MCS}} = t \frac{N_x N_z}{\Delta t}, \quad (3.40)$$

where  $\Delta t$  is the infinitesimal time step. The purpose of the scaling in Eqns. (3.39) and (3.40) is to ensure that the computed results are not affected by selection of time step [Liu et al., 2000; Li, K. T. and Lo, 2004].

The longitudinal polarization  $P_3$  in Eqn. (3.24) is normalized by  $P_S$ , which is expressed as:

$$p_3 = \frac{P_3}{P_S} = \frac{\sum_{ij} \hat{n}^T \hat{S}_{ij}}{N_x N_z} \quad (3.41)$$

so that the maximum polarization is equal to 1. The normalized electric displacement along the electric field direction  $d_3$  is given by:

$$d_3 = \frac{D_3}{P_S} = p_3 + \frac{\kappa}{P_S} E_3 = p_3 + \frac{\kappa J}{P_S^2} e_3 = p_3 + \kappa' e_3 \quad (3.42)$$



where  $\kappa' = \frac{\kappa_o J}{P_s^2}$ . Moreover, the normalized susceptibility  $\bar{\chi}_{33}$  can be expressed as:

$$\bar{\chi}_{33} = \frac{\chi_{33}}{\chi'} = \frac{1}{\bar{T}} \langle p_3^2 - \langle p_3 \rangle^2 \rangle \quad (3.43)$$

where  $\chi' = \frac{N_x N_z P_s^2}{J V_c}$ . For the mechanical properties, such as the longitudinal and

transverse strains of each cell, can be normalized as:

$$\xi_3 = \frac{1}{N_x N_z} \sum_{ij} \hat{n}^T (\hat{\xi}_{ij} - \hat{\xi}_{ij}^0) \quad (3.44)$$

and

$$\xi_1 = \frac{1}{N_x N_z} \sum_{ij} \hat{q}^T (\hat{\xi}_{ij} - \hat{\xi}_{ij}^0) \quad (3.45)$$

where  $\hat{\xi}_{ij}^0$  is the initial strain matrix for each cell. In next chapter, we will present the calculated results obtained from our model.



## Chapter 4 Simulation results

### 4.1 *Effect of static stress on phase transition temperature*

#### 4.1.1 Experimental observations

From X-ray diffraction measurements, the presence of misfit strain in the ferroelectric films has been identified by the changes in lattice constants of the distorted cells. Moreover, the in-plane compressive stress in ferroelectric films led to an increase in the Curie temperature  $T_c$  [Kushida and Takeuchi, 1990; Kushida and Takeuchi, 1991; Rossetti et al., 1991; Taylor et al., 2002; Yuzyuk et al., 2002] whereas the in-plane tensile stress resulted in a reduction. For instance, the cubic-to-tetragonal phase transition of  $\text{PbTiO}_3$  thin films under a transverse compressive stress occurred at a temperature nearly  $50^\circ\text{C}$  higher than that measured from a bulk single crystal ( $T_c \approx 490^\circ\text{C}$ ) [Kushida and Takeuchi, 1990; Kushida and Takeuchi, 1991]. On the other hand, Taylor et al. [Taylor et al., 2002] have reported a decrease in  $T_c$  under a large tensile strain in the film induced by thermal mismatch. In section 4.1.3, we will demonstrate the shift in phase transition in the presence of a transverse stress by using the modified four-state Potts model and compared with the experimental results qualitatively.



#### 4.1.2 Determination of phase transition temperature

The critical behavior of a ferroelectric material can be determined from both the polarization-temperature ( $P_3 - T$ ) and susceptibility-temperature ( $\chi_{33} - T$ ) curves where  $P_3$  and  $\chi_{33}$  are longitudinal polarization and susceptibility as defined in Chapter 3. In perovskite-type ferroelectrics, the ferroelectric phase is signified by the presence of spontaneous polarization below the Curie temperature ( $T_c$ ). The overall polarization drops to zero at or above  $T_c$ . On the other hand, the  $\chi_{33} - T$  curve diverges at  $T_c$  in an infinite system whereas the susceptibility peak becomes smeared in a finite system according to the finite size scaling theory [Privman, 1990]. Therefore, the phase transition temperature  $T_c$  can be determined by locating the critical points, i.e., the point that the overall polarization drops drastically to zero and the position of the susceptibility peak in the  $P_3 - T$  and  $\chi_{33} - T$  curves, respectively.

For a finite system at some finite temperature, there is always a nonzero probability that the system may pass from a state near  $+|P|$  to a state near  $-|P|$  or vice versa and the overall polarization at zero field vanishes [Heermann and Binder, 2002]. Therefore, a longitudinal *dc* electric field is applied to impose a preferential direction for the dipoles.



In order to obtain the  $P_3 - T$  and  $\chi_{33} - T$  curves, the system is subject to a small longitudinal  $dc$  electric field at a constant temperature  $T$ . At thermal equilibrium, the ensemble of dipoles (or pseudospins) proceeds by using the Metropolis algorithm as mentioned in Chapter 3. Considering the conditions of small electric field and small external stress, only the ferroelectric strain  $\hat{\epsilon}^F$  is important in this study. Thus, the Hamiltonian in Eqn. (3.18) can be reduced to the following form:

$$H = - \sum_{i,j,k,l} J \{ \hat{S}_{ij}^T \hat{S}_{kl} \} - P_S \sum_{i,j} \{ \hat{E}^T \hat{S}_{ij} \} - \sum_{ij} \{ \hat{\sigma}^T \hat{\epsilon}_{i,j}^F \} - \alpha \sum_{i,j,k,l} \hat{\epsilon}_{i,j}^{F^T} \hat{\epsilon}_{k,l}^F + H' \quad (4.1)$$

where  $\hat{\epsilon}_{k,l}^F$  is defined in Eqn. (3.10). It can be shown that the elastic strain only makes a slight modification of our results without altering the trends. Moreover, if we take  $\phi_c = \phi_a = 0.5$ , i.e. the  $c$ -domain volume fraction is equal to that of  $a$ -domains. The anisotropy effect in dipole switching can be ignored,  $H' = 0$ .

When an initially unpoled system is subject to a positive  $dc$  field, dipoles inside the film rotate sequentially in response to the driving field. The overall polarization gradually increases until it finally attains a steady state value where  $\Delta p_3 / \langle p_3 \rangle < 0.05$  as shown in Figure 4.1. The number of MCS to achieve the steady value depends on the magnitude of the  $dc$  field as well as the system size. It increases with increasing thickness  $N_z$  [Li, K.T., 2005] and decreases with the magnitude of the  $dc$  field. Therefore, it requires millions of MCSs to reach the steady state when the electric field is getting smaller. In our simulation, the steady state condition can be achieved after iterating 10000 Monte Carlo steps (MCSs) per dipole.

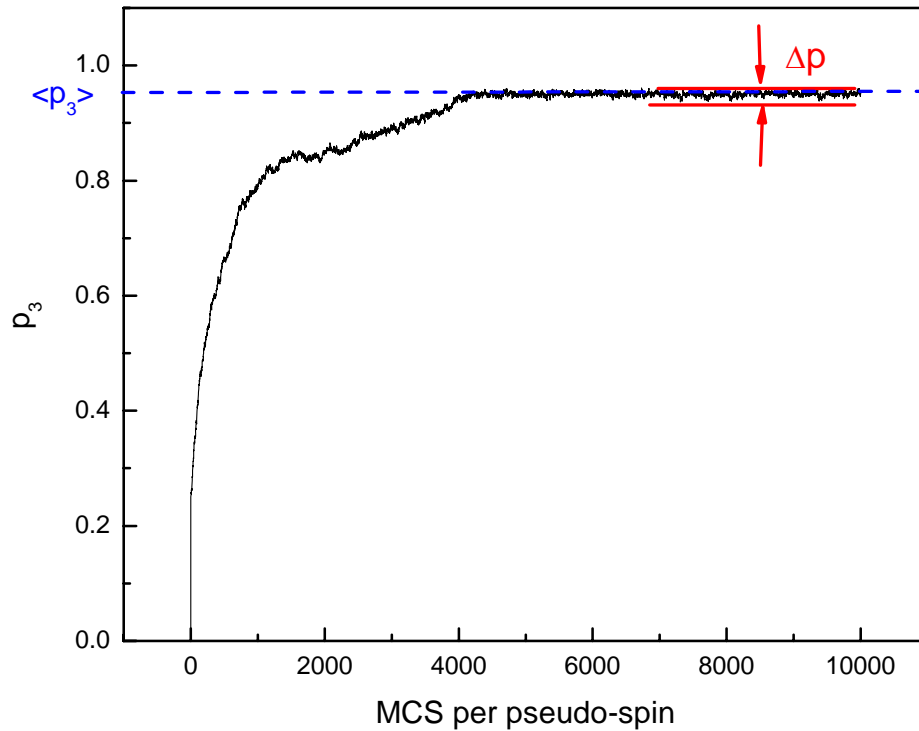


Figure 4.1 Polarization vs MCS per pseudo-spin at  $e_3 = 0.02$  and  $\bar{T} = 0.9$ .

The longitudinal polarization ( $P_3$ ) at a particular instance can be evaluated by Eqn. (3.24). The time average of polarization, denoted by  $\langle P_3 \rangle$ , is the average of  $P_3$  over many MCSs after attaining a steady-state condition. We are also able to evaluate the susceptibility from the variance of polarization by Eqn. (3.26). Different  $\langle P_3 \rangle$  and  $\chi_{33}$  values can then be calculated in different temperatures. The relations of longitudinal polarization and susceptibility versus temperature can be obtained.



### 4.1.3 Results and discussion

In our simulation, the size of the system is  $N_x = 150$  and  $N_z = 80$ . We have used the dimensionless equations and hence variables as described in Section 3.6 for our simulation. The  $p_3 - \bar{T}$  and  $\bar{\chi}_{33} - \bar{T}$  curves under different loading conditions were evaluated using the following parameters:  $e_3 = 0.02$ ,  $\zeta_0 = 0.5$ ,  $\alpha' = 0.0$  and  $\phi_c = 0.5$ .

At each temperature, the system undergoes 10000 Monte Carlo steps (MCSs) per dipole. The effects of transverse stress on both the polarization and susceptibility are shown in Figures 4.2 and 4.3, respectively. The corresponding effects induced by longitudinal stress are shown in Figures 4.4 and 4.5.

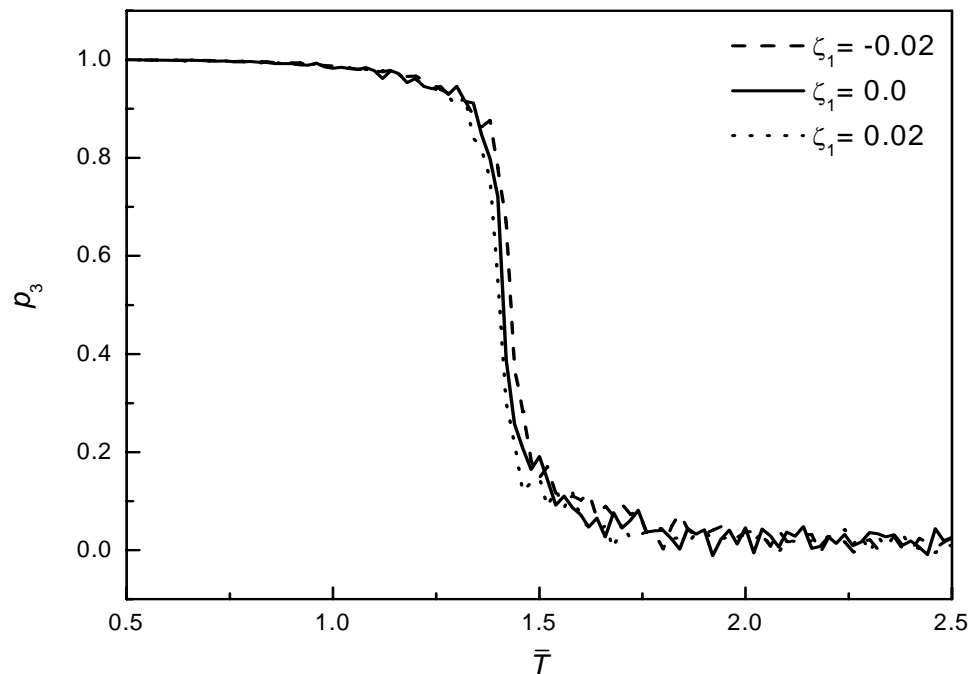


Figure 4.2 Polarization vs temperature for different values of transverse stress ( $\zeta_1 = 0.0, -0.02$  and  $+0.02$ ).

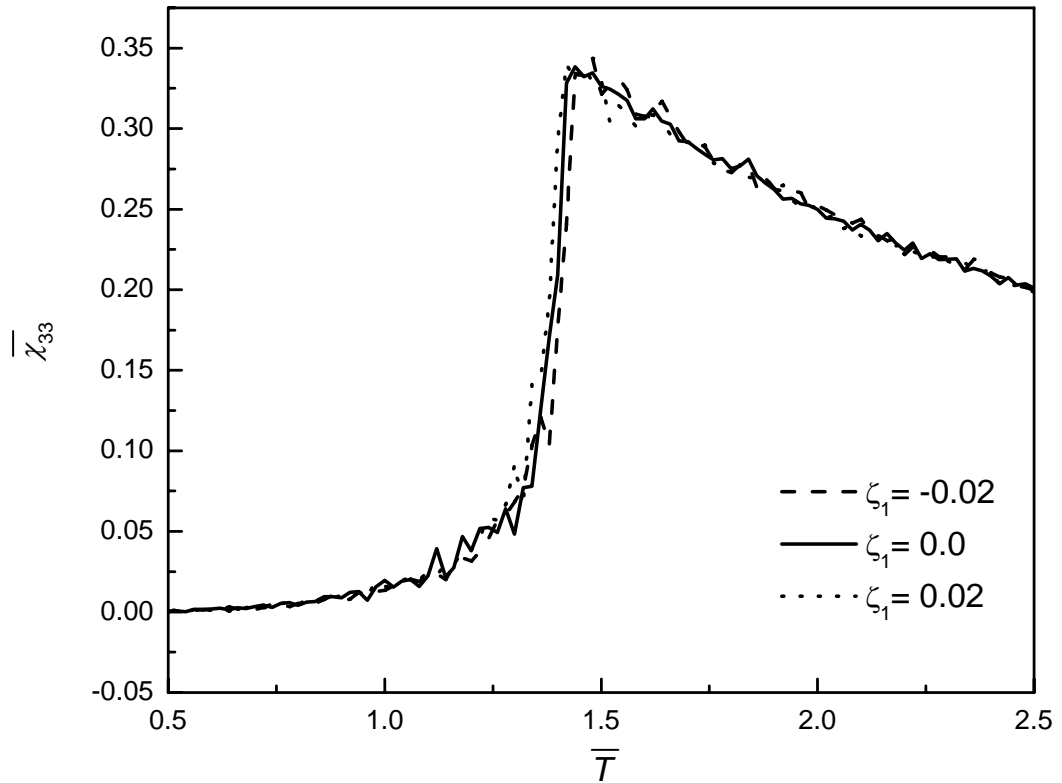


Figure 4.3 Susceptibility vs temperature for different values of transverse stress ( $\zeta_1 = 0.0, -0.02$  and  $+0.02$ ).

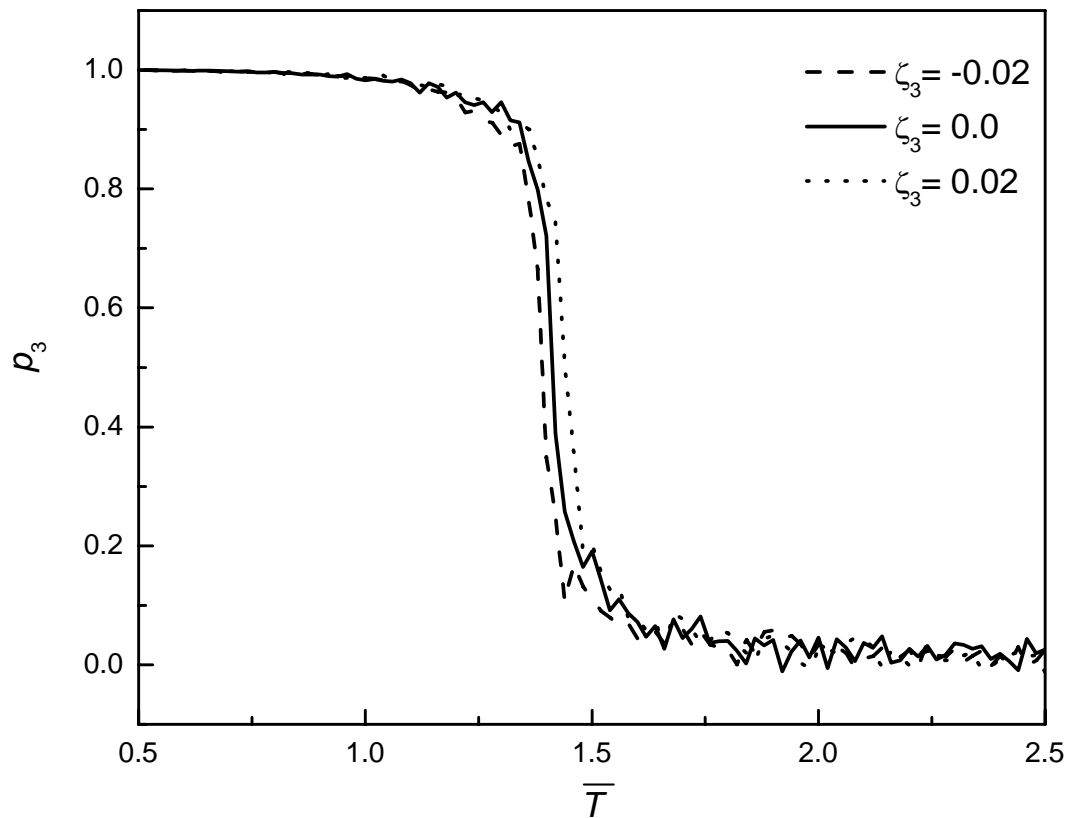


Figure 4.4 Polarization vs temperature for different values of longitudinal stress ( $\zeta_3 = 0.0, -0.02$  and  $+0.02$ ).

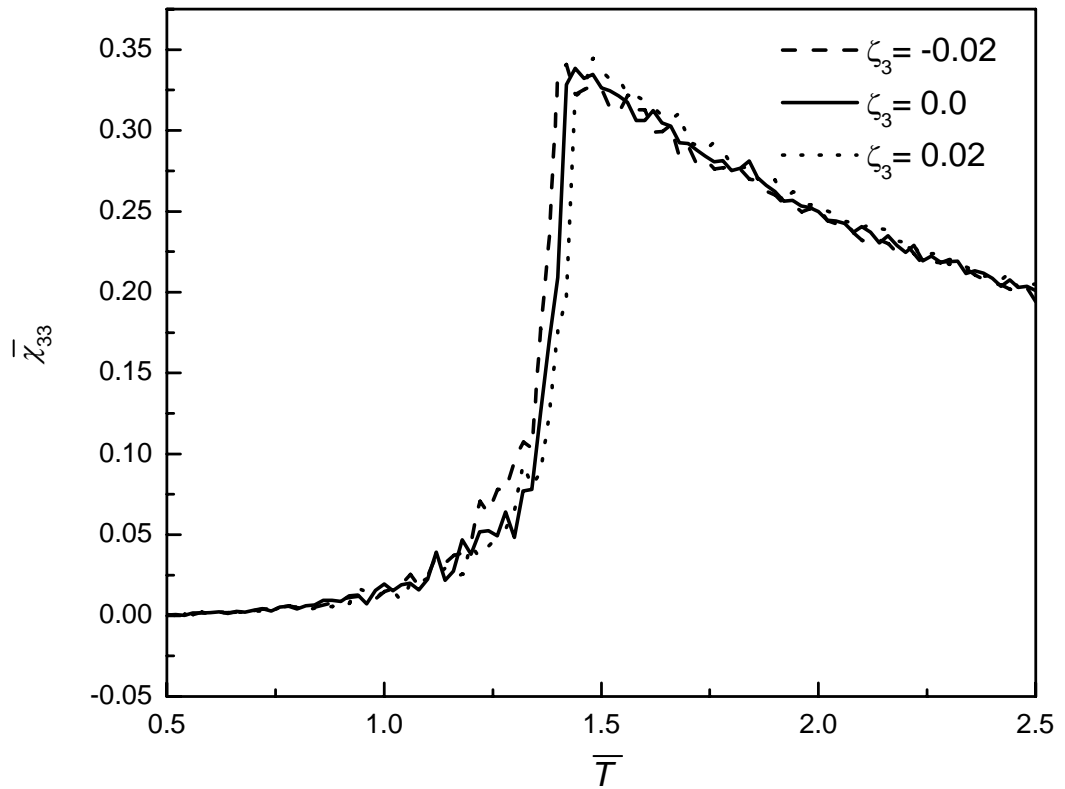


Figure 4.5 Susceptibility vs temperature for different values of longitudinal stress ( $\zeta_3 = 0.0, -0.02$  and  $+0.02$ ).



The critical behavior of the system can be determined from both  $p_3 - \bar{T}$  and  $\bar{\chi}_{33} - \bar{T}$  curves. In Figures 4.2 and 4.4,  $p_3$  drops gradually at about  $\bar{T}_c = 1.3$  with a non zero tailing above  $\bar{T}_c$ . This non vanishing  $p_3$  value above  $\bar{T}_c$  is due to the finite size effect. Thus, it is difficult to locate the Curie temperature precisely in the  $p_3 - \bar{T}$  curves. All we can know from the  $p_3 - \bar{T}$  curves is that  $\bar{T}_c$  varies within the range of 1.3-1.6. We can estimate the phase transition temperature by extrapolating the sudden drop of the  $p_3 - \bar{T}$  curves to  $p_3 = 0$  and taking the mean value of the x value.

With the  $\bar{\chi}_{33} - \bar{T}$  curve, the Curie temperature  $\bar{T}_c$  can be determined by locating peak position in a more accurate manner. In Figure 4.3, the peak position is at 1.48, 1.44 and 1.42 when  $\zeta_1 = -0.02, 0.0$  and  $0.02$ , respectively. However, in the case of longitudinal stress, the peak position is at 1.42, 1.44 and 1.48 when  $\zeta_3 = -0.02, 0.0$  and  $0.02$ , respectively. The susceptibility peaks from both Figures 4.3 and 4.5 are rounded and finite, unlike an infinite phase transition peak from an infinite system [Privman, 1990]. In addition to the infinite system size, Eqn. (3.26) is applicable to the case when the electric field tends to zero [Heermann and Binder, 2002]. A sharper phase transition and a more accurate  $\bar{T}_c$  can be obtained when the amplitude of the electric field is very small and the system size is infinite [Slivka et al., 2005]. However, when we use a much smaller electric field, i.e.,  $e_3 < 0.02$ , the electric field cannot impose a preferential direction for the dipoles. The system with finite size may



still transit from a state near  $+|P|$  to a state near  $-|P|$  or via versa after several hundreds of MCSs [Heermann and Binder, 2002]. The overall polarization fluctuates rapidly even below  $\bar{T}_c$  which induces unexpected peaks in susceptibility-temperature curves. We cannot determine the phase transition from the  $\bar{\chi}_{33} - \bar{T}$  curves. On the other hand, a large electric field will lead to the smearing of the susceptibility-temperature curve and the shift of peak at higher temperature [Slivka et al., 2005]. Thus, we have chosen  $e_3 = 0.02$  as the amplitude of the electric field which is small enough to maintain an abrupt drop in polarization at  $\bar{T}_c$ , but can still impose a preferential direction for the dipoles.

The phase transition temperatures obtained from our model are smaller than the theoretical value  $\bar{T}_c = 2.269$  obtained from a two-dimensional Ising model [Privman, 1990]. The number of states that a dipole can switch is a measure of the degree of freedom imposed on the dipole switching. For instance, the degree of freedom in a four-state Potts model is larger than that in Ising model. Consequently, we can conclude that the larger the degree of freedom the smaller phase transition temperature is obtained which is consistent with Ono's result [Ono, 1984], after his investigation on r-state, ferro- and antiferromagnetic systems using Bethe approximation.



From both Figures 4.2 and 4.3, the shifting direction of  $\bar{T}_c$  and the sign of the transverse stress are correlated. In particular,  $\bar{T}_c$  decreases in the presence of in-plane tensile stress. The 2D clamping exists along the film plane in the presence of in-plane tensile stress. It prohibits the dipoles to be switched towards the longitudinal direction but it favors transverse alignment. As a result,  $\bar{T}_c$  shifts downwards with the increase in the in-plane tensile stress. Conversely, the opposite trend also holds under the in-plane compressive stress. The presence of in-plane compressive stress discourages the dipoles to be aligned parallel to the film but encourages longitudinal alignment. This leads to the increase in the tetragonality along the  $z$ -direction and stabilizes the ferroelectric phase at higher temperatures. This result qualitatively agrees with experiments [Abe and Komatsu, 1995; Taylor et al., 2002; Yuzyuk et al., 2002].

The magnitude and sign of the in-plane stress can be manipulated by the selection of the film/substrate combination and the growth conditions [Abe and Komatsu, 1995; Pertsev et al., 1999; Taylor et al., 2002; Yuzyuk et al., 2002], where the biaxial in-plane stress can be induced by the following routes: (i) thermal mismatch, (ii) lattice mismatch and (iii) structural change due to the phase transition. In reality, the stress is position-dependent and decays from the interface between the substrate and film to the surface. The uniform stress can be replaced by an exponential stress function along thickness direction [Wang, X.S., 2002]. Since we assume the system is an infinitesimally thin film, the stress is supposed to uniform in the whole thin film.



Practically, the presence of transverse (or in-plane) stress can be easily realized by the selection of the film/substrate combination or by bending the film. On the other hand, few reports in the literature have mentioned the effects of uniaxial (or longitudinal) stress on  $\bar{T}_c$ . The major reason might be due to the difficulty in imposing a longitudinal stress in a controllable manner. Our model is not restricted to transverse stress. It can also be extended to the case of longitudinal stress as shown in Figures 4.4 and 4.5.

The longitudinal polarization  $p_3$  and the susceptibility  $\bar{\chi}_{33}$  against temperature  $\bar{T}$  under longitudinal stress were evaluated using the following parameters:  $e_3 = 0.02$ ,  $\xi_0 = 0.5$  and  $\phi_c = 0.5$ . It is expected that the longitudinal stress will have an effect opposite to that of the transverse stress. When the ferroelectric film is subject to a longitudinal tensile stress, the out-of-plane expansion occurs and forces the dipoles to be aligned along the  $z$ -direction. Similar to the effect of in-plane compressive stress, the longitudinal tensile stress leads to the increase in the tetragonality along the  $z$ -direction and stabilizes the ferroelectric phase at higher temperature. Thus, a higher  $\bar{T}_c$  is obtained compared with the stress free condition. Conversely, alignments of dipoles along the film can be induced by the application of a uniaxial compressive stress.  $\bar{T}_c$  shifts to a lower temperature. The shifting direction of  $\bar{T}_c$  under longitudinal stress is opposite to that under transverse stress.



We have also evaluated the longitudinal polarization  $p_3$  and the susceptibility  $\bar{\chi}_{33}$  against temperature using the same set of parameters except the different coupling coefficients of strain  $\alpha'$ , ( $\alpha' = 0.0, 0.1, 0.3$ ) as shown in Figure 4.6. There is only negligible effect of strain-strain coupling on the phase transition. Basically, neglecting the strain-strain coupling term does not alter the shifting trend of the phase transition temperature induced by the stress. Comparing with the case  $\alpha' = 0.1$  and  $\alpha' = 0.3$ , both  $p_3 - \bar{T}$  and  $\bar{\chi}_{33} - \bar{T}$  curves shift entirely towards a higher temperature as  $\alpha'$  increases. The application of strain-strain coupling term can eliminate the perturbation of the system at low temperature and it is faster to obtain a steady state. However, if the coupling coefficient is set to be a very high value, the effect of strain-strain coupling is dominant other effects which are important to ferroelectric materials.

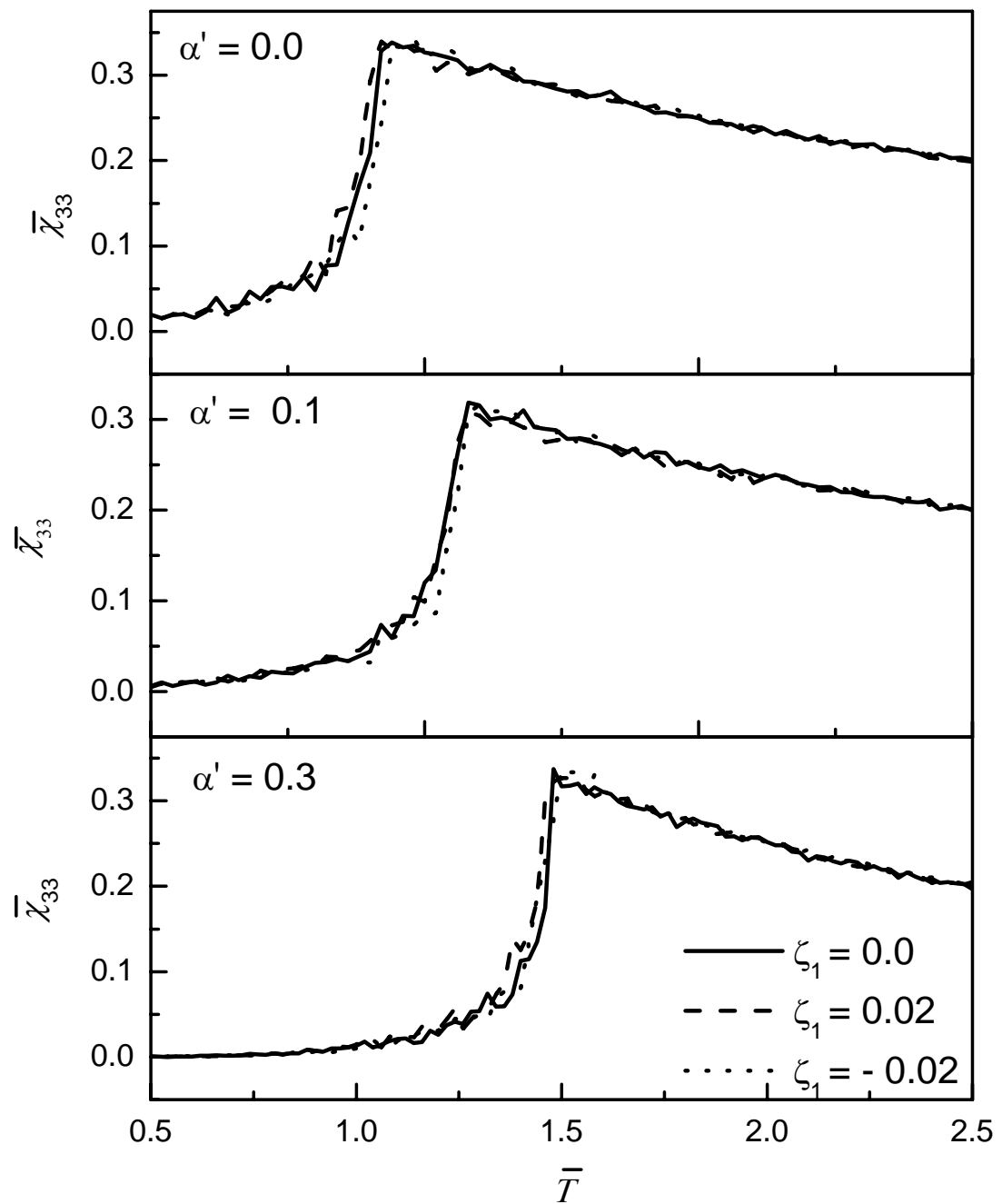


Figure 4.6 Susceptibility vs temperature for different strain-strain coupling coefficients ( $\alpha' = 0.0, 0.1$  and  $0.3$ ).



## 4.2 Effect of static stress on other ferroelectric properties

### 4.2.1 Experimental observations

The presence of in-plane stress can be easily manipulated by the selection of film/substrate combination, or bending the film in either concave or convex forms. Moreover, the uniaxial compressive stress on the sample can also be applied by a testing machine such as INSTRON. In the last Section, we have discussed the effect of stress on the phase transition temperature. We now extend the discussion to other electromechanical properties, such as the strain and the polarization under cyclic electric field. From Section 2.11(b), experimental results reveal that the presence of residual in-plane tensile stress in ferroelectric films reduces the remnant and saturated polarizations while the compressive stress increases them [Garino and Harrington, 1992; Shepard et al., 1996]. Similar effect on the area of the  $P$ - $E$  hysteresis loop has also been studied. In this section, we will study the polarization-electric field ( $P_3 - E_3$ ) loops and butterfly loops for both transverse ( $\varepsilon_1$ ) and longitudinal strains ( $\varepsilon_3$ ) against electric field ( $E_3$ ) under different stress and anisotropy conditions are simulated. Results are compared with the experiments.



### 4.2.2 Simulation

To simulate the hysteresis ( $P_3$  versus  $E_3$ ) and butterfly ( $\varepsilon_3$  and  $\varepsilon_1$  versus  $E_3$ ) loops, an external longitudinal alternating electric field is applied to the system. In the absence of local field, the electric field matrix can be expressed as follow:

$$\hat{E} = \begin{pmatrix} E_0 \sin\left(\frac{2\pi t}{\Gamma}\right) \\ 0 \end{pmatrix} \quad (4.2)$$

where  $E_0$  and  $\Gamma$  are the amplitude and period of the electric field, respectively, and  $t$  is time. Both  $\Gamma$  and  $t$  are scaled in terms of MCS by a time scale according to the following relations:

$$\Gamma_{\text{MCS}} = \Gamma \frac{N_x N_z}{\Delta t} \quad (4.3)$$

and

$$t_{\text{MCS}} = t \frac{N_x N_z}{\Delta t} \quad (4.4)$$

where  $\Delta t$  is the infinitesimally small time step. Eqn. (4.2) can then be expressed in normalized form as follow:

$$\hat{e} = \begin{pmatrix} e_0 \sin\left(\frac{2\pi t_{\text{MCS}}}{\Gamma_{\text{MCS}}}\right) \\ 0 \end{pmatrix} \quad (4.5)$$



Assuming that the film thickness is very small, we can ignore the stress gradient along the thickness direction. The stress is therefore assumed to be uniform along the thickness direction. Furthermore, we ignore the shearing stress components  $\sigma_{31} = \sigma_{13} = \sigma_5 = 0$ .

The normalized values of the observable properties, such as longitudinal polarization, electric displacement, longitudinal and transverse strains at particular instance can be evaluated by Eqns. (3.41), (3.42), (3.44) and (3.45), respectively. The  $p_3 - e_3$ ,  $d_3 - e_3$ ,  $\xi_3 - e_3$  and  $\xi_1 - e_3$  loops and the volume fractions for the four different spin states under different static stresses were stimulated.



### 4.2.3 Results and discussion

The polarization ( $p_3$ ) and electric displacement ( $d_3$ ) versus electric field hysteresis loops, and the butterfly loops for both longitudinal ( $\xi_3$ ) and transverse strains ( $\xi_1$ ) against electric field have been numerically simulated under different static stresses and different switching anisotropy parameter  $\phi_c$ . In our calculation, we have used the following parameters:  $\Gamma_{MCS} = 350$  (MCS/dipole),  $e_3 = 1.2$ ,  $\bar{T} = 0.8$ ,  $\xi_0 = 0.5$ ,  $h_3 = 0.3$ ,  $Y' = 1.5$ ,  $\nu = 0.3$ ,  $\zeta_{crit} = 0.3$ ,  $k = 0.1$ ,  $n = 0.5$ ,  $\alpha' = 0.1$ ,  $d'_{33} = 0.2$ ,  $d'_{31} = -0.1$ ,  $\kappa' = 0.5$ ,  $N_x = 150$ , and  $N_z = 80$ .

The  $p_3 - e_3$ ,  $d_3 - e_3$ ,  $\xi_3 - e_3$  and  $\xi_1 - e_3$  loops under different transverse stress values ( $\zeta_1 = 0.0, 0.5, -0.5$ ) are shown in Figures 4.7, 4.8 and 4.9, respectively. The corresponding change in volume fractions of each state are shown in Figures 4.10 and 4.11, respectively. The switching anisotropy parameter  $\phi_c$  is 0.45.

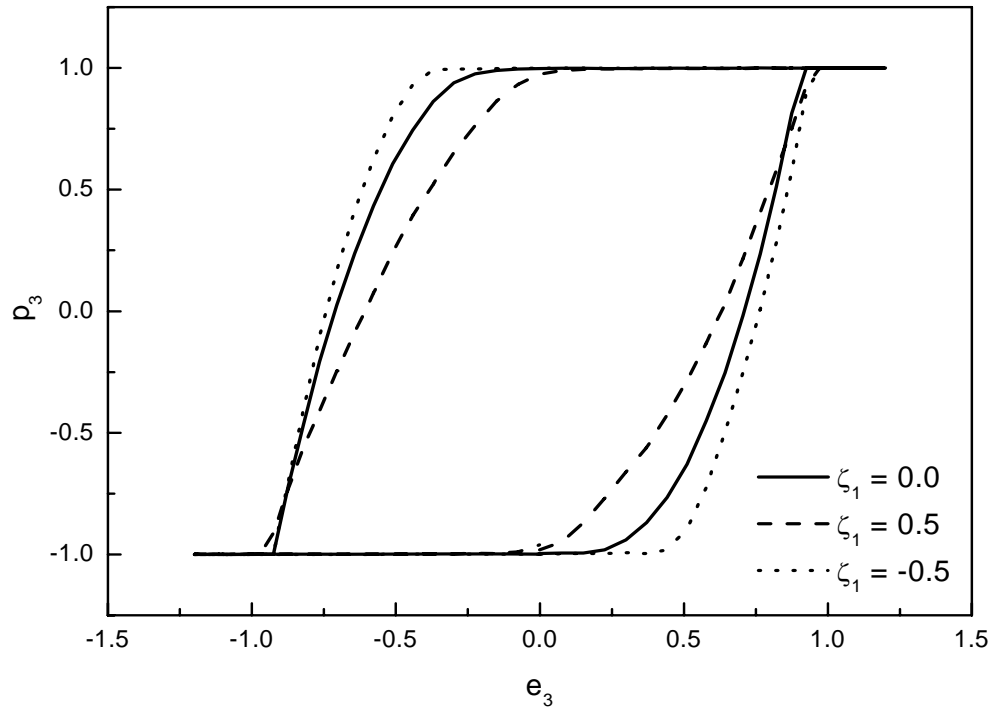


Figure 4.7 Polarization versus electric field under different static transverse stresses ( $\zeta_1 = 0.0, 0.5, -0.5$ )

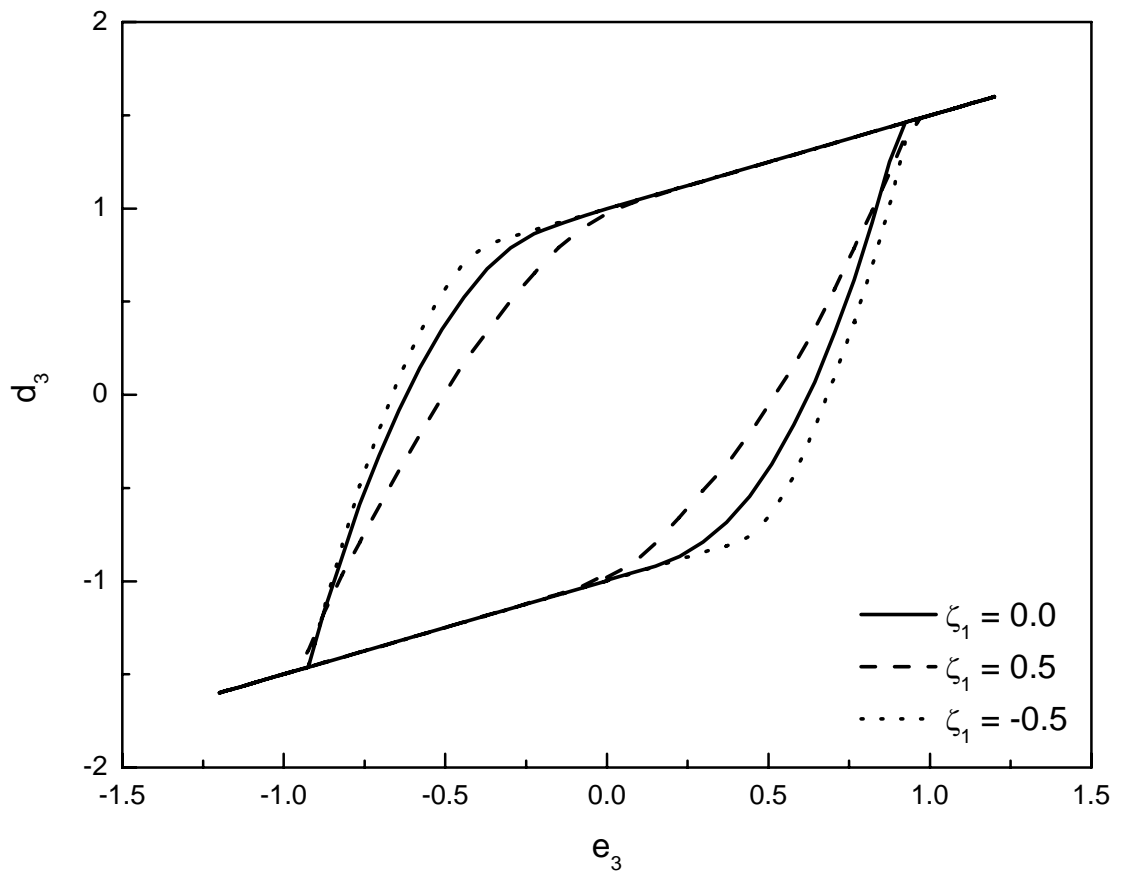


Figure 4.8 Electric displacement versus electric field under static transverse stresses ( $\zeta_1 = 0.0, 0.5, -0.5$ )

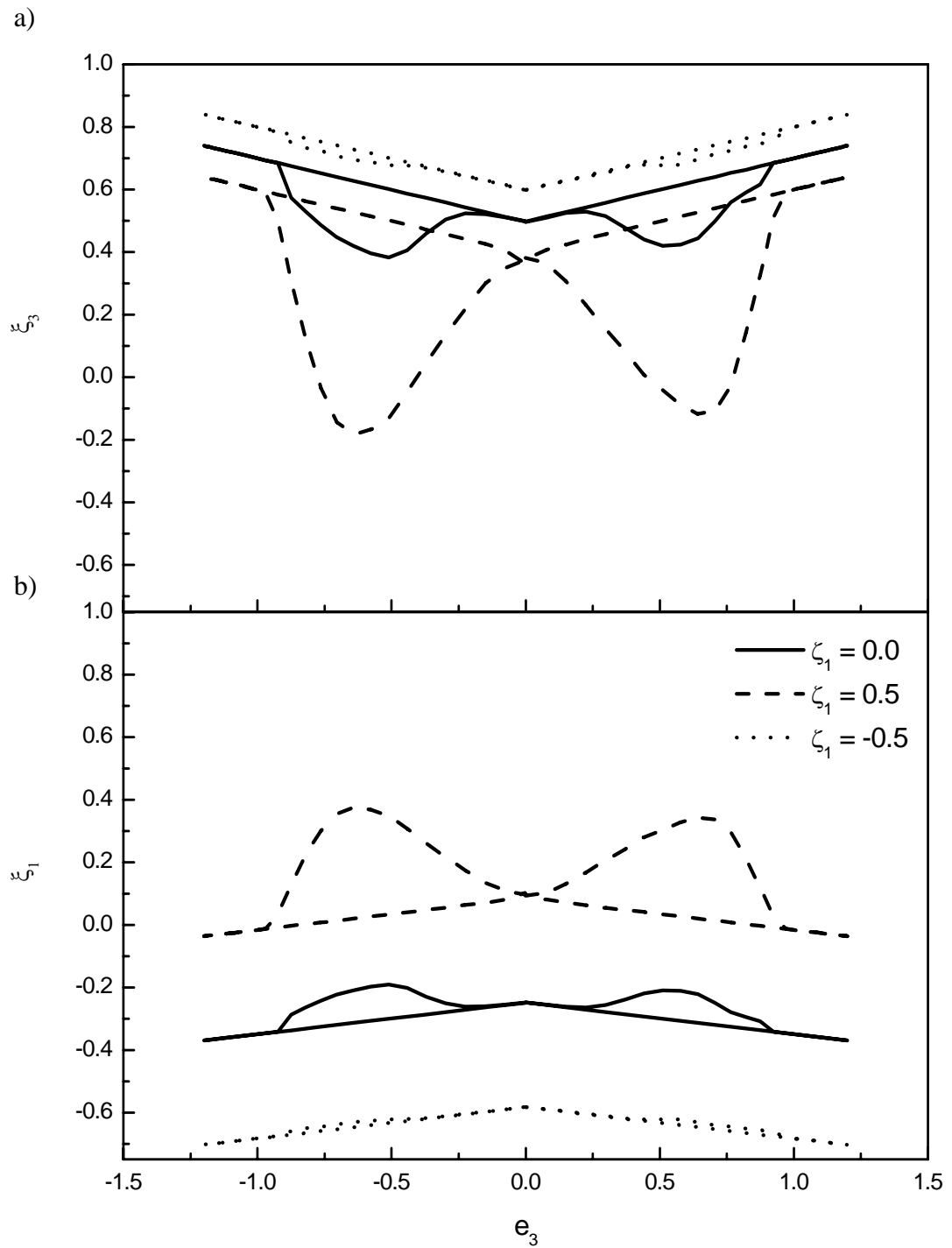


Figure 4.9 (a) Longitudinal strain and (b) transverse strain versus electric field under static transverse stresses ( $\zeta_1 = 0.0, 0.5, -0.5$ )

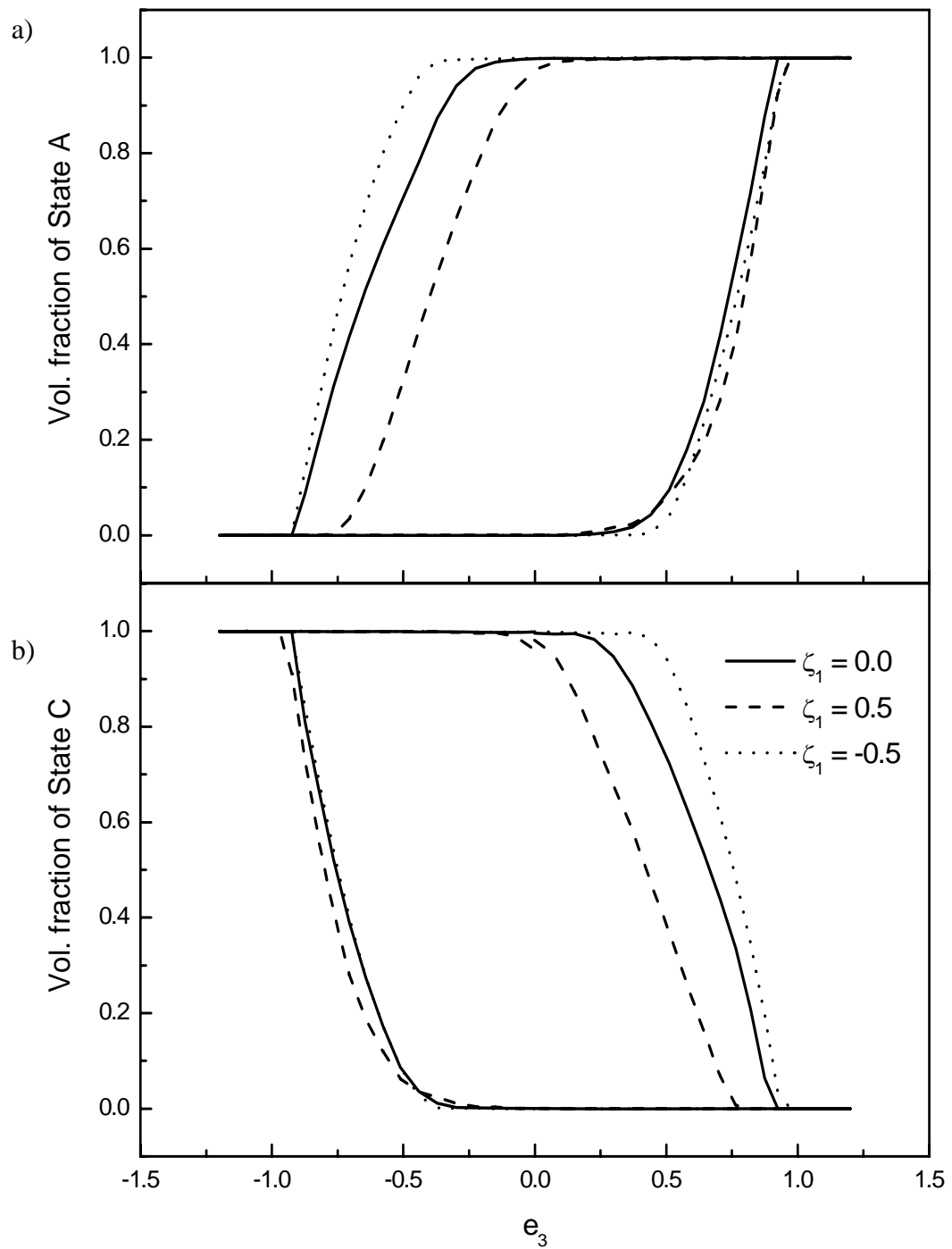


Figure 4.10 Volume fractions of (a) State A and (b) State C versus electric field under different static transverse stresses ( $\zeta_1 = 0.0, 0.5, -0.5$ )

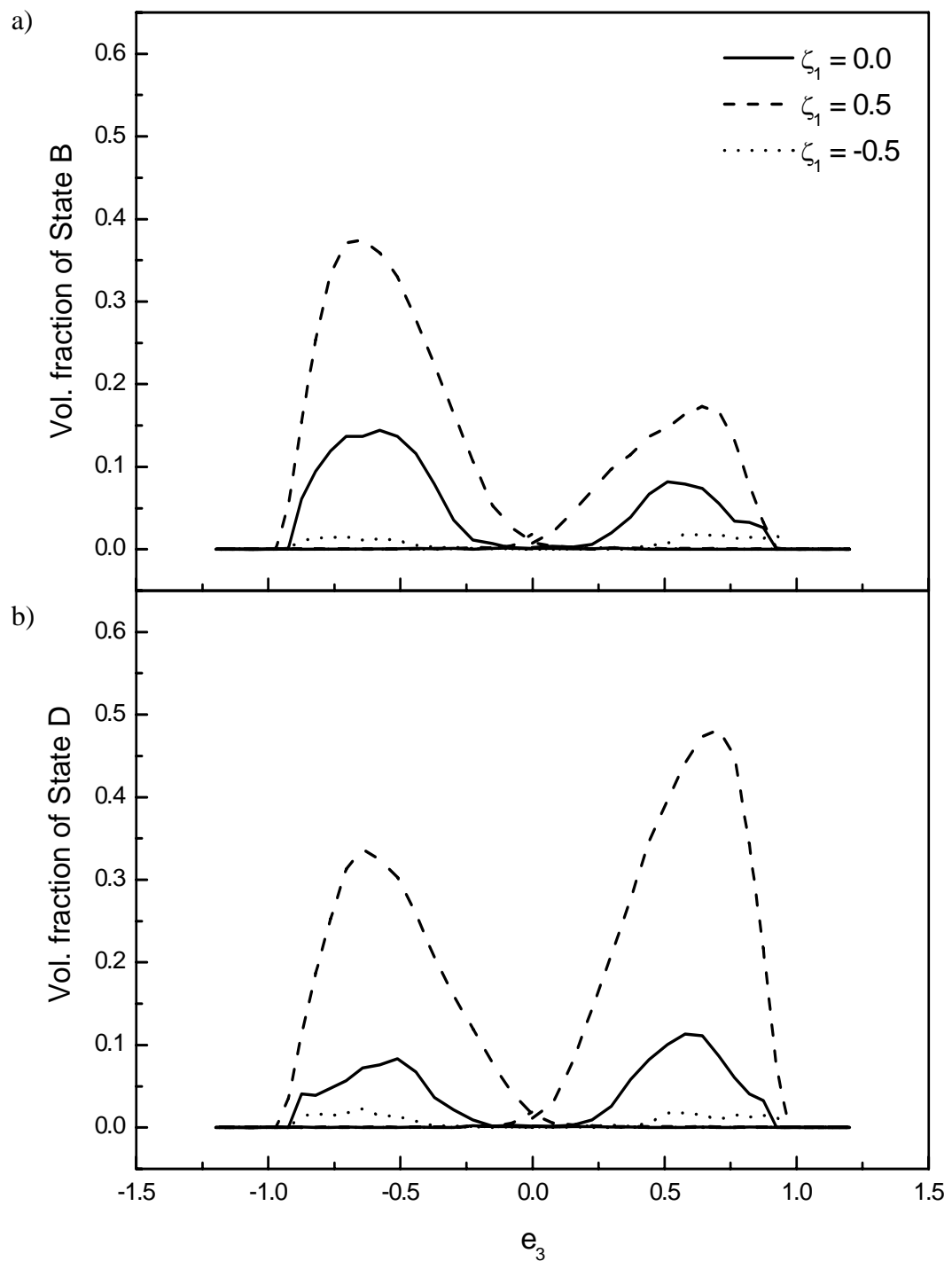


Figure 4.11 Volume fractions of (a) State *B* and (b) State *D* versus electric field under different static transverse stresses ( $\zeta_1 = 0.0, 0.5, -0.5$ )



In addition to the effect of transverse stress, we have also simulated the  $p_3 - e_3$  and  $d_3 - e_3$  loops under different longitudinal stress conditions ( $\zeta_3 = 0.0, 0.2, -0.2$ ) with a fixed switching anisotropy parameter  $\phi_c = 0.45$  as shown in Figures 4.12 and 4.13. The longitudinal and transverse strains,  $\xi_3$  and  $\xi_1$ , driven by an alternating longitudinal electric field under different longitudinal stress conditions are shown in Figures 4.14 (a) and (b), respectively. The corresponding change in volume fractions of each state are shown in Figures 4.15 and 4.16.

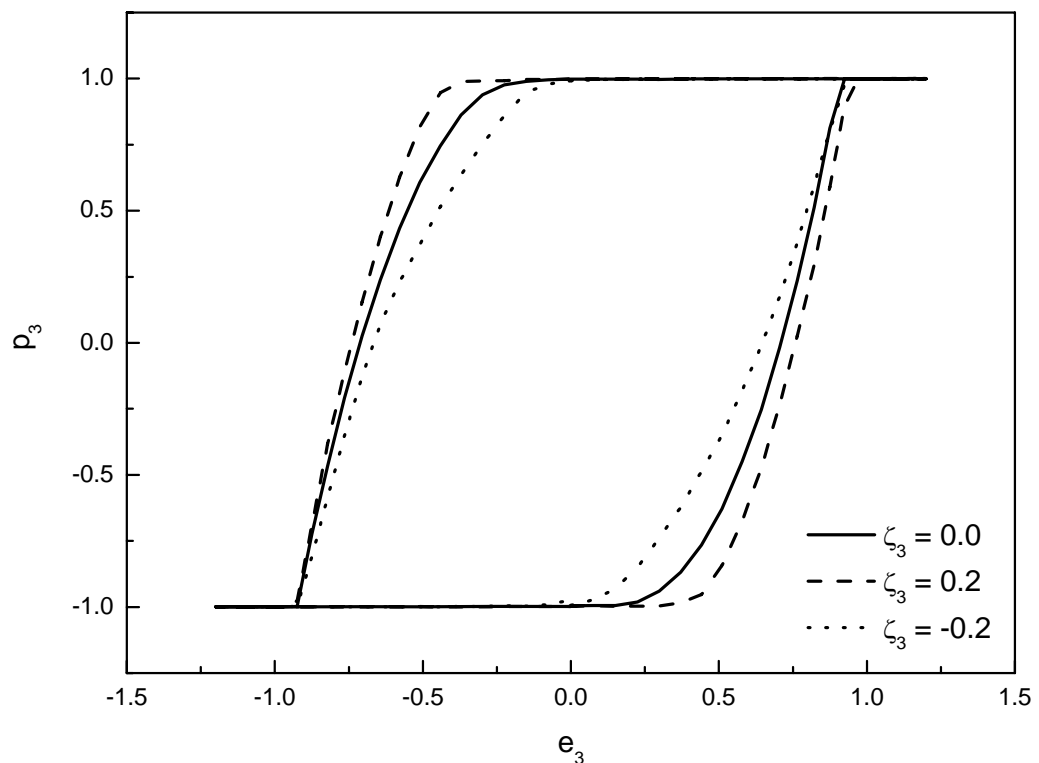


Figure 4.12 Polarization versus electric field under different static longitudinal stresses ( $\zeta_3 = 0.0, 0.2, -0.2$ )

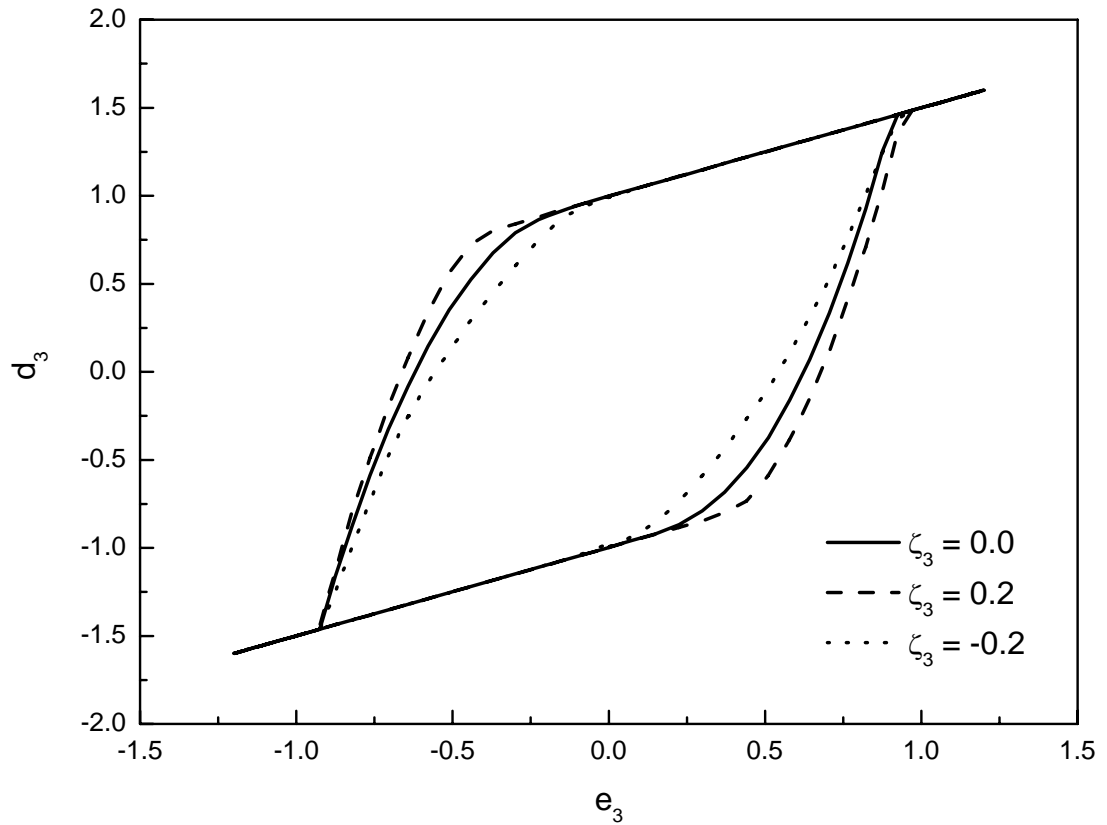


Figure 4.13 Electric displacement versus electric field under static longitudinal stresses ( $\zeta_3 = 0.0, 0.2, -0.2$ )

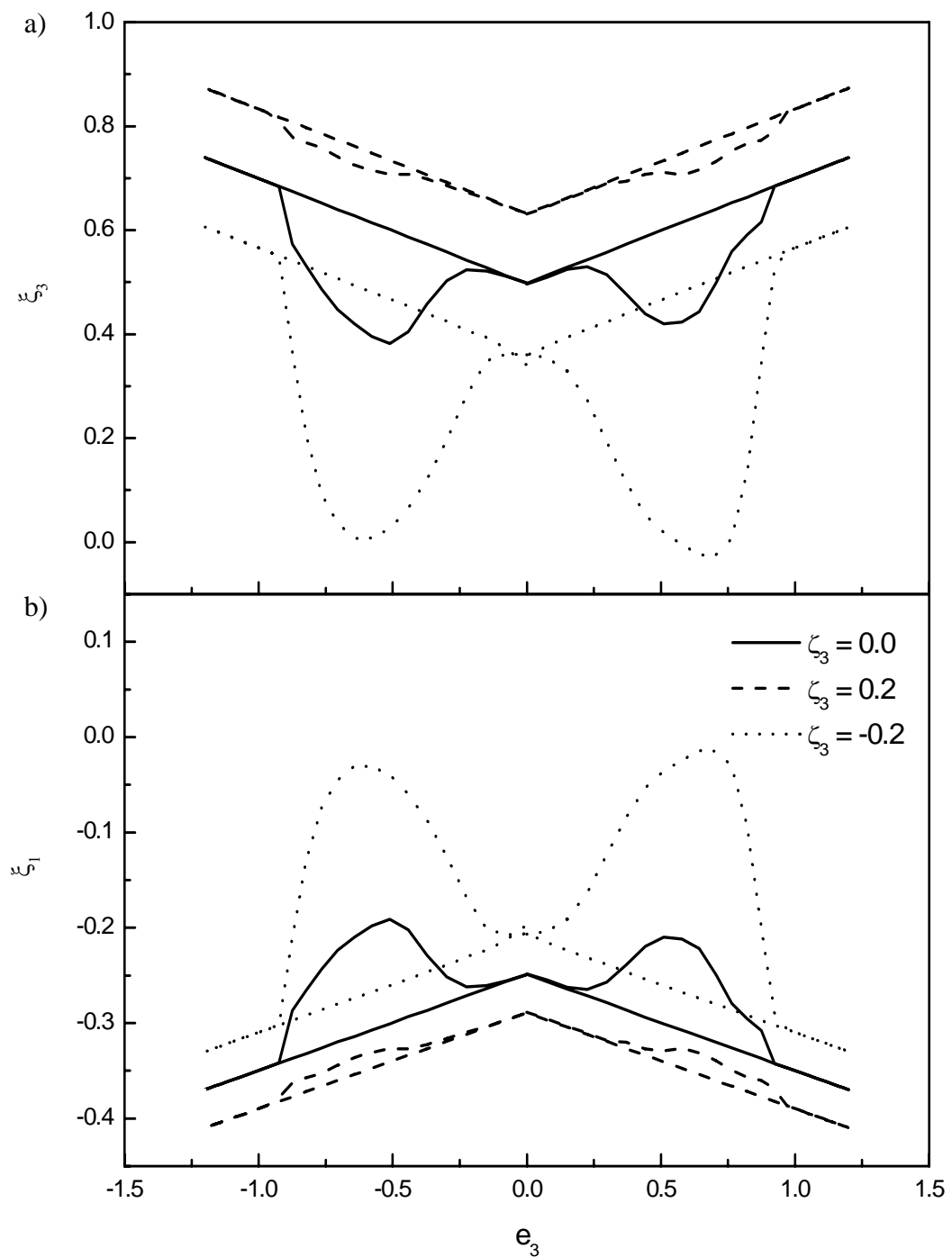


Figure 4.14 (a) Longitudinal strain and (b) transverse strain versus electric field under static longitudinal stresses ( $\zeta_3 = 0.0, 0.2, -0.2$ )

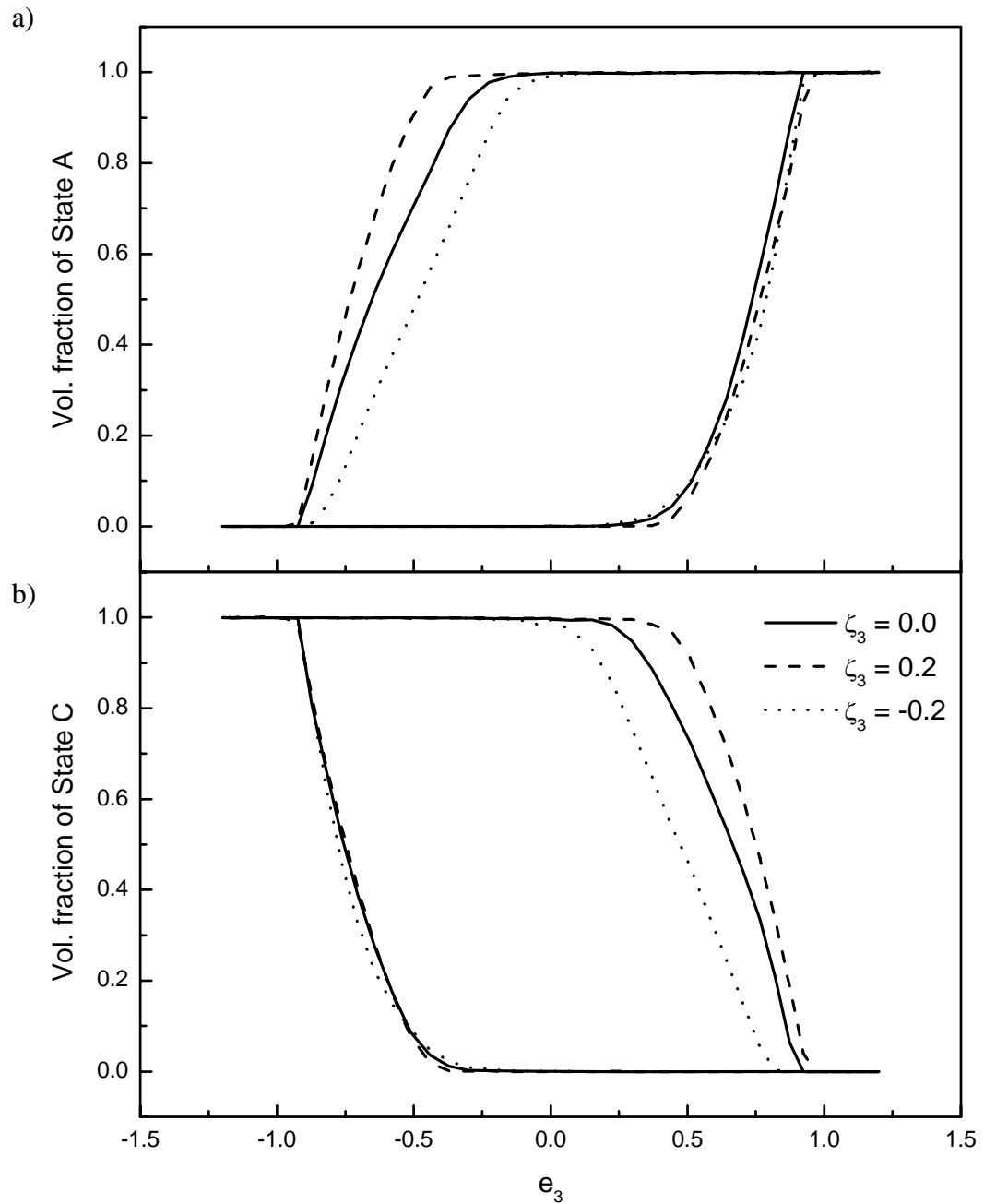


Figure 4.15 Volume fractions of (a) State A and (b) State C versus electric field under static longitudinal stresses ( $\zeta_3 = 0.0, 0.2, -0.2$ )

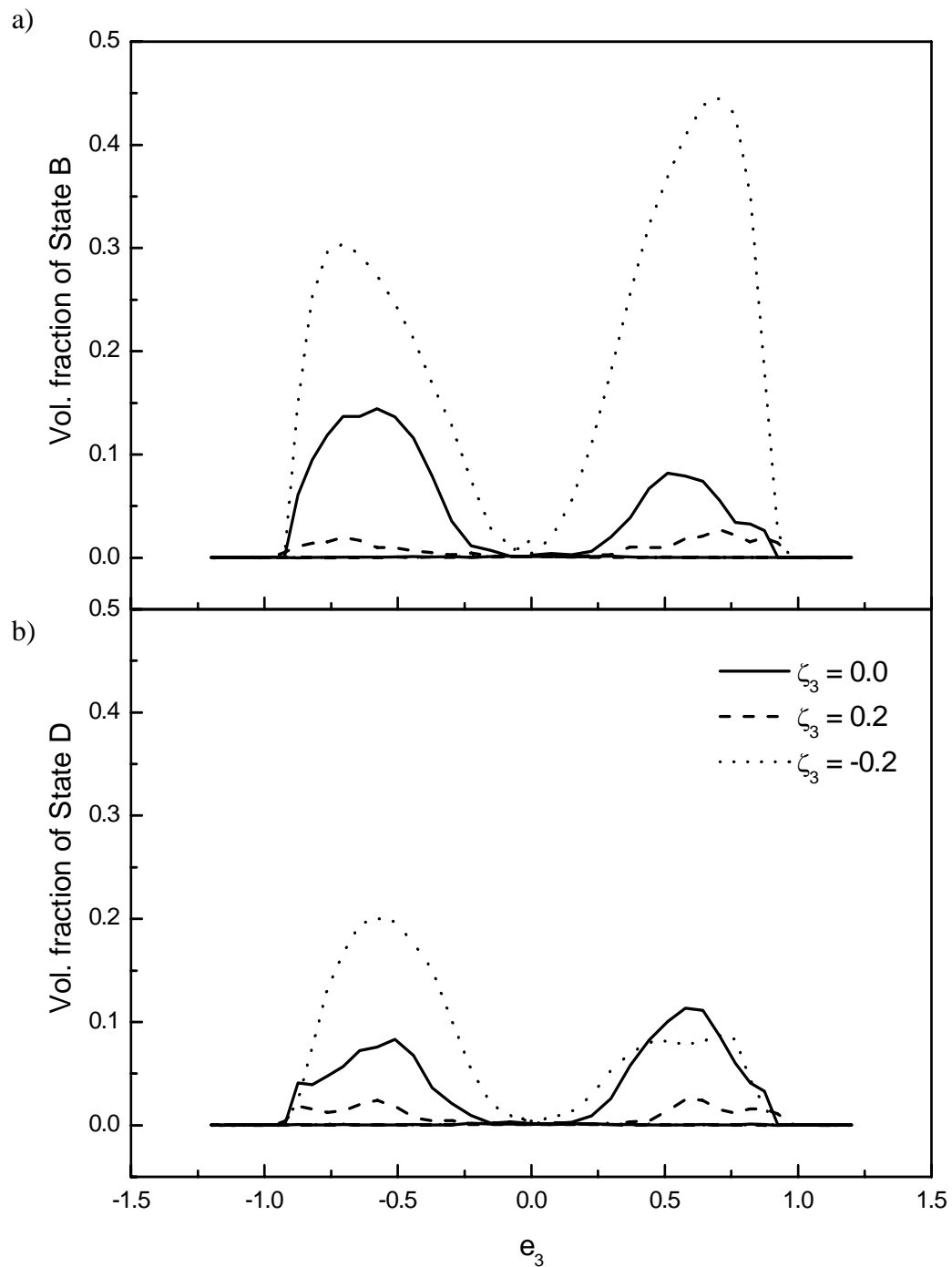


Figure 4.16 Volume fractions of (a) State *B* and (b) State *D* versus electric field under static longitudinal stresses ( $\zeta_3 = 0.0, 0.2, -0.2$ )



From Figure 4.7, both the remnant polarization and coercive field are enhanced under a transverse compressive stress ( $\zeta_1 < 0$ ) but are suppressed under tensile stress ( $\zeta_1 > 0$ ). This conclusion agrees with the experimental result of Lappalainen *et al.* [Lappalainen et al., 1997] from their investigation of the electromechanical properties of PZT thin films under both compressive and tensile stresses at transverse direction. Similar trend is obtained in electric displacement-electric field curves (Figures 4.8). On the other hand, from Figure 4.12, both remnant polarization and coercive field are enhanced under a longitudinal tensile stress ( $\zeta_3 > 0$ ) but reduced under a compressive stress ( $\zeta_3 < 0$ ). Similar trend on the effect of longitudinal stress can be found in lanthanum doped lead zirconate titanate (PLZT) reported by Lynch [Lynch, 1996]. Zhou *et al.* [Zhou, D. Y. et al., 2005] have also obtained similar results. Although it is difficult to incorporate a longitudinal tensile stress on the film, our simulation result can predict an opposite effect for the longitudinal tensile stress.

According to our simulated results, we suggest that dipoles at both states *A* and *C* are encouraged while those at states *B* and *D* are hindered under transverse compressive stress or longitudinal tensile stress. It also enhances the longitudinal polarization. Thus, the longitudinal remnant polarization  $p_r$  increases in the presence of either transverse compressive stress or longitudinal tensile stress. In contrast, the role of longitudinal compressive stress and transverse tensile stress is to suppress dipoles in states *A* and *C*. The dominance of states *B* and *D* gives rise to the reduction of  $p_r$ . The volume fractions of each



state over a cycle are shown in Figures 4.10, 4.11, 4.15 and 4.16 support our discussion.

From Figure 4.9, it is envisaged that the changes in strains of both directions over a cycle are larger under a transverse tensile stress. The corresponding changes under a transverse compressive stress are negligibly small. On a contrary, the change in strains under a longitudinal compressive are the largest, as shown in Figure 4.14, while those under tensile stress are the smallest. The explanation is given in the followings.

At  $\phi_c = 0.45$ , the dipoles are preferentially aligned along the film (at both states *B* and *D*). The application of transverse tensile stress even enhances this preferential alignment. Consequently, in the absence of the applied electric field, the transverse strain is large and the longitudinal strain is small. By the application of longitudinal electric field, these dipoles start rotating to either *A* or *C* states, depending on the sign of *E*. This leads to the increase of longitudinal strain and decrease in transverse strain. Upon the disappearance of the external electric field, dipoles restore to their initial conditions because of the influence of transverse stress and orientation anisotropy. The application of an electric field at negative direction yields identical result. Under this situation, the transverse strain creates the largest changes both for the transverse and longitudinal strains. On the other hand, under a transverse compressive stress, nearly most of the dipoles are preferentially aligned along *z*-axis (at both states *A* and *C*) even in the absence of external electric field. The application of the



longitudinal electric field does not affect the alignment of dipoles so much. Therefore, the changes in strains are small.

The presence of longitudinal stress produces exactly opposite trends on the changes in strains, as shown in Figures 4.14 (a) and (b), respectively. The longitudinal tensile stress reduces the area in both  $\xi_3$  and  $\xi_1$  versus  $e_3$  butterfly loops whereas these loop areas are enlarged by the application of longitudinal compressive stress. However, as the magnitude of static compressive stress increases (in Figure 4.17), the loop area decreases again. In general, the longitudinal compressive stress forces the dipoles to be preferentially aligned along the film (both states *B* and *D*), resulting in a small longitudinal strain and a large transverse strain. If the longitudinal external field is large enough, the dipoles can be switched to energetically favorable states, either states *A* or *C*, increasing the longitudinal strain and reducing the transverse strain. Consequently, an adequate longitudinal compressive stress can create larger changes in strains than that under the unstrained case. On the other hand, if the compressive stress is too large (in Figure 4.17), all dipoles are clamped along the transverse direction that the switching is difficult because it requires a very large electric field to activate the rotation, as shown in Figure 4.18 and 4.19. The butterfly curve then becomes smaller and finally constricts to a line. This explanation can be supported by the graphs of volume fractions in Figures 4.18 and 4.19. The volume fractions of dipoles at States *A* and *C* remain in a very low value under a compressive stress  $\zeta = -1.5$ . Those in States *B* and *D* remain in a value of 0.5. The experimental result from Zhou *et al.* [Zhou, D. Y. et al.,



2005] on the investigation of electromechanical properties of the  $\text{Pb}(\text{Ni}_{1/3}\text{Sb}_{2/3})\text{O}_3\text{-PbTiO}_3\text{-PbZrO}_3$  system confirms our conclusion. Similar to our simulation results, the strain–electric field butterfly loop is gradually enlarged on increasing the compressive stress and attains a maximum loop area when the stress value is about 25 MPa. The loop area then gradually shrinks and finally reduces to a horizontal line at a very large stress value.

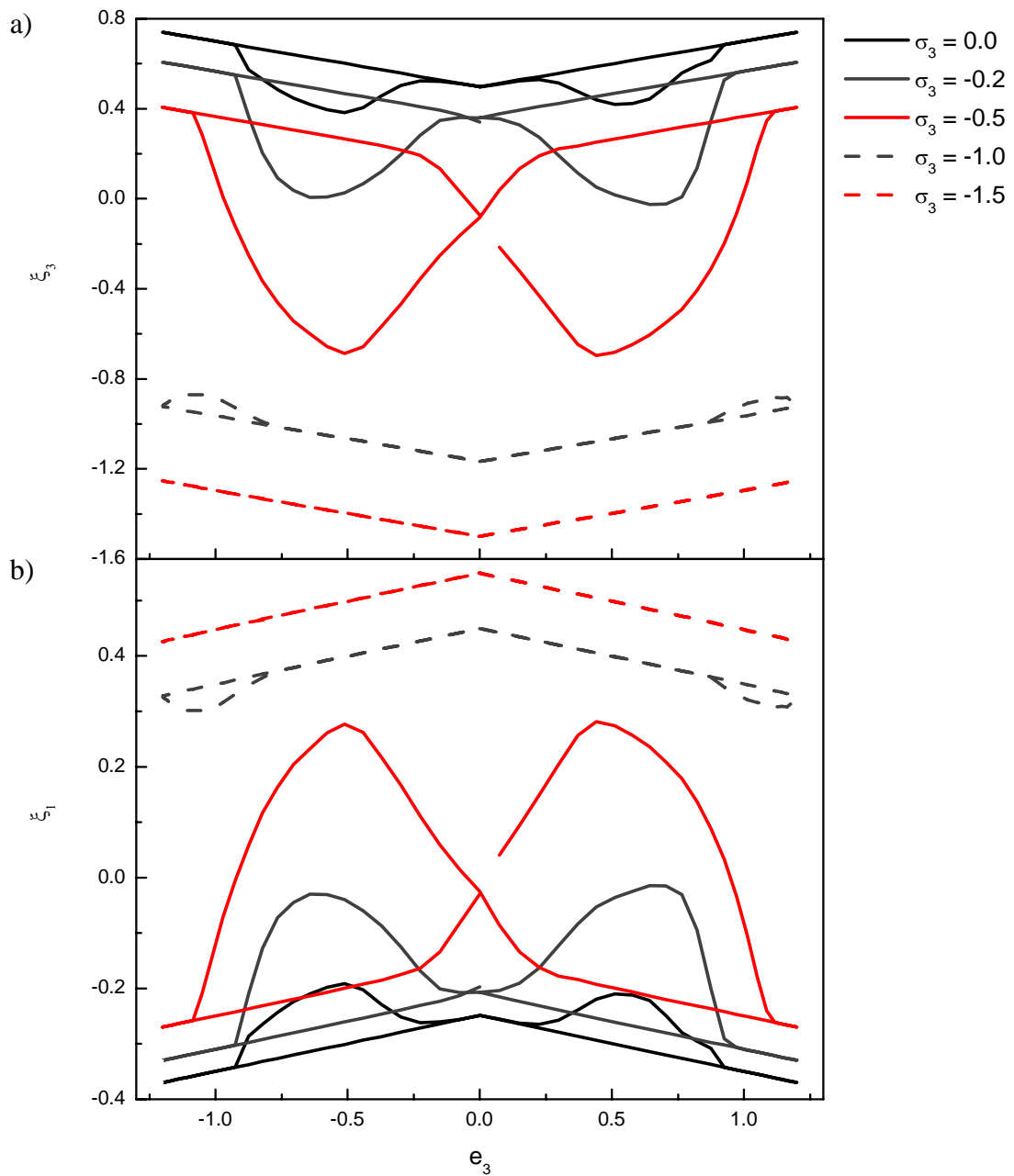


Figure 4.17 (a) Longitudinal strain and (b) transverse strain versus electric field under different magnitudes of longitudinal compressive stresses ( $\sigma_3 = 0.0, -0.2, -0.5, -1.0, -1.5$ )

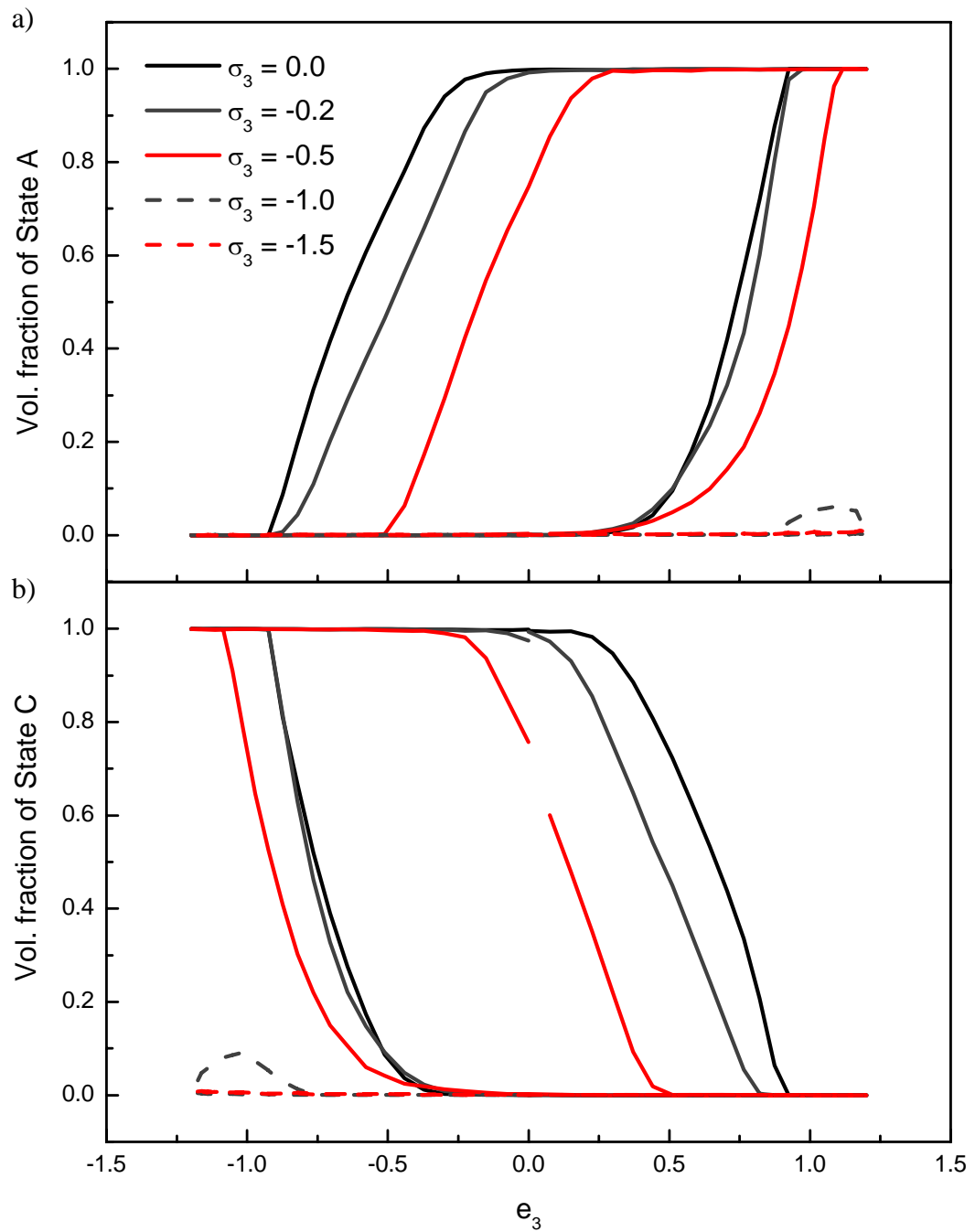


Figure 4.18 Volume fractions of (a) State A and (b) State C versus electric field under different magnitudes of longitudinal compressive stresses ( $\zeta_3 = 0.0, -0.2, -0.5, -1.0, -1.5$ )

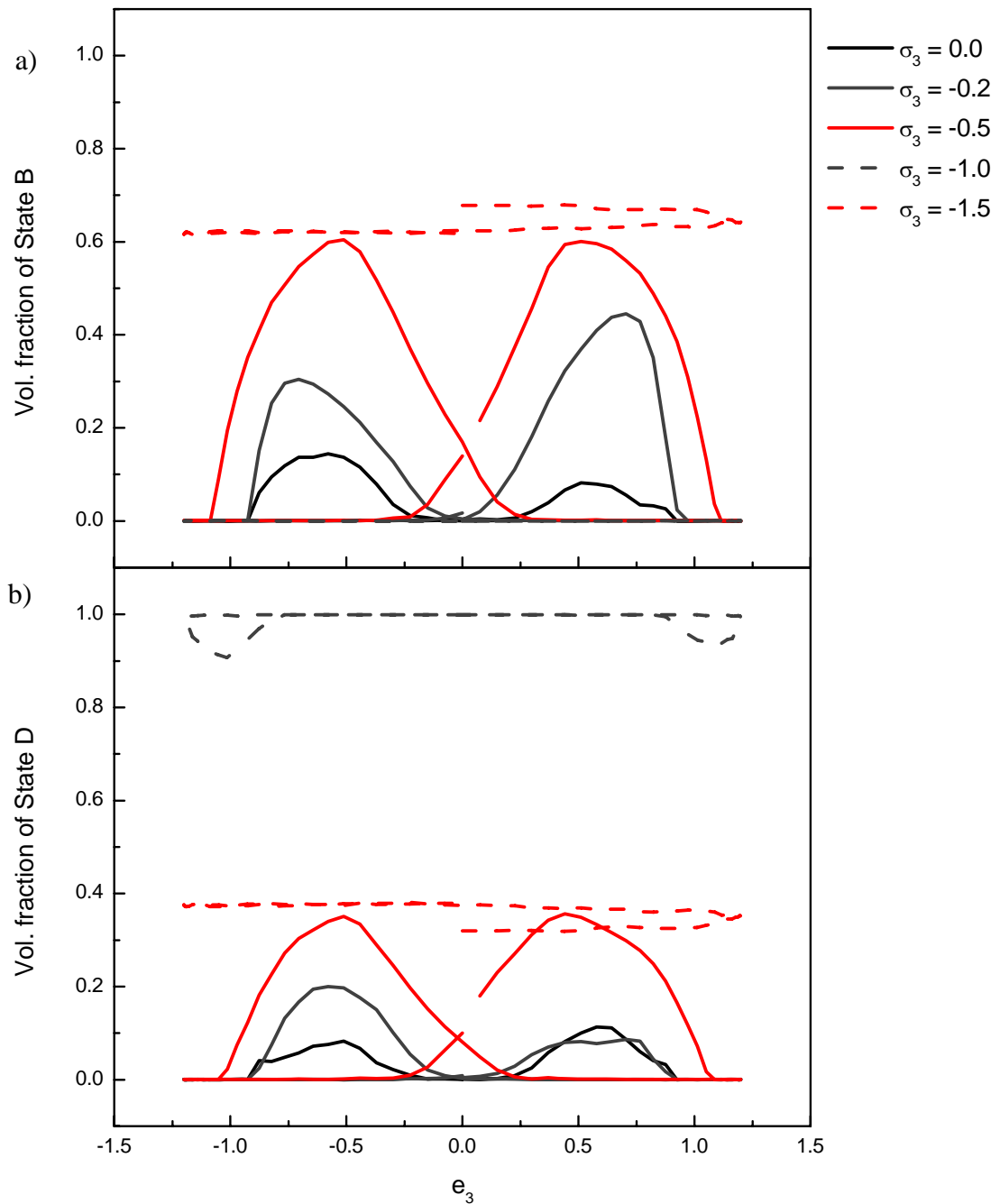


Figure 4.19 Volume fractions of (a) State *B* and (b) State *D* versus electric field under different magnitudes of longitudinal compressive stresses ( $\sigma_3 = 0.0, -0.2, -0.5, -1.0, -1.5$ )



In addition to the influence on the areas of the butterfly loops, the presence of stress also induces a vertical shift of the loop. As mentioned in Chapter 2, there is an elastic strain component because of the elastic deformation in the presence of stress. This response causes the vertical drift in the strain–electric field diagram, as shown in Figures 4.20 and 4.21. In Figure 4.20,  $\xi_3 - e_3$  curve shifts upward and  $\xi_1 - e_3$  curve shifts downward under transverse compressive stress. Conversely, the presence of transverse tensile stress induces opposite shifting directions for both curves. In Figures 4.21, the roles of compressive and tensile stresses on the shifting directions are reverse. The effect of longitudinal compressive stress on the shifting direction of butterfly curves is confirmed by the experimental result of Zhou et al.

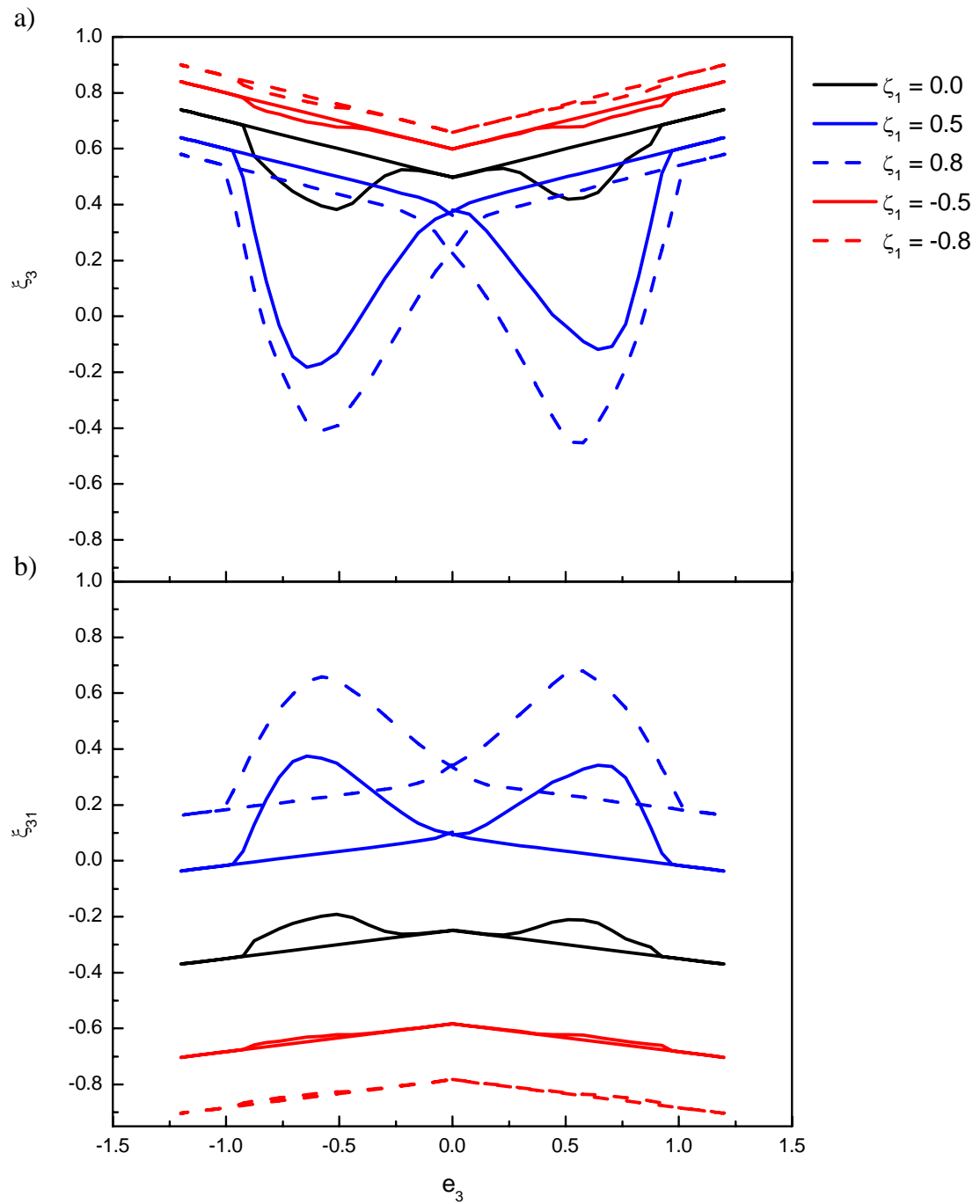


Figure 4.20 (a) Longitudinal strain and (b) transverse strain versus electric field under different transverse static stresses ( $\zeta_1 = 0.0, 0.5, 0.8, -0.5, -0.8$ )

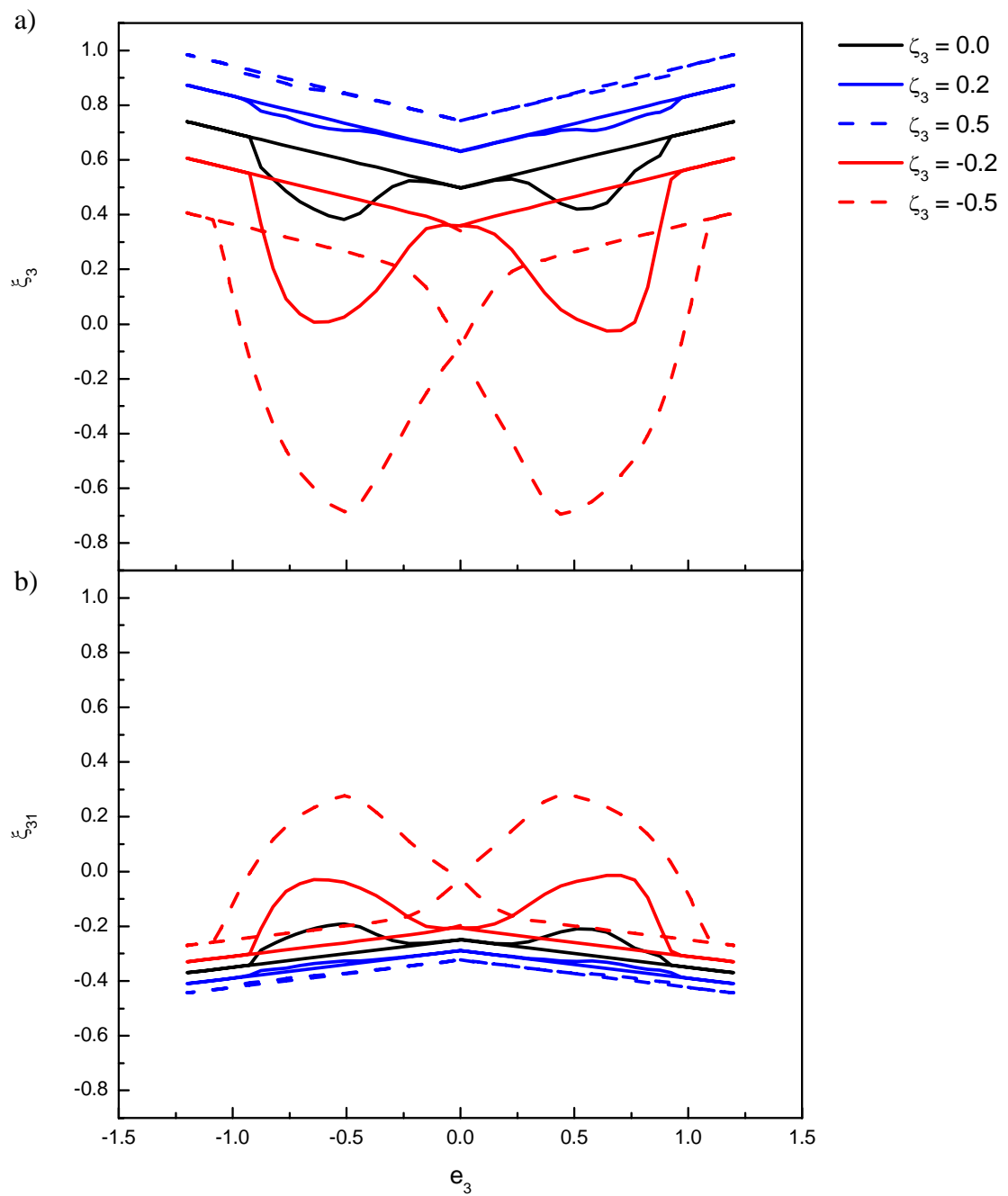


Figure 4.21 (a) Longitudinal strain and (b) transverse strain versus electric field under different longitudinal static stresses ( $\zeta_3 = 0.0, 0.2, 0.5, -0.2, -0.5$ )



#### 4.2.4 Effects of anisotropic switching

The effects of switching anisotropy parameter  $\phi_c$  on the polarization, electric displacement, longitudinal and transverse strains are shown in Figures 4.22, 4.23 and 4.24, respectively. We have used the following parameters:  $\Gamma_{MCS} = 350$  (MCS/dipole),  $e_3 = 1.2$ ,  $\bar{T} = 0.8$ ,  $\xi_0 = 0.5$ ,  $h_3 = 0.5$ ,  $Y' = 1.5$ ,  $\nu = 0.3$ ,  $\zeta_{crit} = 0.3$ ,  $k = 0.1$ ,  $n = 0.5$ ,  $\alpha' = 0.1$ ,  $d'_{33} = 0.2$ ,  $d'_{31} = -0.1$ ,  $\kappa' = 0.5$ ,  $N_x = 150$ , and  $N_z = 80$ .

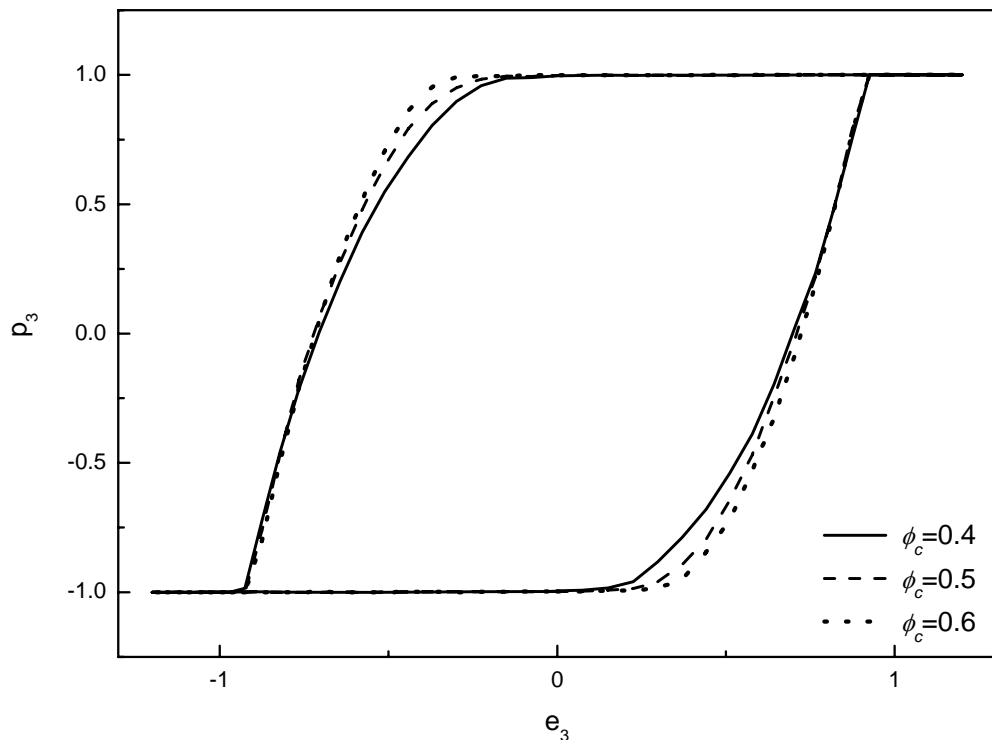


Figure 4.22 Polarization versus electric field under stress-free condition with different volume fraction of  $c$ -domains ( $\phi_c = 0.4, 0.5, 0.6$ )

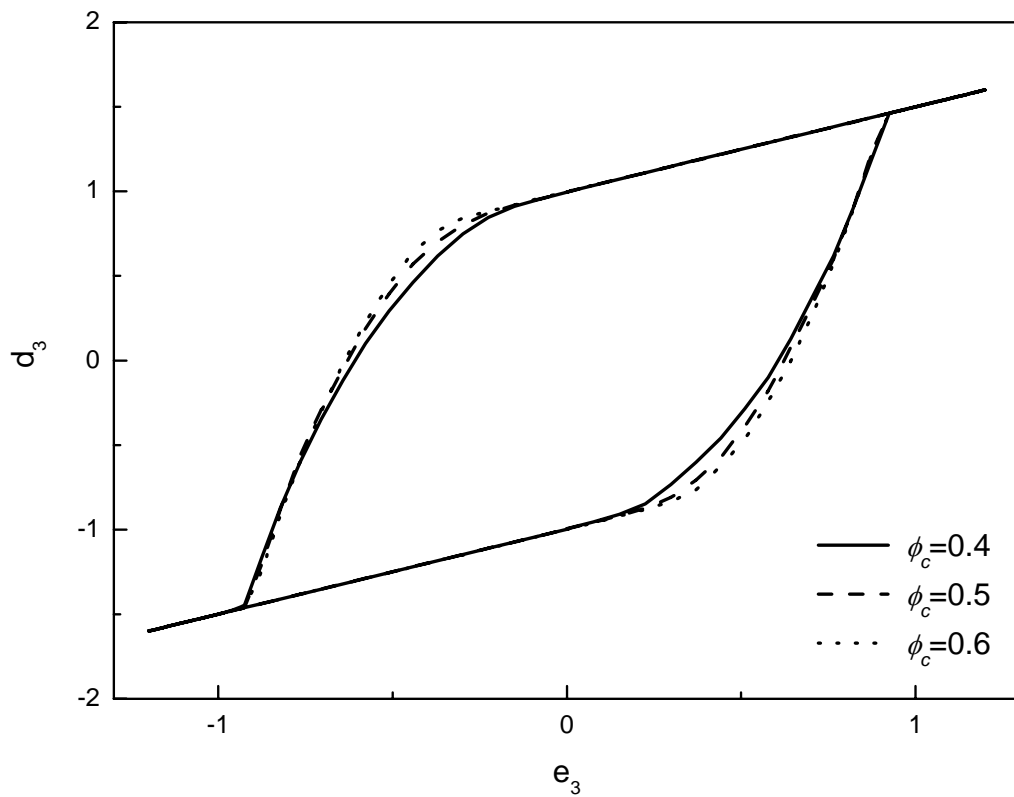


Figure 4.23 Electric displacement versus electric field under stress-free condition with different volume fraction of  $c$ -domains ( $\phi_c = 0.4, 0.5, 0.6$ )

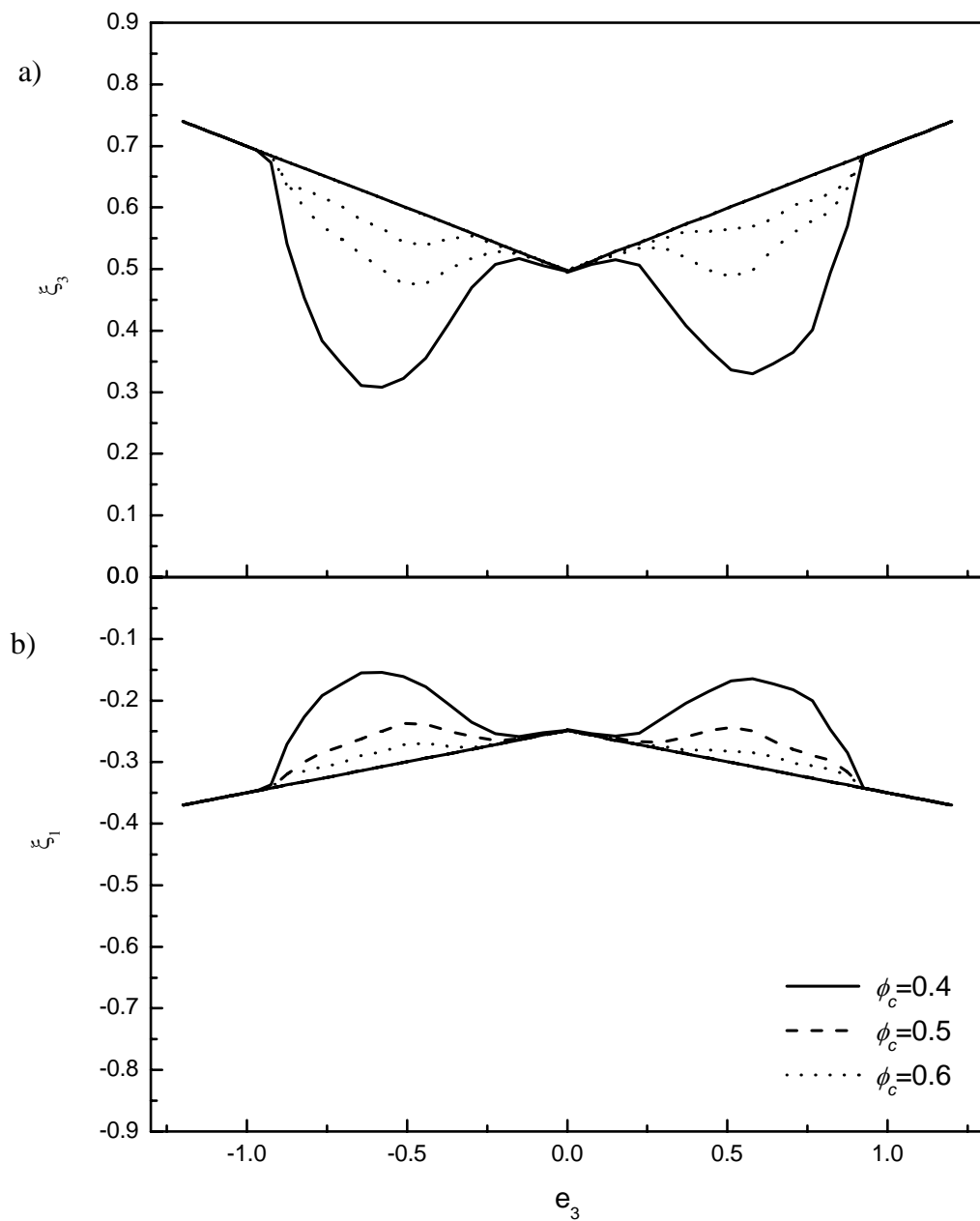


Figure 4.24 (a) Longitudinal strain and (b) transverse strain versus electric field under stress-free condition ( $\zeta_3 = \zeta_1 = 0.0$ ) with different volume fraction of  $c$ -domains ( $\phi_c = 0.4, 0.5, 0.6$ )

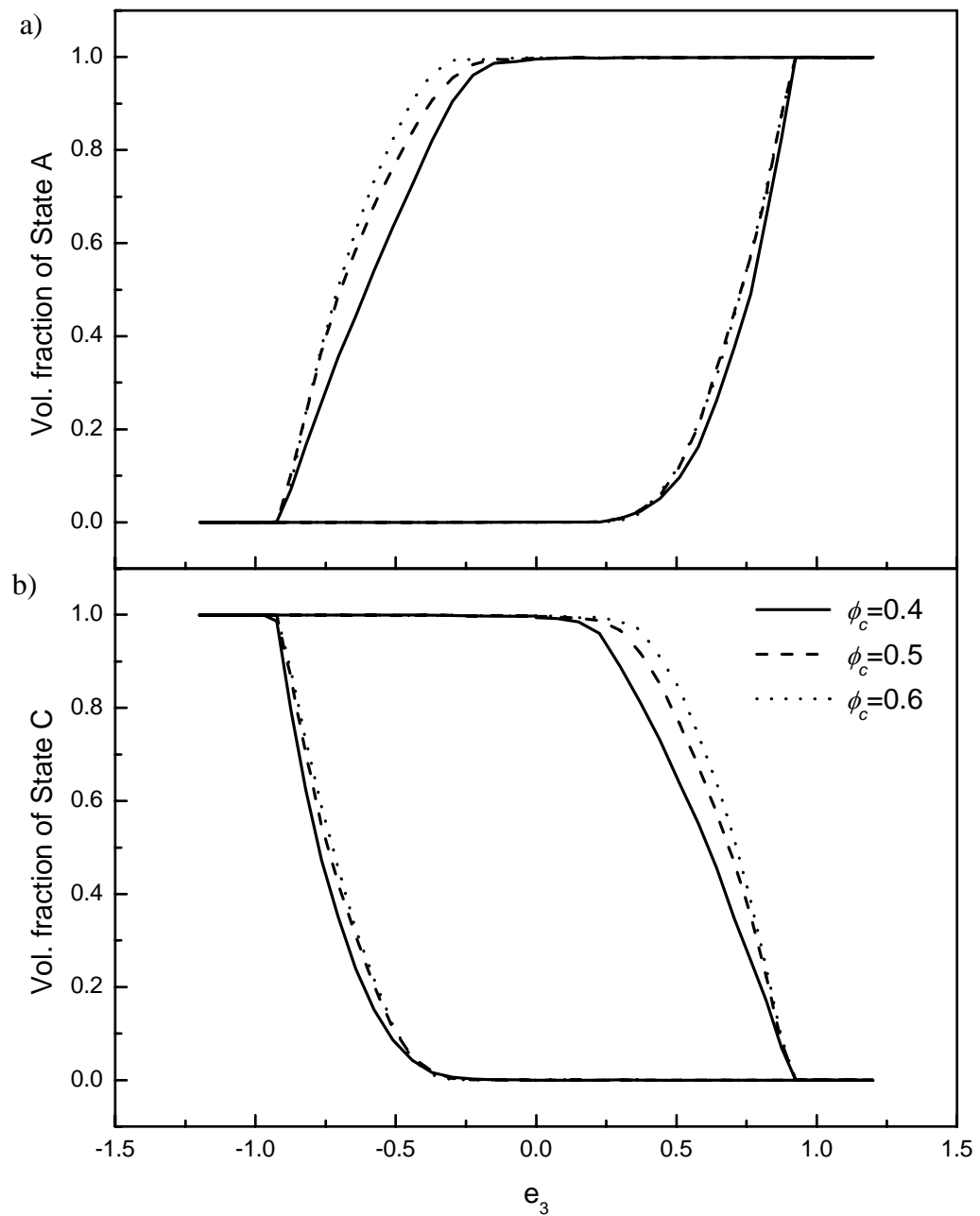


Figure 4.25 Volume fractions of (a) State A and (b) State C versus electric field under different stress-free condition ( $\zeta_3 = \zeta_1 = 0.0$ ) with different volume fraction of  $c$ -domains ( $\phi_c = 0.4, 0.5, 0.6$ )

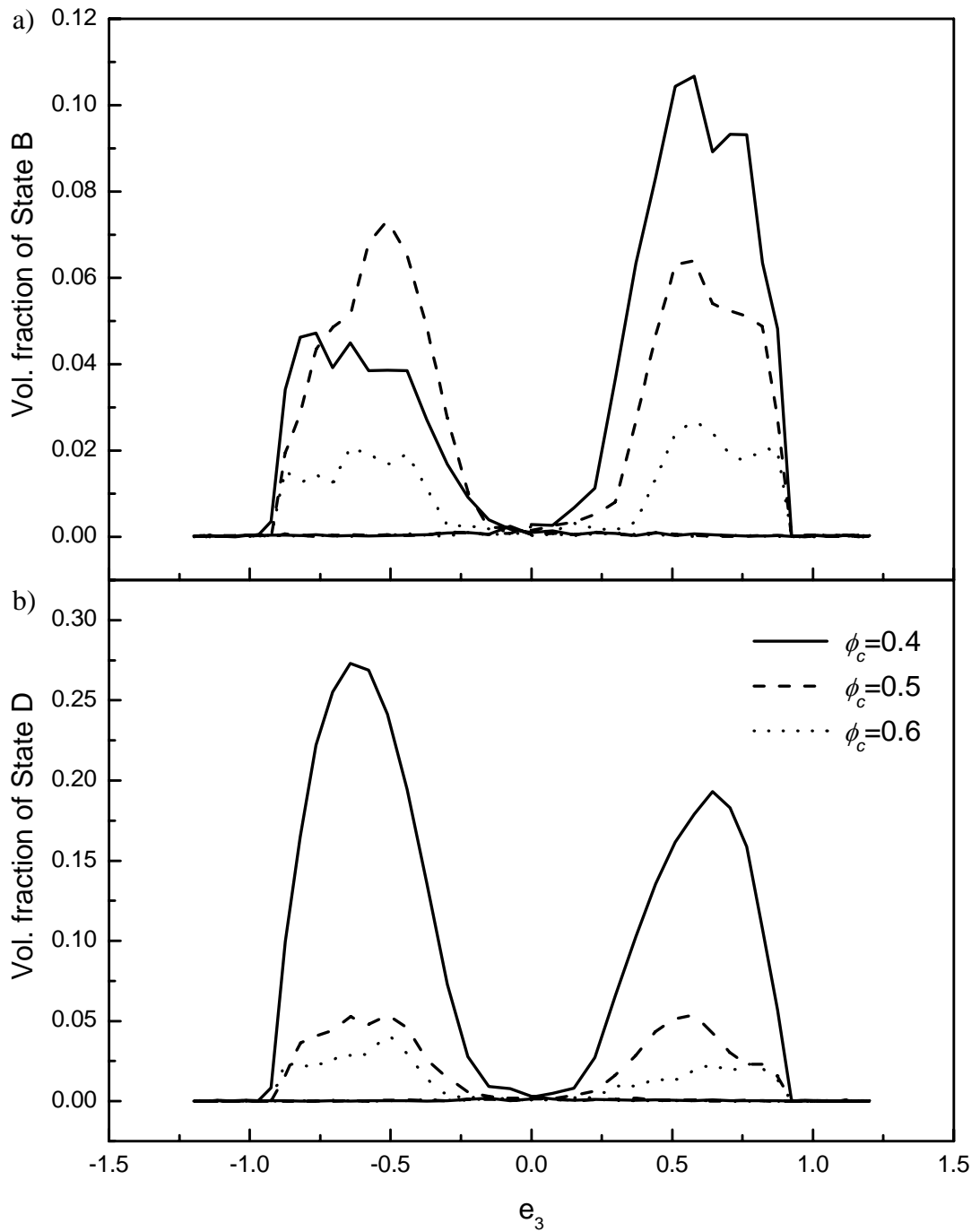


Figure 4.26 Volume fractions of (a) State  $B$  and (b) State  $D$  versus electric field under different stress-free condition ( $\zeta_3 = \zeta_1 = 0.0$ ) with different volume fraction of  $c$ -domains ( $\phi_c = 0.4, 0.5, 0.6$ )



From Figure 4.22, the remnant polarization increases with the value of  $\phi_c$ . As described in Chapter 3, the orientation of a film depends on the growth condition as well as the choice of substrate. Due to the anisotropic effect, it establishes a preferential direction for the orientation of the dipoles. For a  $c$ -domain-dominated film ( $\phi_c > 0.5$ ), the preferential orientation of dipoles is along  $z$ -direction whereas the dipoles preferentially align along  $x$ -direction for an  $a$ -domain-dominated film ( $\phi_c < 0.5$ ). The volume fraction of  $c$ -domains is therefore larger than that of  $a$ -domains in a  $c$ -domain-dominated film (i.e.,  $\phi_c > \phi_a$ ) and vice versa. The remnant polarization of a  $c$ -domain-dominated film is larger than that of an  $a$ -domain-dominated film.

In Figure 4.24, the loop areas for the longitudinal and transverse strains are maximum for  $\phi_c = 0.4$  and minimum for  $\phi_c = 0.6$ . In other words, the loop area decreases on increasing the switching anisotropy parameter  $\phi_c$ . In the absence of stress, the strain response is contributed by ferroelastic and field induced components. As all of the samples are subject to identical electrical loading, only the ferroelastic contribution makes the difference. For small  $\phi_c$ , say  $\phi_c = 0.4$ , most of dipoles are aligned along the film and  $a$ -domains dominate (in Figures 4.25 and 4.26). This results in a large transverse strain and small longitudinal strain. The application of longitudinal electric field causes a number of dipoles rotating towards  $A$  or  $C$  states, resulting in an increase in longitudinal strain and reduction of transverse strain. The large changes in strains are then reflected by the large loop areas. To the other extreme, for large  $\phi_c$ , most of the dipoles are preferentially aligned along the longitudinal direction



(either  $A$  or  $C$  states), the application of electric field does not affect them so much because most of them are already in States  $A$  or  $C$ . Consequently, there is not much change in both longitudinal and transverse strains. Small loop areas are then obtained.



### **4.3 *Effect of combined alternating electrical and mechanical loadings***

#### **4.3.1 Experimental observations**

While most of the study are focused on the effect of static stress, Mitrovic et al. [Mitrovic et al., 2001] and Zhou et al. [Zhou, D. Y. and Kamlah, 2004] have investigated the effect of alternating stress. In particular, they have characterized the electromechanical responses of six piezoelectric stack actuators and a commercial soft PZT material under combined electrical and mechanical loadings. Zhou and his coworkers have subject the sample by an alternating longitudinal compressive stress which was either in-phase or out-of-phase with the alternating electric field as shown in Figures 4.27(a) and 4.27(b), respectively. From Zhou's definition, the "in-phase" condition is defined as the case where both the electric field and the compressive stress attain maximum simultaneously, whereas the "out-of-phase" condition is the one where the electric field attains a maximum value at the moment of minimal compressive stress (Figures 4.27(b)).

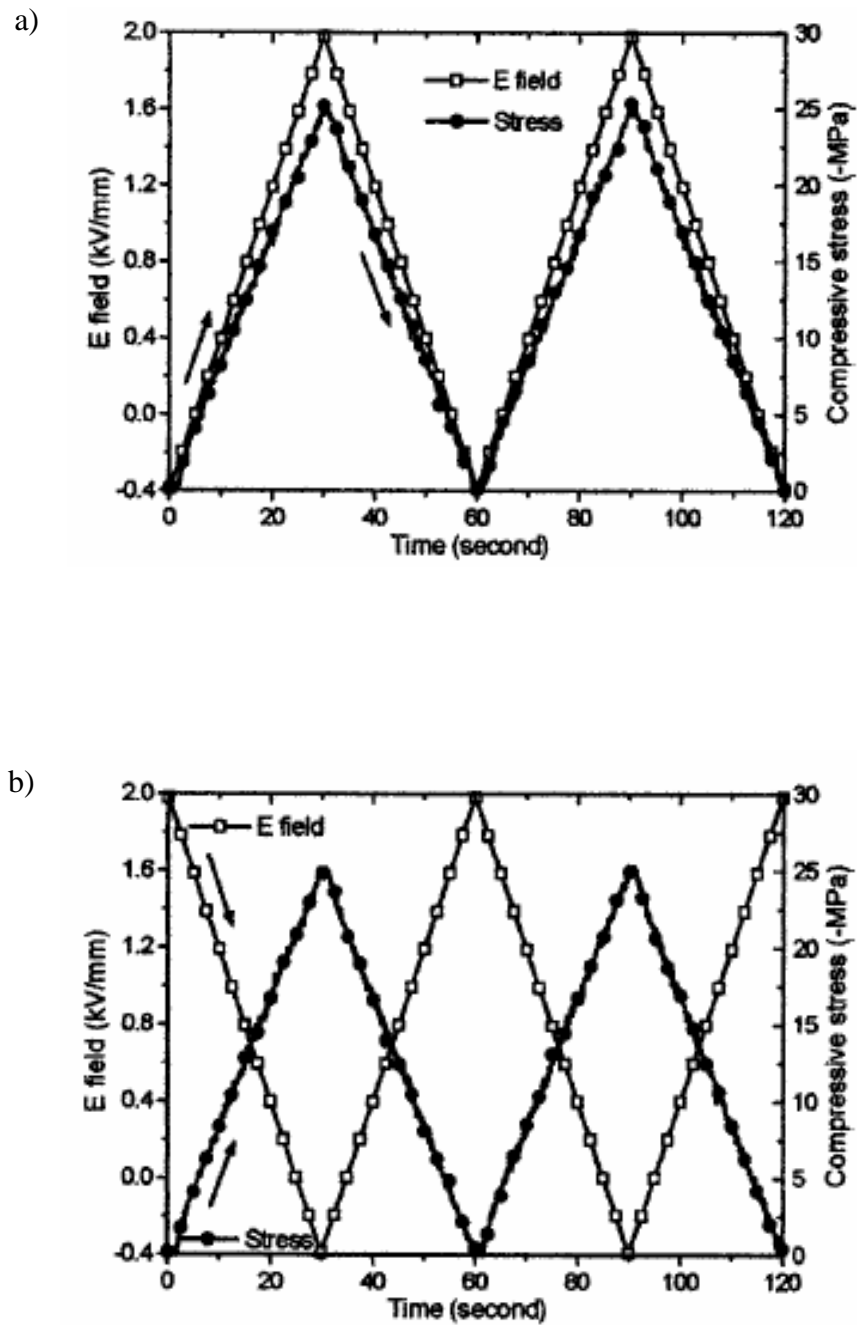


Figure 4.27 Electric-field-time and stress-time patterns in which the maximum stress is zero (released compression). (a) In-phase loading. (b) Out-of-phase loading. [Zhou, D. Y. and Kamlah, 2004]



The experimental  $D$ - $E$  and  $\varepsilon$ - $E$  loops under in-phase, out-of-phase and stress free conditions are shown in Figures 4.28(a) and 4.28(b). Even in the stress-free condition, nonlinearity and hysteresis are observed from both  $D$ - $E$  and  $\varepsilon$ - $E$  loops. For the in-phase condition, both  $D$ - $E$  and  $\varepsilon$ - $E$  loops are significantly reduced. On the other hand, these loops are significantly enlarged under the out-of-phase condition. Zhou and Kamlah have attributed this novel phenomenon to the non-180° domain switching. There is so far no other comprehensive explanation on this experimental account. We are trying to reproduce these experimental results based on our present model.

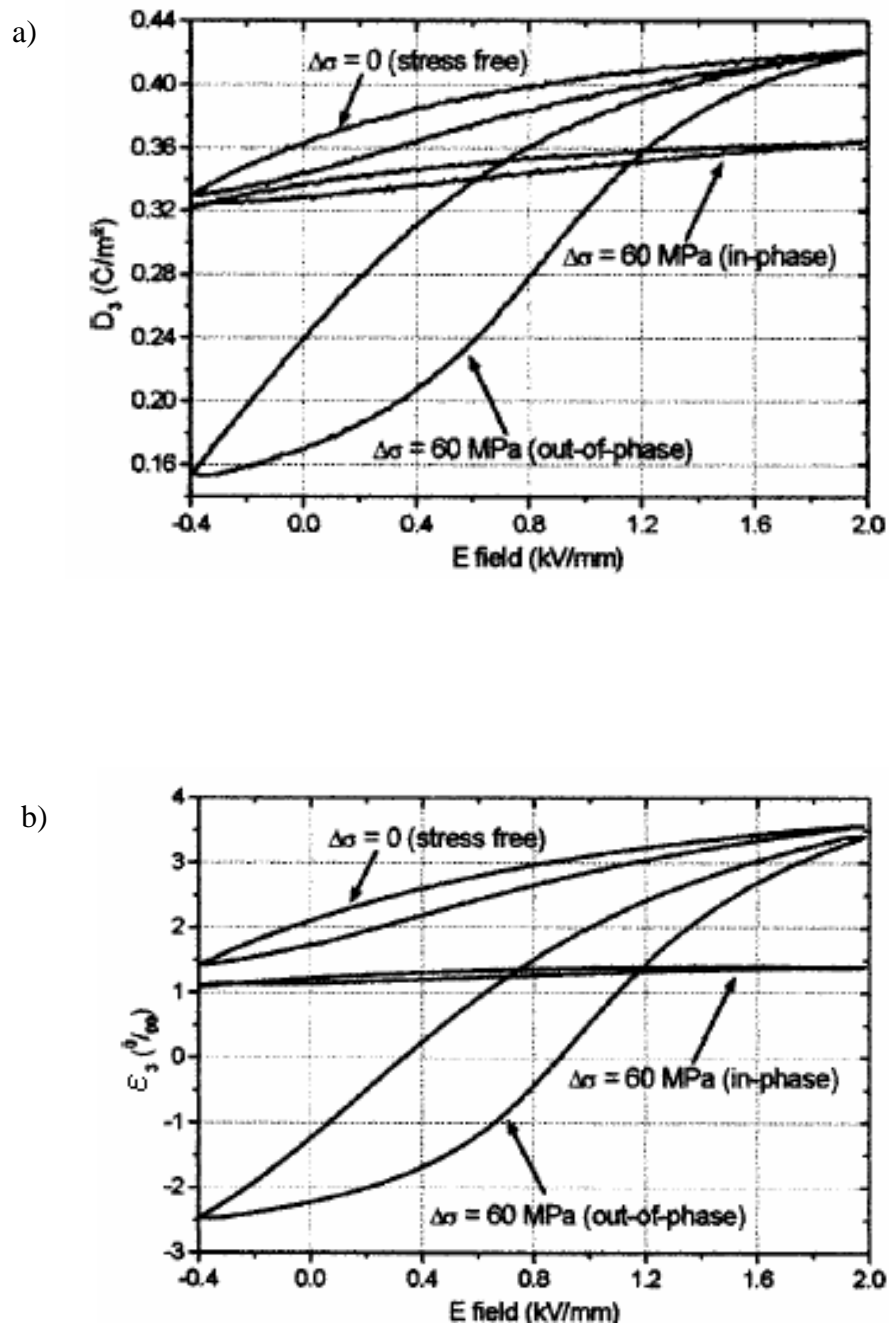


Figure 4.28 Comparison of the (a) electric displacement and (b) strain behavior in the stress-free state, under in-phase and out-of-phase electromechanical loading with zero-maximum stress. [Zhou, D. Y. and Kamlah, 2004]



### 4.3.2 Simulation

Similar to Section 4.2, an external longitudinal electric field is applied to the system. However, it is replaced by a ramp-shape field. The applied electric field  $E$  is supposed to be homogeneous and orthogonal to the film surfaces ( $E_1 = E_2 = 0, E_3 \neq 0$ ). The longitudinal electric field can be expressed as follow:

$$t' = \text{Mod}(t, \Gamma)$$

$$E = E_{dc} + E_0 \frac{4t'}{\Gamma} \quad (0 \leq t' \leq \Gamma/4)$$

$$E = E_{dc} + E_0 - \frac{4E_0}{\Gamma} \left( t' - \frac{\Gamma}{4} \right) \quad (\Gamma/4 \leq t' \leq 3\Gamma/4) \quad (4.6)$$

$$E = E_{dc} + \frac{4E_0}{\Gamma} \left( t' - \frac{3\Gamma}{4} \right) - E_0 \quad (3\Gamma/4 \leq t' \leq \Gamma)$$

where  $\text{mod}(x,y)$  is the remainder function returning the remainder of the division of  $x/y$ ,  $t$  is time,  $\Gamma$  is the period of the electric field, and  $E_{dc}$  and  $E_0$  are the static field and the magnitude of the alternating field, respectively.



In addition to the electric field, the applied alternating longitudinal compressive stress  $\sigma$  is homogeneous in space and can be expressed as follow:

$$\begin{aligned}t' &= \text{Mod}(t + \tau, \Gamma) \\ \sigma_3 &= \sigma_{dc} + \sigma_0 \frac{4t'}{\Gamma} & (0 \leq t' \leq \Gamma/4) \\ \sigma_3 &= \sigma_{dc} + \sigma_0 - \frac{4\sigma_0}{\Gamma} \left( t' - \frac{\Gamma}{4} \right) & (\Gamma/4 \leq t' \leq 3\Gamma/4) \\ \sigma_3 &= \sigma_{dc} + \frac{4\sigma_0}{\Gamma} \left( t' - \frac{3\Gamma}{4} \right) - \sigma_0 & (3\Gamma/4 \leq t' \leq \Gamma)\end{aligned} \quad (4.7)$$

where  $\phi = 2\pi(\tau/\Gamma)$  is the phase difference between the applied field and stress,  $\sigma_{dc}$  and  $\sigma_0$  are the static stress and the amplitude of alternating stress, respectively. If  $\sigma_{dc} \leq -\sigma_0$ , then the longitudinal stress is purely compressive, regardless of time. Moreover, if  $\phi = (2n+1)\pi$ , both loadings are out of phase; if  $\phi = 2n\pi$ , both are in phase.

The longitudinal polarization, electric displacement and longitudinal strain at particular instance can be evaluated by Eqns. (3.24), (3.25) and (3.27), respectively. The  $D_3 - E_3$  and  $\varepsilon_3 - E_3$  loops under three different loading conditions, i.e., in-phase, out-of-phase and stress-free were then simulated.



### 4.3.3 Results and discussion

The electric displacement versus electric field loops and the longitudinal strain versus electric field loops have been evaluated numerically under different mechanical loading conditions. In these calculations, it is assumed that a residual static in-plane compressive stress exist in the film, i.e.,  $\zeta_1 = -0.05$ . In our calculation, we have used the following normalized parameters:  $\phi_c = 0.45$ ,  $\Gamma_{MCS} = 300$  (MCS/dipole),  $e_{dc} = 0.2$ ,  $e_0 = 0.3$ ,  $\bar{T} = 1.0$ ,  $\xi_0 = 0.5$ ,  $h_3 = 0.3$ ,  $Y' = 1.5$ ,  $\nu = 0.3$ ,  $\zeta_{dc} = -0.2$ ,  $\zeta_0 = 0.2$ ,  $\zeta_{crit} = 0.3$ ,  $k = 0.1$ ,  $n = 0.5$ ,  $\alpha' = 0.1$ ,  $d'_{33} = 0.2$ ,  $d'_{31} = -0.1$ ,  $\kappa' = 0.45$ ,  $N_x = 150$ , and  $N_z = 80$ . The normalized electric displacement-electric field loops and longitudinal strain-electric field loops under different electromechanical loading conditions are shown in Figures 4.29 and 4.30, respectively.

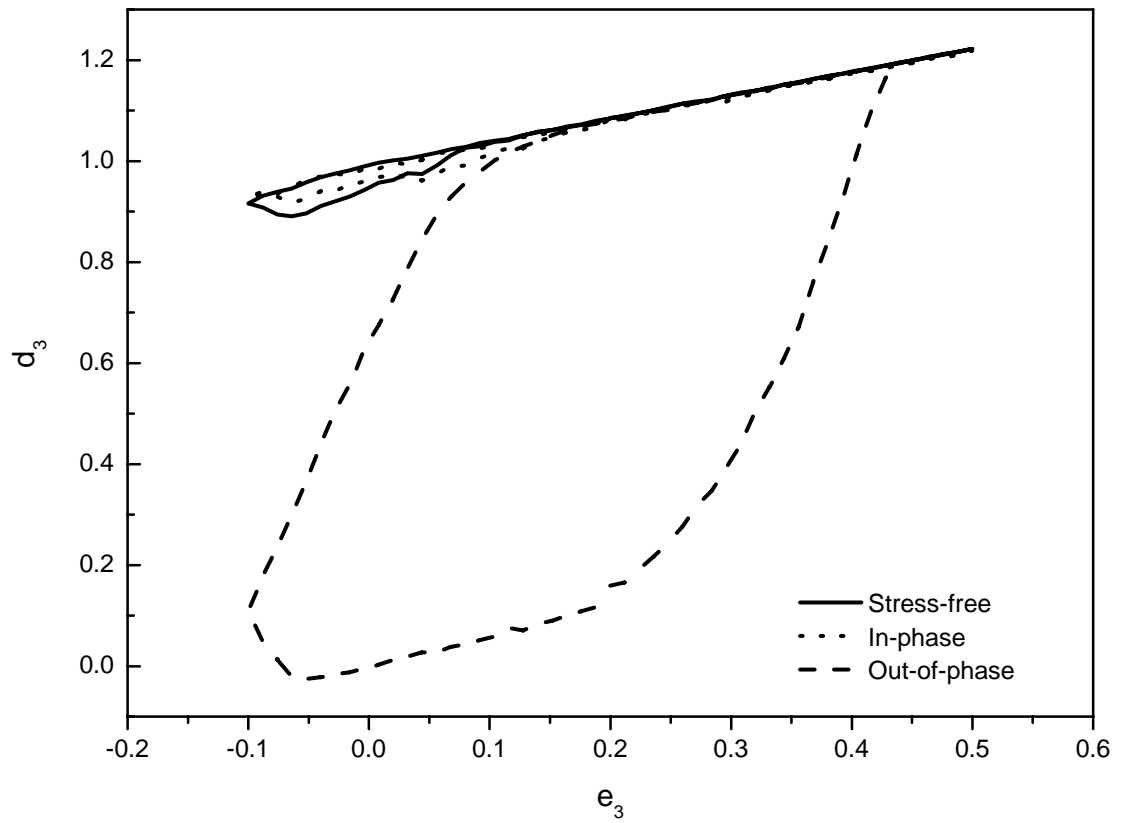


Figure 4.29 The normalized electric displacement of a film under stress-free state, in-phase and out-of-phase conditions

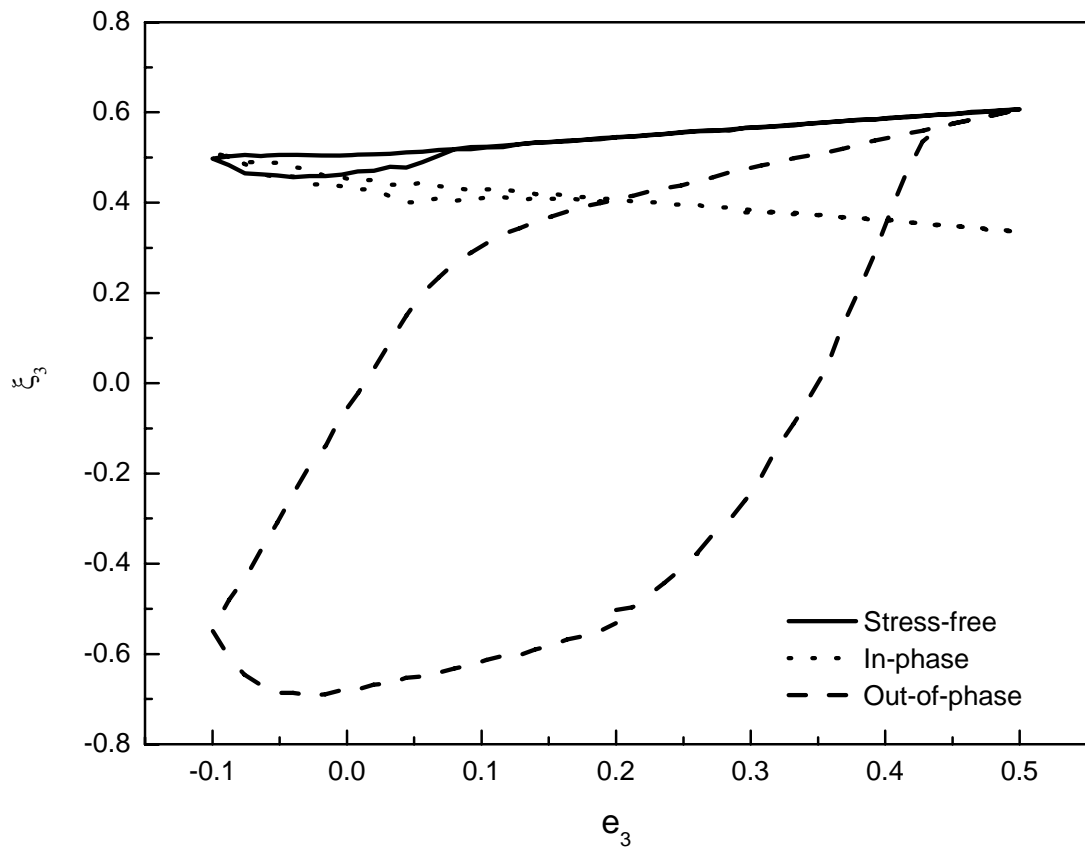


Figure 4.30 The normalized longitudinal strain behavior of a film under stress-free state, in-phase and out-of-phase conditions



By converting the normalized parameters into real quotations, both our stimulated results and the experimental results from Zhou and Kamlah are plotted together, as shown in Figures 4.31 and 4.32. The saturated polarization  $P_s$  and total saturated strain of the system is set to be  $0.39 \text{ C/m}^2$  and  $5 \times 10^{-3}$  respectively. The real parameters are shown in Table 4.1.

	Normalized	Physical		Normalized	Physical
$e_{dc} \rightarrow E_{dc}$	0.2	0.8 kV/mm	$\kappa_r$	---	4955
$e_0 \rightarrow E_0$	0.3	1.2 kV/mm	$\nu$	---	0.3
$J$	---	$1560000 \text{ CV/m}^3$	k	---	0.1
$\zeta_{dc} \rightarrow \sigma_{dc}$	-0.2	-62.4 MPa	n	---	0.5
$\zeta_0 \rightarrow \sigma_0$	0.2	62.4 MPa	$\xi_0 \rightarrow \varepsilon_0$	0.5	$2.5 \times 10^{-3}$
$\zeta_1 \rightarrow \sigma_1$	-0.05	-15.6 MPa	$h_3 \rightarrow H_3$	0.3	468000
$\zeta_{crit} \rightarrow \sigma_{crit}$	0.3	93.6 MPa	$\alpha' \rightarrow \alpha$	0.1	156000
$Y' \rightarrow Y$	1.5	93.6 GPa	$d_{33}' \rightarrow d_{33}$	0.2	$250 \times 10^{-12} \text{ m/V}$
$\kappa' \rightarrow \kappa$	0.45	$4.3875 \times 10^{-8} \text{ F/m}^2$	$d_{31}' \rightarrow d_{31}$	-0.1	$-125 \times 10^{-12} \text{ m/V}$
$\kappa_0$	---	$8.85 \times 10^{-12} \text{ F/m}^2$			

Table 4.1 The set of real parameters used for the simulation

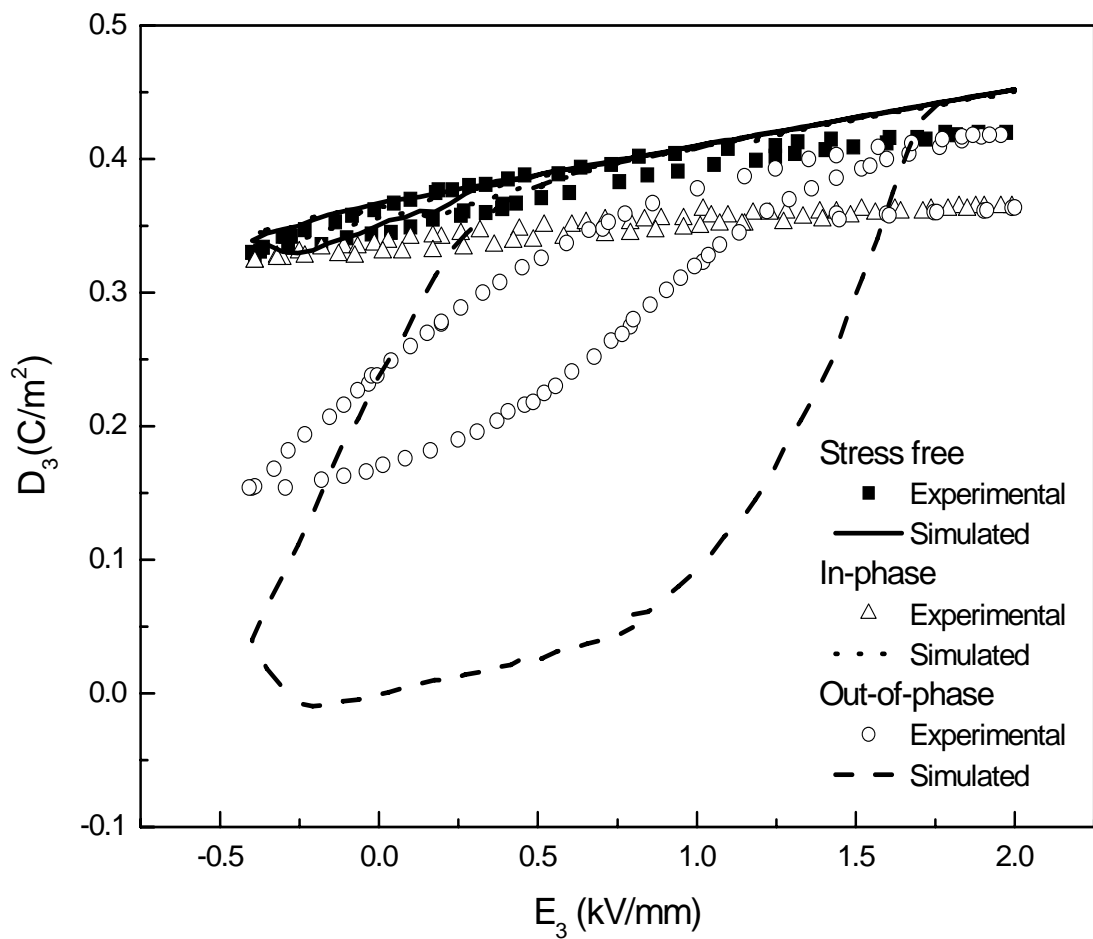


Figure 4.31 Electric displacement versus electric field under stress-free, in-phase and out-of-phase conditions. Symbols are experimental results from Zhou and Kamlah, and lines are simulated results.

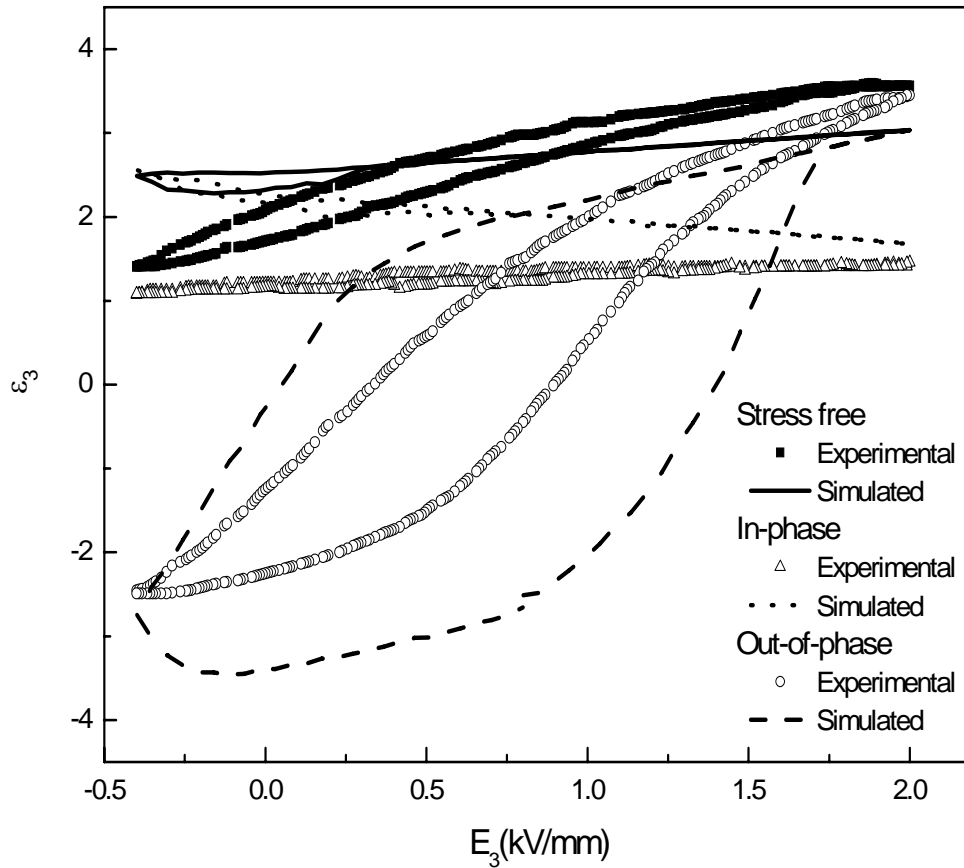


Figure 4.32 Longitudinal strain versus electric field under stress-free, in-phase and out-of-phase conditions. Symbols are experimental results from Zhou and Kamlah, and lines are simulated results.



From Figures 4.31 and 4.32, both experimental (symbols) and simulated (curves)  $D_3 - E_3$  and  $\varepsilon_3 - E_3$  loops are shown under three different loading conditions. At the time at point A in Figure 4.33, both compressive stress and the electric field are maximal. The former forces the dipoles to be aligned along longitudinal direction while the second drives them along the transverse direction. The overall effect is that both influences cancel each other. At point B (in Figure 4.35), both the field and stress are reduced to one half, and again their influences are cancelled. At point C as shown in Figure 4.37, these driving field and stress drop to nearly zero, and there is no change in dipole orientations at all. Consequently, the change in dipole orientation over a cycle must be negligibly small even if it is not zero. It leads to very small changes both in electric displacement and strain.

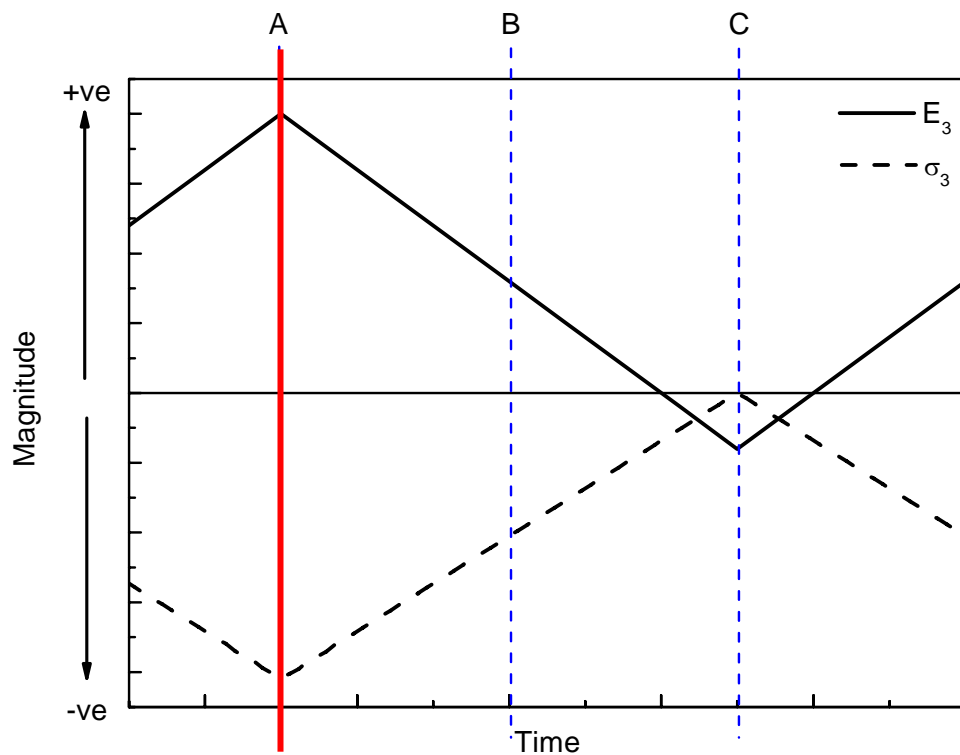


Figure 4.33 Electric-field-time and stress-time patterns of the in-phase loading condition in which the maximum stress is zero (released compression).

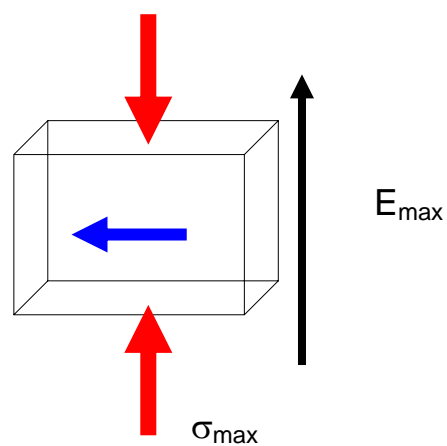


Figure 4.34 Effects of both influences cancel each other when both  $E_3$  and  $\sigma_3$  are the maximum (At point A in Figure 4.33).

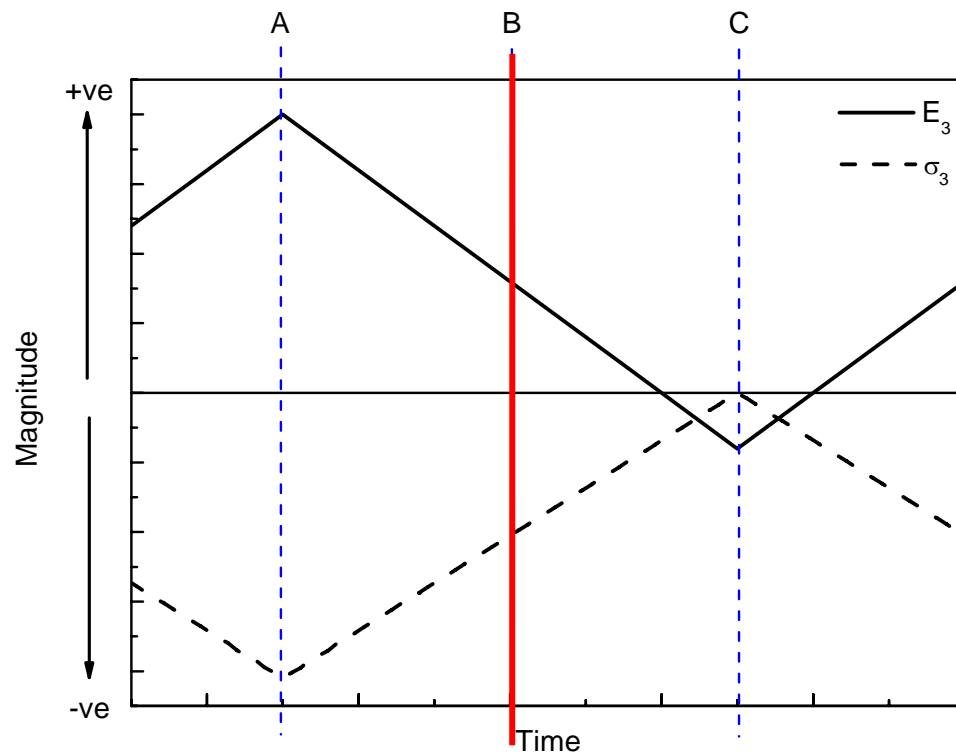


Figure 4.35 Electric-field-time and stress-time patterns of the in-phase loading condition in which the maximum stress is zero (released compression).

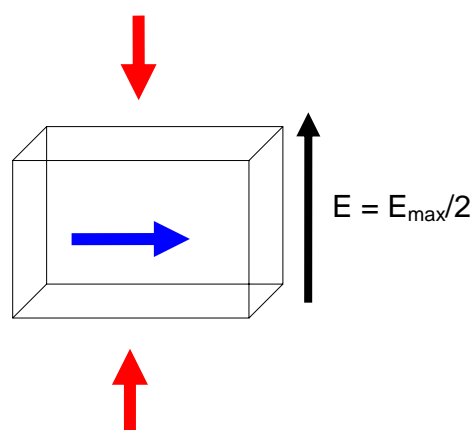


Figure 4.36 Effects of both influences cancel each other when both  $E_3$  and  $\sigma_3$  are exactly at one-half of their maximum value (At point B in Figure 4.35).

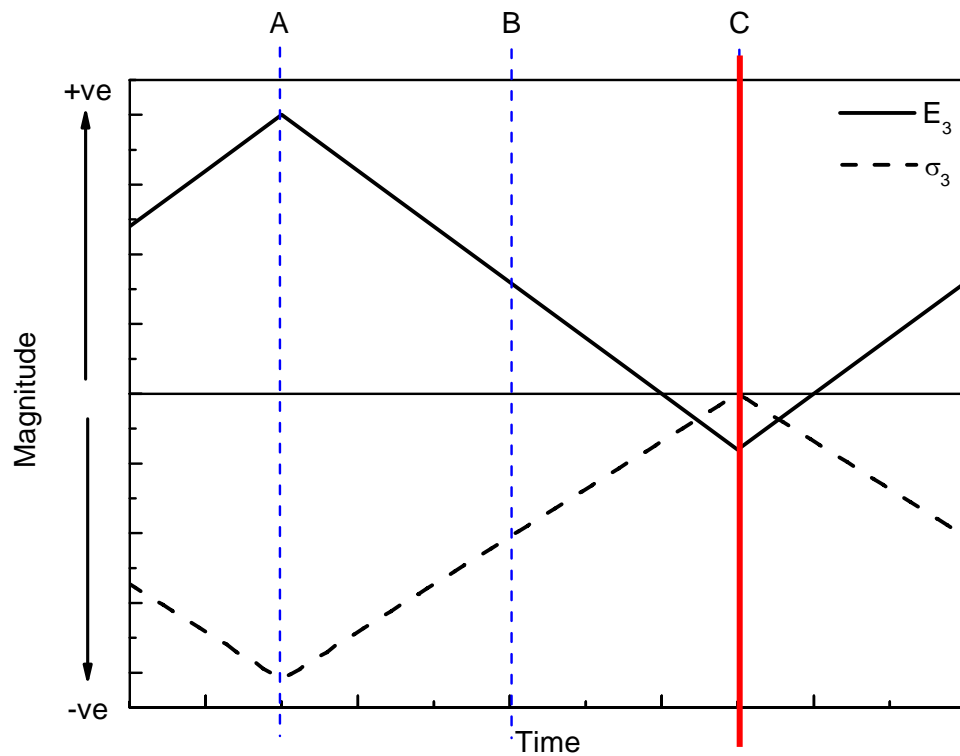


Figure 4.37 Electric-field-time and stress-time patterns of the in-phase loading condition in which the maximum stress is zero (released compression).

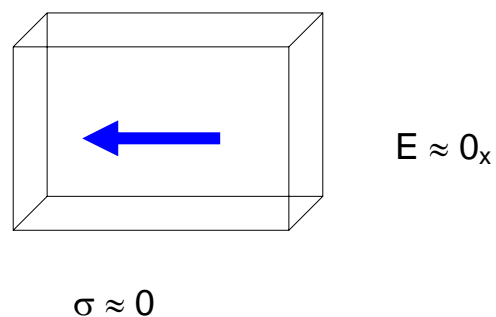


Figure 4.38 Dipoles remain in its original status when both  $E_3$  and  $\sigma_3$  are nearly zero (At point C in Figure 4.37).



On the other hand, in the out-of-phase case, the longitudinal compressive stress is nearly zero when the electric field is maximum as shown in Figure 4.39 (at point A). This leads to a large amount of dipoles to be aligned along the longitudinal direction. Thus, the volume fraction of State A tends to 1 at point A. At point B (in Figure 4.41), the electric field drops to one-half while the stress increases to one half of its maximal value. These two influences now cancel each other and some of the dipoles rotate to the transverse direction. At point C, the stress reaches the maximal value while the electric field drops nearly to zero. At the moment, the compressive stress becomes the only influence forcing most of the dipoles along the transverse direction. Consequently, from points A to C, a large amount of dipoles rotate from longitudinal direction to the transverse one. A large electrical displacement and longitudinal strain are generated in the in-phase condition while and both quantities are diminished in the out-of-phase case. The changes in displacement and strain over a cycle are then very large in the latter condition. Figure 4.45 and Figure 4.46 also show there is a large change in volume fraction in the out-of-phase case whereas there are not many changes in volume fraction in the in-phase case.

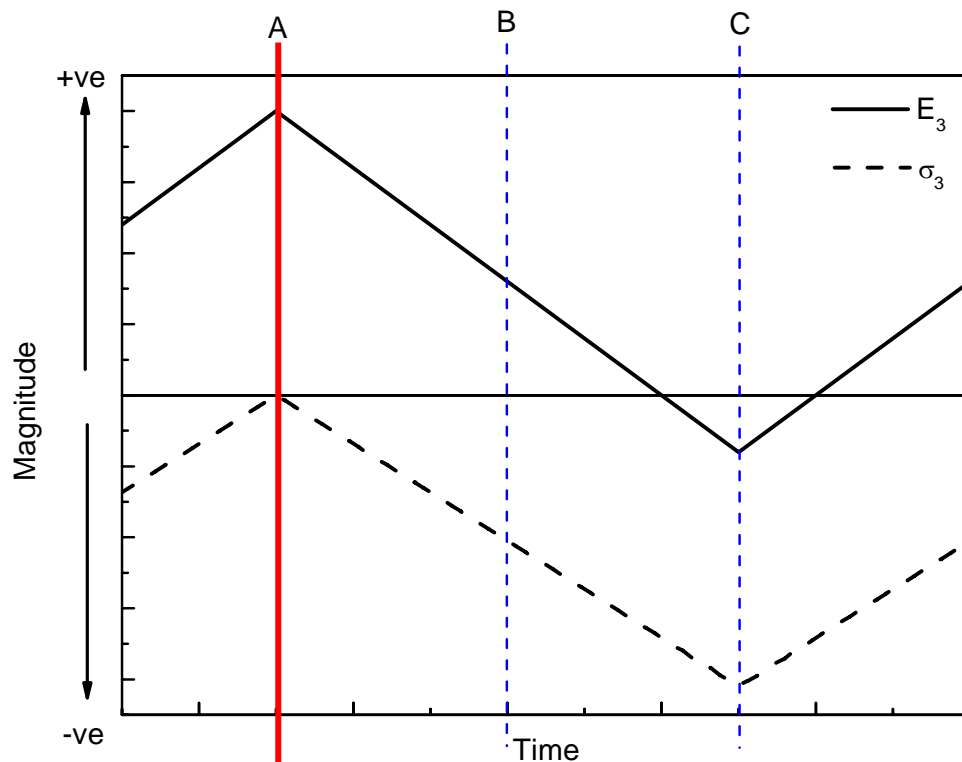


Figure 4.39 Electric-field-time and stress-time patterns of the out-of-phase loading condition in which the maximum stress is zero (released compression).

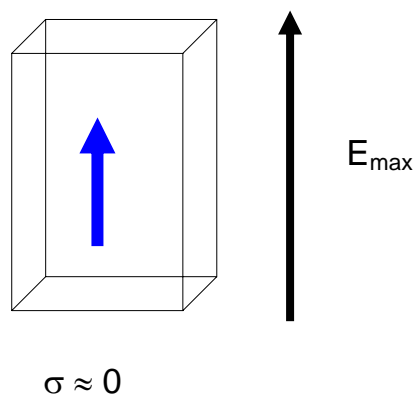


Figure 4.40 Dipoles are aligned along the electric field direction when  $E_3$  is the maximum and  $\sigma_3$  is zero (At point A in Figure 4.39).

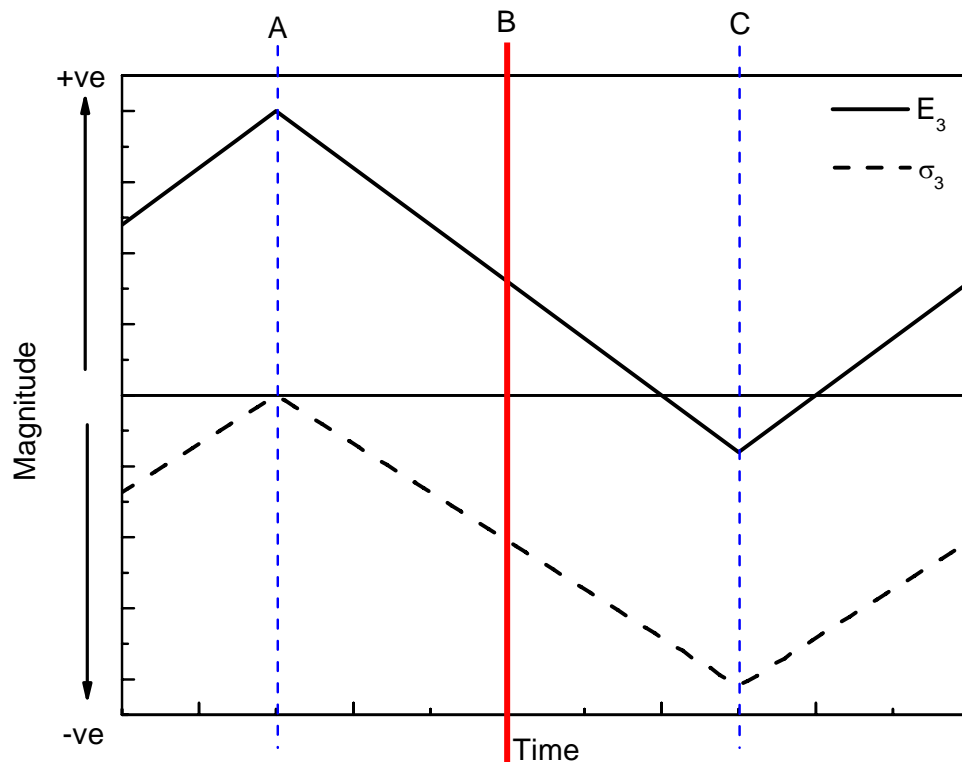


Figure 4.41 Electric-field-time and stress-time patterns of the out-of-phase loading condition in which the maximum stress is zero (released compression).

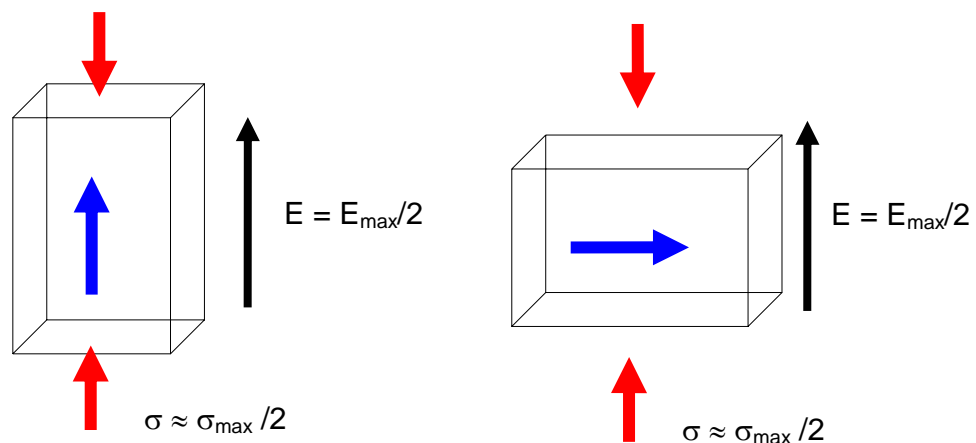


Figure 4.42 Effects of both influences cancel each other at point B. The two possibilities of dipole orientation when both  $E_3$  and  $\sigma_3$  are exactly at one-half of their maximum value (At point B in Figure 4.41).

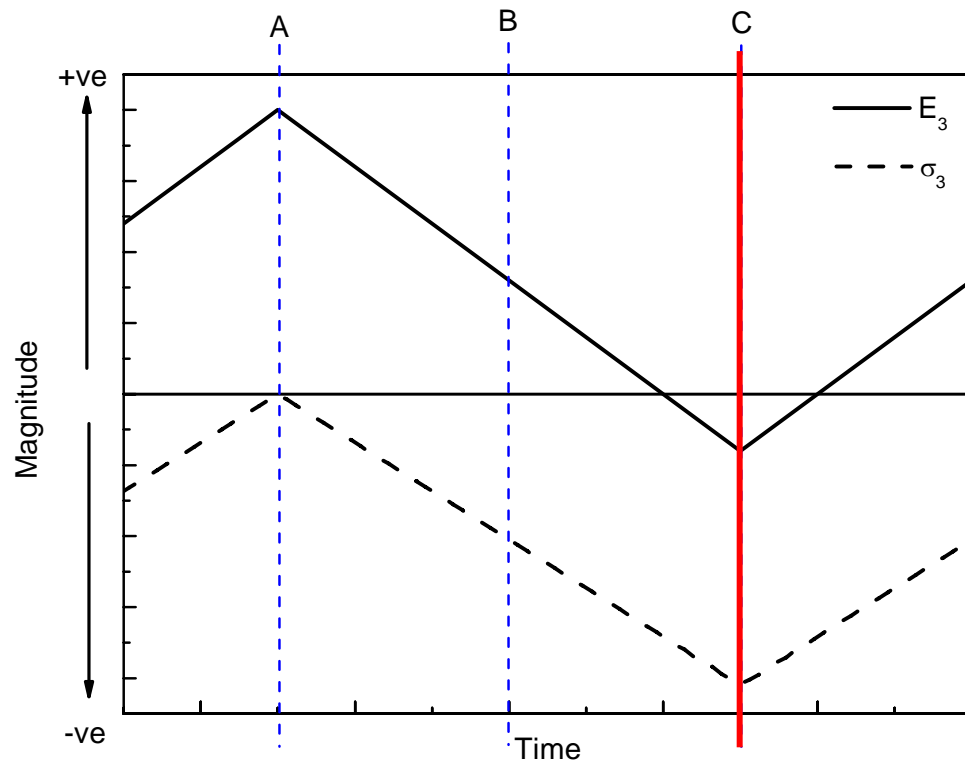


Figure 4.43 Electric-field-time and stress-time patterns of the out-of-phase loading condition in which the maximum stress is zero (released compression).

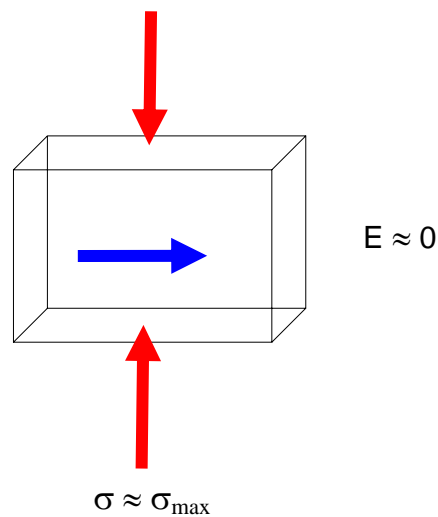


Figure 4.44 Dipoles are aligned perpendicular to the stress direction when  $E_3$  is nearly equal to zero and  $\sigma_3$  is the maximum (At point C in Figure 4.43).

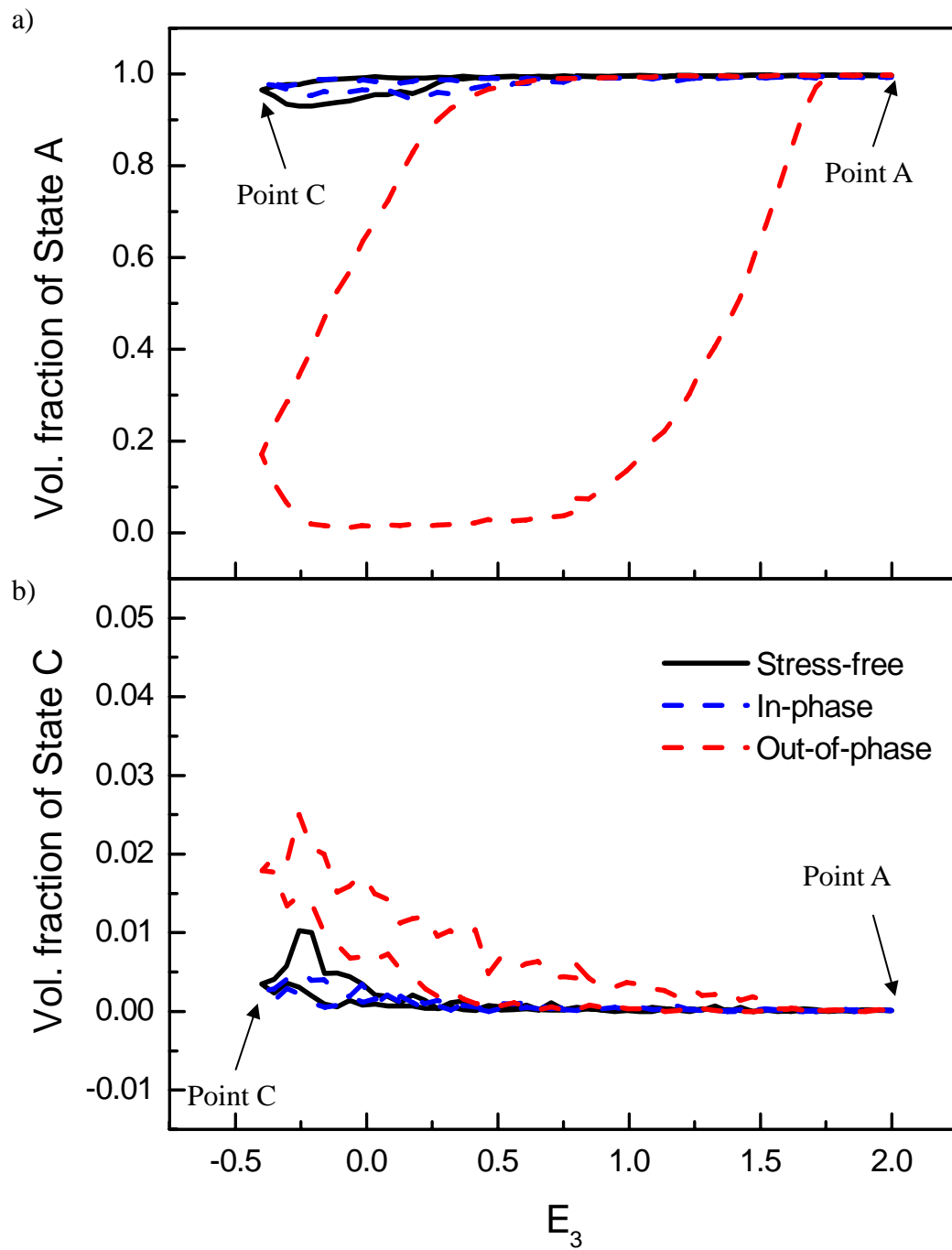


Figure 4.45 Volume fractions of (a) State A and (b) State C versus electric field under stress-free state, in-phase and out-of-phase conditions.

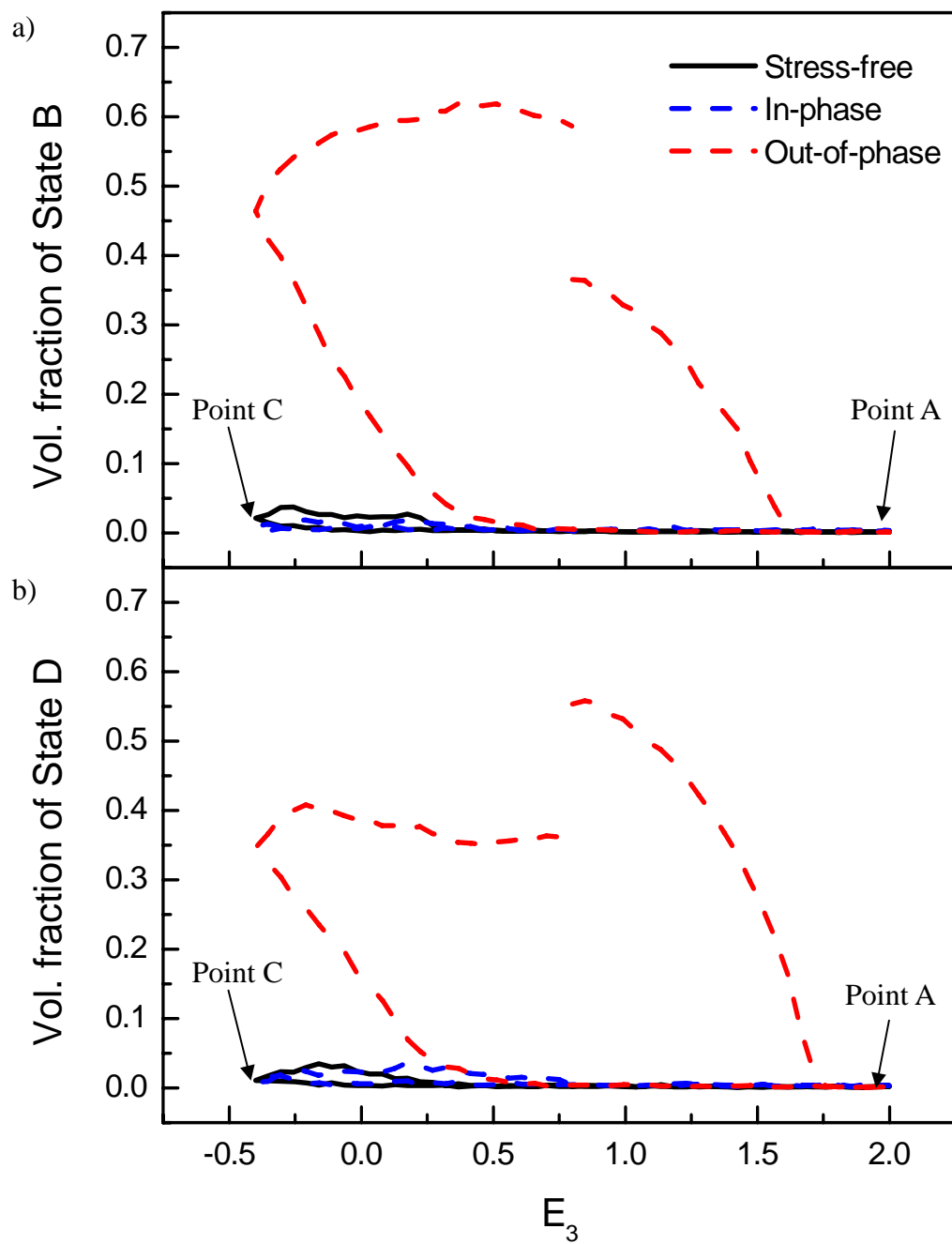


Figure 4.46 Volume fractions of (a) State *B* and (b) State *D* versus electric field under stress-free state, in-phase and out-of-phase conditions.



## Chapter 5 Conclusions and Future work

We have studied the stress effects on the critical behavior and different electromechanical properties of ferroelectric thin films by using the modified four-state Potts model. From a microscopic point of view, the polarization switching is primarily through  $90^\circ$  rotations of dipoles at the domain walls. These rotations are associated with the change in polarization, as well as the mechanical strains.

From our simulation, the effect of static stress on the longitudinal polarization versus temperature and susceptibility versus temperature are demonstrated. The paraelectric–ferroelectric phase transition temperature (or Curie temperature) can thus be determined. It is shown that Curie temperature decreases in the presence of a transverse tensile stress, but increases in case of a compressive stress. The shift in Curie temperature with the longitudinal stress has also been simulated. The results are exactly opposite to those of the transverse stress. The shifting trend of the phase transition temperature obtained from the calculated results qualitatively agrees with experiments. The electromechanical properties of ferroelectric thin films have also been simulated. Effects of stresses in different directions and switching anisotropy parameter  $\phi_c$  on the polarization-electric field loops, electric displacement-electric field loops and butterfly loops for both transverse and longitudinal strain against electric field have been investigated. It is found that the ferroelectricity, in terms of remnant polarization and phase transition temperature, can be enhanced by (i) the application of a transverse compressive stress, (ii) a longitudinal tensile stress, and (iii) high  $\phi_c$  value. Moreover, the maximum electromechanical response can be



achieved by suitably applying the suitable transverse tensile stress or longitudinal compressive stress on the film.

We have also simulated the electromechanical properties under combined electrical and mechanical loadings and the results are compared with results from Zhou and Kamlah's experiment. Even though our simulation results cannot exactly fit the experimental ones, the effect of phase angle between the electric field and the uniaxial compressive stress can be reproduced and explained. The enhanced electromechanical responses for both electrical displacement and strain are due to the competition between the driving electric field and stress which force dipoles to be aligned either along normal or along the film. Different phase difference between the two loadings will lead to different electromechanical response. Correct timing for these driving forces can give rise to optimal electromechanical responses.

We have studied the electromechanical properties and different aspects of polarization switching in terms of domain wall motion. The present model manifests the importance of  $90^\circ$  domain switching in electromechanical properties of ferroelectric materials, such as polarization and strain. In most of the applications of ferroelectric materials, they usually work under combined loading, both electric and mechanical ones, at the same time. As mentioned previously, the phase difference between the electric and mechanical loading affect the electromechanical responses. However, there must be some time delays for the dielectric and mechanical responses to these driving field and stress, due to the material constraints. These two time delays might also be different. Consequently, the optimal electromechanical



responses might be obtained neither at “in-phase” nor “out-of-phase” conditions. That means the phase angle might be a value between  $0^\circ$  and  $180^\circ$ . Even though the optimal condition should be obtained from experiment ultimately, because the selection of fitting parameters for the simulation relies on experimental data, numerical simulation can greatly reduce the experimental works on trial-and-error basis. Furthermore, the frequency response is also worthwhile to study. The drawback of our present model is that there is no single parameter related to the time variable. The relaxation time of the system, i.e. the time for the system to restore to the thermal equilibrium condition, might be chosen and all other times should be scaled with it. The study of low frequency electromechanical properties is still an undeveloped area.



## References

- Abe, K. and S. Komatsu. "Ferroelectric Properties in Epitaxially Grown BaSr<sub>1-x</sub>TiO<sub>3</sub> Thin-Films". *Journal of Applied Physics*, Vol. **77**, pp. 6461-6465.(1995)
- Ball, B. L. and R. C. Smith et al. "A Stress-Dependent Hysteresis Model for PZT". *Material Research Symposium Proceeding*, Vol. **881E**, pp. CC1.8.1.(2005)
- Bellaiche, L. "Piezoelectricity of ferroelectric perovskite from first principles". *Current Opinion in Solid State and Materials Science*, Vol. **6**, pp. 19-25.(2002)
- Berfield, T. A. and N. R. Sottos et al. "Residual Stress Effects in Ferroelectric Thin Films". *Material Research Symposium Proceeding*, Vol. **784**, pp. C.3.2.1-C.3.2.5.(2004)
- Berlincourt, D. and H. Jaffe. "Elastic and Piezoelectric Coefficients of Single-Crystal Barium Titanate". *Physical Review*, Vol. **111**, pp. 143-148.(1958)
- Binder, K. and D. W. Heermann. *Monte Carlo Simulation in Statistical Physics: An Introduction*. Springer, New York.(2002)
- Buzano, C. and M. VDACCHINO et al. "Analysis of a Ferroelectric Pseudo-Spin Hamiltonian by 2Nd Order Cumulant Expansion". *Ferroelectrics*, Vol. **29**, pp. 11-14.(1980)
- Calderon-Moreno, J. M. "Stress induced domain switching of PZT in compression tests". *Materials Science and Engineering*, Vol. **A315**, pp. 227-230.(2001)
- Cao, H. X. and V. C. Lo et al. "Investigation of electromechanical properties in ferroelectric thin films using Monte Carlo simulation". *Journal of Applied Physics*, Vol. **99**, pp. -(2006)
- Chaudhuri, B. K. and T. Atake et al. "Study of Ferroelectric Phase-Transitions in the Rochelle Salt with the Pseudo-Spin-Lattice Coupled Mode Model". *Journal of the Physical Society of Japan*, Vol. **49**, pp. 608-618.(1980)
- Cross, L. E. and R. E. Newham. "History of Ferroelectrics". *The Ceramics and Civilization*, Vol. **III**, pp. 289-305.(1987)
- Duiker, H. M. and P. D. Beale. "Grain-Size Effects in Ferroelectric Switching". *Physical Review B*, Vol. **41**, pp. 490-495.(1990)
- Feng, Z. Y. and D. Lin et al. "Effect of uniaxial stress on the electromechanical response of < 001 >-oriented Pb(Mg<sub>1/3</sub>Nb<sub>2/3</sub>)O<sub>3</sub>-PbTiO<sub>3</sub> crystals". *Journal of Applied Physics*, Vol. **97**, pp. -(2005)
- Frey, M. H. and D. A. Payne. "Nanocrystalline Barium-Titanate - Evidence for the Absence of Ferroelectricity in Sol-Gel Derived Thin-Layer Capacitors". *Applied Physics Letters*, Vol. **63**, pp. 2753-2755.(1993)
- Garino, T. J. and M. Harrington. "Residual Stress in PZT Thin Films and its Effect on Ferroelectric Properties ". *Materials Research Society symposia proceedings*, Vol. **243**, pp. 341-347.(1992)
- Gifford, K. and A. I. Kingon. "Oriented PZT Films". *Ferroelectrics*, Vol. pp. (1992)
- Heermann, D. W. and K. Binder. *Monte Carlo Simulation in Statistical Physics: An Introduction*. Springer, New York.(2002)
- Ishibashi, Y. and M. Iwata et al. "Polarization Reversals in the Presence of 90° Domain Walls". *Japanese Journal of Applied Physics Part 1-Regular Papers Short Notes & Review Papers*, Vol. **44**, pp. 7512-7517.(2005)



## THE HONG KONG POLYTECHNIC UNIVERSITY

- Kim, D. J. and J. P. Maria et al. "Evaluation of intrinsic and extrinsic contributions to the piezoelectric properties of Pb(Zr<sub>1-x</sub>Tx)O<sub>3</sub> thin films as a function of composition". *Journal of Applied Physics*, Vol. **93**, pp. 5568-5575.(2003)
- Kushida, K. and H. Takeuchi. "Piezoelectricity of C-Axis Oriented Pbtio<sub>3</sub> Thin-Films". *Applied Physics Letters*, Vol. **50**, pp. 1800-1801.(1987)
- Kushida, K. and H. Takeuchi. "Ferroelectric Properties of C-Axis Oriented Pbtio<sub>3</sub> Films". *Ferroelectrics*, Vol. **108**, pp. 3-8.(1990)
- Kushida, K. and H. Takeuchi. "Epitaxial growth of PbTiO<sub>3</sub> films on SrTiO<sub>3</sub> by RF magnetron sputtering". *IEEE Transactions on Ultrasonics, Ferroelectrics and Frequency Control*, Vol. **38**, pp. 656-662.(1991)
- Lappalainen, J. and J. Frantti et al. "Electrical and mechanical properties of ferroelectric thin films laser ablated from a Pb<sub>0.97</sub>Nd<sub>0.02</sub>(Zr<sub>0.55</sub>Ti<sub>0.45</sub>)O<sub>3</sub> target". *Journal of Applied Physics*, Vol. **82**, pp. 3469-3477.(1997)
- Li, K. T. *Thickness Effects in Ferroelectric Thin Films*. Department of Applied Physics, The Hong Kong Polytechnic University. **M. Phil.**
- Li, K. T. and V. C. Lo. "Simulation of thickness dependence in ferroelectric thin films". *Solid State Communications*, Vol. **132**, pp. 49-54.(2004)
- Li, K. T. and V. C. Lo. "Simulation of oxygen vacancy induced phenomena in ferroelectric thin films". *Journal of Applied Physics*, Vol. **97**, pp. -.(2005)
- Li, W. F. and G. J. Weng. "A theory of ferroelectric hysteresis with a superimposed stress". *Journal of Applied Physics*, Vol. **91**, pp. 3806-3815.(2002)
- Lian, L. and N. R. Sottos. "Effects of thickness on the piezoelectric and dielectric properties of lead zirconate titanate thin films". *Journal of Applied Physics*, Vol. **87**, pp. 3941-3949.(2000)
- Lian, L. and N. R. Sottos. "Stress effects in sol-gel derived ferroelectric thin films". *Journal of Applied Physics*, Vol. **95**, pp. 629-634.(2004)
- Lines, M. E. and A. M. Glass. *Principles and Applications of Ferroelectrics and Related Materials*. Oxford University Press, London.(1977)
- Liu, J. M. "Kinetics of partial polarization reversal in ferroelectric Potts lattices under an external electric field". *Solid State Communications*, Vol. **109**, pp. 671-676.(1999)
- Liu, J. M. and Z. C. Wu et al. "Q-dependence of dynamic hysteresis in Potts spin lattice: Monte-Carlo simulation". *Solid State Communications*, Vol. **115**, pp. 383-388.(2000)
- Lo, V. C. "Modeling the role of oxygen vacancy on ferroelectric properties in thin films". *Journal of Applied Physics*, Vol. **92**, pp. 6778-6786.(2002)
- Lu, X. M. and J. S. Zhu et al. "Phase transition related stress in ferroelectric thin films". *Thin Solid Films*, Vol. **375**, pp. 15-18.(2000)
- Lynch, C. S. "The effect of uniaxial stress on the electro-mechanical response of 8/65/35 PLZT". *Acta Materialia*, Vol. **44**, pp. 4137-4148.(1996)
- Maiwa, H. and N. Ichinose. "Thickness dependence of the electrical and electromechanical properties of Pb(Zr,Ti)O<sub>3</sub> thin films". *Japanese Journal of Applied Physics Part 1-Regular Papers Short Notes & Review Papers*, Vol. **42**, pp. 4392-4398.(2003)
- Mitrovic, M. and G. P. Carman et al. "Response of piezoelectric stack actuators under combined electro-mechanical loading". *International Journal of Solids and Structures*, Vol. **38**, pp. 4357-4374.(2001)
- Nagarajan, V. and I. G. Jenkins et al. "Thickness dependence of structural and



## THE HONG KONG POLYTECHNIC UNIVERSITY

- electrical properties in epitaxial lead zirconate titanate films". *Journal of Applied Physics*, Vol. **86**, pp. 595-602.(1999)
- Newman, M. E. J. and G. T. Barkema. *Monte Carlo methods in statistical physics* Oxford University Press, New York.(1999)
- Ohno, T. and D. S. Fu et al. "Residual stress in lead titanate thin film on different substrates". *Journal of the European Ceramic Society*, Vol. **24**, pp. 1669-1672.(2004)
- Ono, I. "Phase-Transition of Ferromagnetic and Antiferromagnetic R-State Potts Models by the Bethe Approximation". *Journal of Physics C-Solid State Physics*, Vol. **17**, pp. 3615-3631.(1984)
- Onsager, L. "A 2d model with an order-disorder transition". *Physical Review*, Vol. **65**, pp. 117-149.(1944)
- P.W. Forsbergh, J. "Effect of a Two-Dimensional Pressure on the Curie Point of Barium Titanate". *Physical Review*, Vol. **93**, pp. 686-692.(1954)
- Pertsev, N. A. and V. G. Koukhar. "Polarization instability in polydomain ferroelectric epitaxial thin films and the formation of heterophase structures". *Physical Review Letters*, Vol. **84**, pp. 3722-3725.(2000)
- Pertsev, N. A. and A. G. Zembilgotov et al. "Ferroelectric thin films grown on tensile substrates: Renormalization of the Curie-Weiss law and apparent absence of ferroelectricity". *Journal of Applied Physics*, Vol. **85**, pp. 1698-1701.(1999)
- Pertsev, N. A. and A. G. Zembilgotov et al. "Effect of mechanical boundary conditions on phase diagrams of epitaxial ferroelectric thin films". *Physical Review Letters*, Vol. **80**, pp. 1988-1991.(1998)
- Privman, V. *Finite Size Scaling and Numerical Simulation of Statistical Systems* World Scientific, New Jersey.(1990)
- Qian, H. and L. A. Bursill. "Random-field Potts model for the polar domains of lead magnesium niobate and lead scandium tantalate". *International Journal of Modern Physics B*, Vol. **10**, pp. 2027-2047.(1996)
- Rossetti, G. A. and L. E. Cross et al. "Stress-Induced Shift of the Curie-Point in Epitaxial Pbtio<sub>3</sub> Thin-Films". *Applied Physics Letters*, Vol. **59**, pp. 2524-2526.(1991)
- Saito, K. and T. Kurosawa et al. "Structural characterization and 90 degrees domain contribution to ferroelectricity of epitaxial Pb(Zr-0.35,Ti-0.65)O-3 thin films". *Journal of Applied Physics*, Vol. **93**, pp. 545-550.(2003)
- Scott, J. F. "Device physics of ferroelectric memories". *Ferroelectrics*, Vol. **183**, pp. 51.(1996)
- Shaw, T. M. and Z. Suo et al. "The effect of stress on the dielectric properties of barium strontium titanate thin films". *Applied Physics Letters*, Vol. **75**, pp. 2129-2131.(1999)
- Shepard, J. F. and S. T. McKinstry et al. "Properties of PZT Thin Films as a Function of In-plane Biaxial Stress". *Proceedings of the 10<sup>th</sup> IEEE Int. Symposium on Application of Ferroelectrics*, Vol. pp. 161-165.(1996)
- Slivka, A. G. and V. M. Kedyulich et al. "The effect of external factors on dielectric permittivity of Rochelle salt: humidity, annealing, stresses, electric field". *Condensed Matter Physics*, Vol. **8**, pp. 623-638.(2005)
- Smith, R. C. *Smart Material Systems: Model Development* Philadelphia, Pa. : Society for Industrial and Applied Mathematics,(2005)
- Song, T. K. and J. S. Kim et al. "Landau-Khalatnikov simulations for the effects of



## THE HONG KONG POLYTECHNIC UNIVERSITY

- external stresses on the ferroelectric properties of Pb(Zr,Ti)O<sub>3</sub> thin films". *Thin Solid Films*, Vol. **424**, pp. 84-87.(2003)
- Strukov, B. A. and A. P. Levanyuk. *Ferroelectric Phenomena in Crystals*. Springer-Verlag, Berlin.(1998)
- Takayama, R. and Y. Tomita. "Preparation of Epitaxial Pb(ZrxTi1-X)O<sub>3</sub> Thin-Films and Their Crystallographic, Pyroelectric, and Ferroelectric Properties". *Journal of Applied Physics*, Vol. **65**, pp. 1666-1670.(1989)
- Taylor, T. R. and P. J. Hansen et al. "Impact of thermal strain on the dielectric constant of sputtered barium strontium titanate thin films". *Applied Physics Letters*, Vol. **80**, pp. 1978-1980.(2002)
- Tuttle, B. A. and J. A. Voigt et al. "Chemically Prepared Pb(Zr,Ti)O<sub>3</sub> Thin Films: The Effects of Orientation and Stress". *Proceedings of the 8th IEEE Int. Symposium on Application of Ferroelectrics*, Vol. pp. 344-348.(1992)
- Wada, K. and S. Yoshida et al. "Dynamical susceptibility in KH<sub>2</sub>PO<sub>4</sub>-type crystals above and below T<sub>c</sub>". *Journal of the Physical Society of Japan*, Vol. **70**, pp. 1019-1025.(2001)
- Wang, X. S. "The Effects of Uniaxial Stress Distribution on the ferroelectric properties of thin films with first-order phase transition". *Solid State Communications*, Vol. **121**, pp. 111-115.(2002)
- Wang, Y. X. and W. L. Zhong et al. "First principles study on the ferroelectricity of the perovskite ABO<sub>3</sub> ferroelectrics". *Chinese Physics*, Vol. **11**, pp. 714-719.(2002)
- Waser, R. "Dielectric analysis of integrated ceramic thin film capacitors". *Integrated Ferroelectrics*, Vol. **15**, pp. 39-51.(1997)
- Wu, F. Y. "The Potts-Model". *Reviews of Modern Physics*, Vol. **54**, pp. 235-268.(1982)
- Yao, D. L. and Y. Z. Wu et al. "Long-range effect on the Curie temperature of ferroelectric films". *Physica Status Solidi B-Basic Research*, Vol. **231**, pp. 3-10.(2002)
- Yuzyuk, Y. I. and P. Simon et al. "Stress effect on the ferroelectric-to-paraelectric phase transition in heteroepitaxial (Ba,Sr)TiO<sub>3</sub>/(001)MgO thin film studied by Raman scattering and x-ray diffraction". *Physical Review B*, Vol. **66**, pp. -. (2002)
- Zhang, L. L. and J. Tsaur et al. "Residual stress study of SiO<sub>2</sub>/Pt/Pb(Zr,Ti)O<sub>3</sub>/Pt multilayer structure for micro electro mechanical system applications". *Japanese Journal of Applied Physics Part 1-Regular Papers Short Notes & Review Papers*, Vol. **42**, pp. 1386-1390.(2003)
- Zhang, W. and K. Bhattacharya. "A computational model of ferroelectric domains. Part I: model formulation and domain switching". *Acta Materialia*, Vol. **53**, pp. 185-198.(2005)
- Zhong, W. and D. Vanderbilt et al. "Phase-Transitions in BaTiO<sub>3</sub> from First Principles". *Physical Review Letters*, Vol. **73**, pp. 1861-1864.(1994)
- Zhong, W. and D. Vanderbilt et al. "First-Principles Theory of Ferroelectric Phase-Transitions for Perovskites - the Case of BaTiO<sub>3</sub>". *Physical Review B*, Vol. **52**, pp. 6301-6312.(1995)
- Zhou, D. Y. and M. Kamlah. "High-field dielectric and piezoelectric performance of soft lead zirconate titanate piezoceramics under combined electromechanical loading". *Journal of Applied Physics*, Vol. **96**, pp. 6634-6641.(2004)



THE HONG KONG POLYTECHNIC UNIVERSITY

- Zhou, D. Y. and M. Kamlah et al. "Effects of uniaxial prestress on the ferroelectric hysteretic response of soft PZT". *Journal of the European Ceramic Society*, Vol. **25**, pp. 425-432.(2005)
- Zhou, Y. C. and Z. Y. Yang et al. "Residual stress in PZT thin films prepared by pulsed laser deposition". *Surface and Coatings Technology*, Vol. **162**, pp. 202-211.(2003)